Microstructure, lattice strain and mechanical properties of single phase multi-component alloys

Thesis for the partial fulfilment of the requirements for the academic degree of

Doktoringenieur (Dr.-Ing.)

submitted to

Faculty of Mechanical Science and Engineering

Dresden University of Technology

by

Pramote Thirathipviwat

Born on 11.07.1984 in Bangkok, Thailand

Dresden 2019

Submitted on: 15.01.2019

Date of defense: 20.06.2019

Referee 1: Prof. Dr. Kornelius Nielsch (TU Dresden, IFW Dresden)

Referee 2: Assoc. Prof. Dr. Piter Gargarella (DEMa/UFSCar, Brazil

Abstract

The high entropy alloys (HEAs) have been developed based on the concept of entropic stabilization associated with a large number of constituent elements. The high configurational entropy in HEAs is expected to cause promising characteristic properties, i.e. high microstructural stability and high mechanical properties. In this study, the equiatomic *fcc*-structured FeNiCoCrMn and the *bcc*-structured TiNbHfTaZr single phase high entropy alloys (HEAs) were investigated regarding the effect of multiple atom species on microstructure, intrinsic lattice strain and mechanical properties. In a comparison with the HEAs, the sub-alloys having less chemical complexity were studied. The selected sub-alloys of the FeNiCoCrMn HEA were FeNiCoCr, FeNiCo, FeNi alloys and pure Ni, while equiatomic TiNbHfTa, TiNbHf, TiNb alloys and pure Nb were studied to compare with the TiNbHfTaZr HEA.

The samples in this study were prepared by arc-melting, cold-crucible casting and thermomechanical treatment. The thermal phase stability of the FeNiCoCrMn HEA, TiNbHfTaZr HEA and their sub-alloys were observed and no second phase was formed between 300 - 1500 K. In high entropy alloys, the random arrangement of multiple atom species is assumed to cause large atomic displacements at lattice sites, which give rise to a severe lattice distortion. The evidences of lattice distortion in HEAs have been limitedly reported due to a difficulty of experimental investigation. In this work, the pair distribution function (PDF) method was used to assess local strain with analysis of diffuse intensities on total synchrotron X-ray scattering data. The current study found that the level of local lattice strain associated with atomic displacement was a function of atomic size misfit. The local lattice strain of the FeNiCoCrMn HEA was small and comparable to that of the sub-alloys which obtain similar values of the atomic size misfit. In contrast to the FeNiCoCrMn system, the magnitude of the local lattice strain increased with the value of atomic size misfit from the unary Nb sample to the quinary TiNbHfTaZr HEA. The lattice distortion was evident in the TiNbHfTaZr HEA due to large local lattice strain, but the local lattice strain of the FeNiCoCrMn HEA was not anomalously large. The level of lattice strain determines the solid solution hardening as a consequence of the elastic interaction between dislocations and atoms. The comparable level of the lattice strain in the FeNiCoCrMn HEA, its sub-alloys and Ni sample led to narrow range of hardness (64 – 132 HV) and tensile yield strength (60 – 192 MPa). For the *bcc*-

structured samples, the hardness and the yield strength significantly varied depending on the level of local lattice strain, between 80 – 327 HV of hardness and 207 – 985 MPa of tensile yield strength. It is clear from the result that the atomic size misfit influences the level of the local lattice strain and the solid solution hardening.

Cold rotary swaging was used to study the work hardening in the HEAs because it can delay fracture by large hydrostatic stresses. The large plastic deformability was observed in the FeNiCoCrMn and TiNbHfTaZr HEAs. The TiNbHfTaZr HEA was cold-swaged by 90% reduction of the cross-sectional area without intermediate annealing. The FeNiCoCrMn HEA was swaged until 85% reduction of the cross-sectional area; however, it was observed that it could be further deformed. The dislocation densities of the HEAs and its sub-alloys after the cold deformation were calculated as in the range between 10^{14} - 10^{15} m^{-2}, in a good agreement with reported values of conventional metals after severe plastic deformation. This finding suggested that the level of dislocation density storage was correlated with the number of the constituent elements, the level of lattice distortion associated with atomic size misfit and the intrinsic properties (i.e. the stacking fault energy and the melting point). Whereas the intrinsic lattice strains of the FeNiCoCrMn HEA and its sub-alloys were comparable, the levels of dislocation storage were different possibly due to a difference of stacking fault energy. For the *bcc*-structured samples, the dislocation densities of the TiNbHfTaZr HEA, TiNbHfTa and TiNbHf alloys were large due to the large atomic size misfits. The high dislocation density leads to strong interactions between dislocations, which results in high resistance to dislocation motions. The high mechanical properties (hardness and yield strength) in the as-deformed FeNiCoCrMn and TiNbHfTaZr HEA were presented with the evidence of high dislocation densities. Moreover, the hardness and yield strength of the FeNiCoCrMn HEA significantly increased by the deformation, while those of the TiNbHfTaZr HEA after the deformation were slightly changed from the undeformed HEA. The large work hardenability of the FeNiCoCrMn HEA is possibly caused by small solid solution hardening and ease of twin formation.

The research results suggest a further step towards designing an alloy composition for a development of microstructure and mechanical properties of high entropy alloys. It is evidently clear from the findings that the large number of constituent elements (in a term of high configurational entropy) is not only a factor in the determination of lattice distortion,

microstructure and mechanical properties, but the type and the combination of constituent elements including the atomic interactions (i.e. atomic size misfit) have also an effect.

Zusammenfassung

Die Hochentropielegierungen (HELen) wurden auf der Grundlage des Konzepts der entropischen Stabilisierung entwickelt, was eine große Anzahl von Legierungselementen beinhaltet. Es wird erwartet, dass die hohe Konfigurationsentropie in HELen vielversprechende charakteristische Eigenschaften hervorruft, d.h. hohe mikrostrukturelle Stabilität und hohe mechanische Eigenschaften. In dieser Studie wurden die äquiatomare kfz-strukturierte FeNiCoCrMn und die krz-strukturierte TiNbHfTaZr Einphasen-Hochentropielegierung hinsichtlich der Wirkung mehrerer Atomarten auf das Gefüge, die intrinsische Gitterdehnung und die mechanischen Eigenschaften untersucht. Im Vergleich zu den HELen wurden die Sublegierungen mit geringerer chemischer Komplexität untersucht. Die ausgewählten Sublegierungen der FeNiCoCrMn HEL waren FeNiCoCr, FeNiCo, FeNi-Legierungen und reines Ni, während äquiatomare TiNbHfTa, TiNbHf, TiNbHf, TiNb-Legierungen und reines Nb im Vergleich zur TiNbHfTaZr HEL untersucht wurden.

Die Proben in dieser Studie wurden durch Lichtbogenschmelzen, Kalttiegelguss und thermomechanische Behandlung hergestellt. Die thermische Phasenstabilität der FeNiCoCrMn HEL, der TiNbHfTaZr HEL und ihrer Sublegierungen wurde untersucht und es wurde keine zweite Phase zwischen 300 - 1500 K gebildet. Bei Hochentropielegierungen wird angenommen, dass die zufällige Anordnung mehrerer Atomarten zu großen Atomverschiebungen an den Gitterplätzen führt, die eine starke Gitterverzerrung hervorrufen. Aufgrund der Schwierigkeit der experimentellen Untersuchung wurden Beweise für Gitterverzerrungen bei HELen nur begrenzt berichtet. In dieser Studie wurde die Methode der Paarverteilungsfunktion (PDF) verwendet, um die lokale Dehnung mit Analyse der diffusen Intensitäten der gesamten Synchrotron-Röntgenstreuungsdaten zu beurteilen. Die aktuelle Studie ergab, dass die Höhe der lokalen Gitterdehnung, die mit der atomaren Verschiebung einhergeht, eine Funktion der Differenz der Atomgröße ist. Die lokale Gitterdehnung der FeNiCoCrMn HEL war klein und vergleichbar mit der der Sublegierungen, für die ähnliche Werte für die Atomgrößen-Unterschiede ermittelt wurden. Im Gegensatz zum FeNiCoCrMn-System stieg die Größe der lokalen Gitterdehnung mit dem Wert der Atomgrößendifferenz von der unären Nb-Probe bis zur quinären TiNbHfTaZr HEL. Die Gitterverzerrung war in der TiNbHfTaZr HEL aufgrund der großen lokalen Gitterdehnung

offensichtlich, wohingegen die lokale Gitterdehnung der FeNiCoCrMn HEL nicht ungewöhnlich groß war. Die Höhe der Gitterdehnung bestimmt die Mischkristallverfestigung als Folge der elastischen Wechselwirkung zwischen Versetzungen und Atomen. Der vergleichbare Wert der Gitterdehnung in der FeNiCoCrMn HEL, seinen Sublegierungen und den Ni-Proben führte zu einem engen Härte- (64 - 132 HV) und Streckgrenzenbereich (60 - 192 MPa). Für die krz-strukturierten Proben variierten die Härte und die Streckgrenze dagegen je nach Höhe der lokalen Gitterdehnung signifikant, d.h zwischen 80 - 327 HV hinsichtlich der Härte und zwischen 207 - 985 MPa hinsichtlich der Streckgrenze. Aus dem Ergebnis ist ersichtlich, dass die Differenz der Atomgröße einen Einfluss auf die Höhe der lokalen Gitterdehnung und die Mischkristallverfestigung hat.

Das Kalthämmen wurde für die Untersuchung der Kaltverfestigung in den HELen genutzt, da es den Bruch durch die großen hydrostatischen Spannungen verzögern kann. Die große plastische Verformbarkeit wurde bei den FeNiCoCrMn und TiNbHfTaZr HELen beobachtet. Die TiNbHfTaZr HEL wurde ohne Zwischenglühen um 90% der Querschnittsfläche kaltgehämmert. Die FeNiCoCrMn HEL wurde bis zu einer Verkleinerung der Querschnittsfläche von 85% gehämmert, wobei jedoch eine weitere Verformung möglich gewesen wäre. Die Versetzungsdichten der HELen und ihrer Sublegierungen wurden nach dem Verformung in einem Bereich zwischen 10^{14} - 10^{15} m^{-2} berechnet, was in guter Übereinstimmung mit den berichteten Werten konventioneller Metalle nach starker plastischer Verformung ist. Dieses Ergebnis deutete darauf hin, dass die Höhe der gespeicherten Versetzungsdichte mit der Anzahl der beinhaltenden Elemente, dem Grad der Gitterverzerrung im Zusammenhang mit der Differenz der Atomgröße und den intrinsischen Eigenschaften (d.h. der Stapelfehlerenergie und dem Schmelzpunkt) korreliert. Obwohl die intrinsischen Gitterdehnungen der FeNiCoCrMn HEL und seiner Sublegierungen vergleichbar waren, waren die Werte der gespeicherten Versetzungen unterschiedlich, was möglicherweise an einer Differenz der Stapelfehlerenergie lag. Für die krz-strukturierten Proben waren die Versetzungsdichten der TiNbHfTaZr HEL, der TiNbHfTa- und der TiNbHf-Legierungen aufgrund der großen Atomgrößenunterschiede hoch. Die hohe Versetzungsdichte bewirkt starke Wechselwirkungen zwischen den Versetzungen, was zu einem hohen Widerstand gegen Versetzungsbewegungen führt. Die hohen mechanischen Eigenschaften (Härte und Streckgrenze) in den verformten FeNiCoCrMn und TiNbHfTaZr HELen wurden mit dem Nachweis hoher Versetzungsdichten belegt. Darüber hinaus wurden die Härte und die

Streckgrenze des FeNiCoCrMn HEL durch das Kalthämmern deutlich erhöht, während die der TiNbHfTaZr HEL nach dem Hämmerprozess nur leicht gegenüber der unverformten HEL verändert wurden. Die große Kaltverfestigung der FeNiCoCrMn HEL ist möglicherweise auf eine geringe Mischkristallhärtung und eine geringfügige Zwillingsbildung zurückzuführen.

Die Forschungsergebnisse empfehlen für die Entwicklung des Gefüges und der mechanischen Eigenschaften von Hochentropielegierungen weitere Schritte hinsichtlich eines zielführenden Legierungsdesigns durchzuführenhin. Aus den Ergebnissen geht eindeutig hervor, dass die große Anzahl an Legierungselementen (hinsichtlich einer hochkonfigurativen Entropie) nicht die einzige Einflussgrößebei der Bestimmung von Gitterverzerrungen, dem Gefüge und der mechanischen Eigenschaften darstellt, sondern auch die Art und die Kombination der Legierungselementen einschließlich der atomaren Wechselwirkungen (d.h. Atomgrößenunterschiede) einen Effekt haben.

Contents

1. Motivation and objectives

High entropy alloy (HEA), consisting of multi-components in near- or equiatomic ratio, has been known to form a solid solution phase with simple crystal structure, such as face-centered cubic (*fcc*) and body-centered cubic (*bcc*) structures, rather than several intermetallic phases. This suggests that the high configurational entropy in HEAs can overcome the enthalpy of formation of competing intermetallic phases [1, 2, 3]. The HEAs are designed based on the concept of entropic stabilization associated with a large number of constituent elements with high concentration. As a result, the large chemical complexity in HEAs is expected to cause exceptional microstructural stability and special properties, especially mechanical properties.

Due to a large number of atom species at lattice sites in HEAs, an assumption of severe lattice distortion has been proposed [4, 5, 6, 7]. The assumption is based on the number of constituent elements. In fact, not only the number of constituent elements plays a role in a lattice distortion, but an alloy composition should be considered due to different interactions between atom species. There has been a limited number of reports to show the evidence for severe lattice distortion in HEAs. This is particularly because of the difficulties in finding suitable experimental approach to detect these distortions. Recently, the atomic pair distribution function (PDF), obtained from the Fourier transform of total scattering data, has been suggested as a powerful technique to probe the local atomic arrangements and to assess the lattice distortion in HEAs [8, 9, 10]. The diffuse intensities included in the PDF profiles obtain the information on local atomic correlation [8]. An atomic PDF is one-dimensional function which has peaks at distances describing the probability of finding an atom at a distance r in real space. The width of these PDF peaks can give information on atomic displacement correlated with lattice distortion.

As the assumption of severe lattice distortion in HEAs, the random arrangements of multiple atom species are expected to create intensive local strain field. The intensive strain fields act as strong barriers to the dislocation motions, which give rise to a significant level of solid solution hardening [11, 12]. In other words, the level of lattice distortion correlates with the level of solid solution hardening, often expected as key strengthening mechanism in HEAs.

Moreover, it is reported that the effect of work hardening is significant on the improvement of the mechanical properties. For example, in *fcc*-structured FeNiCoCrMn HEA, 50% cold working can enhance the yield strength from 200 MPa to 1000 MPa [4]. It suggests that random arrangements of multiple atom species and an assumption of lattice distortion in the HEAs strongly prohibit the dislocation motion during the plastic deformation; hence, the strength are enhanced. [1, 13]. The characterization of dislocation motion in HEAs have been addressed in the literatures [11, 13, 14]. Many studies indicate that the deformation mechanism of HEAs is similar to concentrated binary solid solution alloys [15, 16]. However, the quantitative analysis of dislocation is still needed to understand deformation behavior and correlated mechanical properties in HEAs [13].

Previous works on HEAs demonstrate that typical manufacturing routes are applied to produce the samples [1, 17, 18, 19]. Also, the high malleability is observed in the fabrication of HEAs [20]. This beneficial point facilitates to tune mechanical and other properties by controlling microstructure with a conventional process [21]. In this study, HEAs could be produced with cold crucible casting and their microstructure was modified by common fabrication methods (rolling and swaging), followed by heat treatment. The macroscopic fracture could not be observed during the production process.

Therefore, this present work aims to assess the lattice strain interacted by multiple atom species in order to correlate the mechanical properties and microstructural evolution during thermomechanical treatment.

This PhD dissertation consists of 8 chapters. Chapter 2 introduces some fundamental aspects about HEAs and their mechanical properties in a comparison with those of conventional alloys. The fundamentals also include thermodynamics and criterion of single solid solution formation in HEAs. Chapter 3 describes the experimental procedure in this work in terms of alloy preparations and characterizations.

The experimental results are presented in chapter 4 – 7. The single solid solution phase *fcc*-structured FeNiCoCrMn and *bcc*-structured TiNbHfTaZr HEAs were studied in the aspects of lattice strain, microstructure and mechanical properties. The single solid solution phase sub-alloys with a variation of compositional complexity were parallel investigated in a comparison with the

HEAs. The two different crystal structures of the HEAs are expected to obtain different structural information due to different constituent elements in each HEA. The investigation of thermal phase stability of the HEAs is discussed in chapter 4. Chapter 5 presents the assessment of lattice strain associated with multiple constituent elements in *fcc*- and *bcc*-structured HEAs. The lattice strain in micro and local scales were characterized by high energy synchrotron X-ray diffraction. The samples were prepared by the cold rolling and subsequent annealing. The samples obtained fine microstructure with strain-free grains in order to achieve high statistics, avoid fluctuation in intensity, and minimize preferred orientation on the diffraction information. Chapter 6 presents the intrinsic effect of solid solution hardening associated with multiple constituent element in HEAs. The effect of solid solution hardening was represented by hardness and tensile strength.

The effect of work hardening on the mechanical properties of the HEAs was presented in chapter 7. The rotary swaging was applied to deform the samples in order to study an accumulation of dislocation. Moreover the rotary swaging associated with large hydrostatic stresses delays brittle fracture and allows the accumulation of high plastic strain [17]. The work hardening was discussed in the correlation between mechanical properties and dislocation density accumulated after cold swaging. According to the mechanical properties strongly dependent on the microstructure, the quantitative analysis of dislocation density is important to study. Finally, the conclusions and outlook for this study are presented in chapter 8.

2. Fundamentals

2.1 Concept of high entropy alloys

High entropy alloys (HEAs) have been introduced by two independent publications in 2004 by J.W. Yeh et al. [22] and B. Cantor et al. [23]. Based on an original definition, HEAs compose of at least 5 elements with near- or equiatomic ratio and obtain a single disordered solid solution [1, 2, 3, 22]. The key characteristic of HEAs is high configurational entropy (ΔS_{conf}) driven by multiple elements. The high ΔS_{conf} stabilizes a disordered solid solution over completing intermetallic compounds [24, 25]. In fact, recent works indicate that most HEAs are not stable as single solid solution at all service temperatures [12]. The many HEAs in recent scientific reports obtain metastable solid solution phase and multiple phases can be presented [21]. The presence of multiple phases in the HEAs is not in an agreement with the original definition of the HEAs. In order to avoid the confusion in the definition, another term "complex concentrated alloys (CCAs)" has been introduced for alloy naming conversion [3, 24]. However, the single phase high entropy alloys were studied in this thesis; hence, the term "high entropy alloy" was used to call the samples.

2.1.1 Phase formation and thermodynamic

In case of excluding kinetic factors, phase formation in multiple element alloys including HEAs is thermodynamically controlled by minimizing the Gibbs free energy of mixing (ΔG_{mix}). The ΔG_{mix} is presented in following equation [26]:

$$\Delta G_{mix} = \Delta H_{mix} - T\Delta S_{mix} \quad (2.1)$$

where ΔH_{mix} is the enthalpy of mixing, ΔS_{mix} is the entropy of mixing, and T is the temperature at which different elements are mixed. The enthalpy of mixing for multiple element alloys with n elements can be determined from the following equation [27, 28]:

$$\Delta H_{mix} = \sum_{i=1, i\neq j}^{n} \Omega_{ij} c_i c_j \quad (2.2)$$

where Ω_{ij} is the regular solution interaction parameter between the i^{th} and j^{th} elements, c_i or c_j is the atomic percentage of the i^{th} or j^{th} component and $\Omega_{ij} = 4\Delta H_{AB}^{mix}$; ΔH_{AB}^{mix} is the enthalpy of mixing of binary A-B liquid alloys.

For ideal and regular solutions, the entropy of mixing is assumed to be approximately the configurational entropy (ΔS_{conf}). The configurational entropy of an n-element solution is as follows;

$$\Delta S_{mix} \approx \Delta S_{conf} = -R \sum_{i=1}^{n} c_i \ln c_i \quad (2.3)$$

where R is gas constant (8.314 J K^{-1} mol^{-1}). The configurational entropy would be the maximum for an equiatomic composition. The ΔS_{conf} of multi-principle element HEAs would higher than that of conventional alloys with one or two main element(s). The magnitude of ΔS_{conf} increases with the number of alloying element in high concentration.

The solid solution formation is determined by competition between an enthalpy term of ΔH_{mix} and an entropy term of $T\Delta S_{mix}$. It is reported that ΔH_{mix} plays an important role in phase formation in multi-component alloys similar to that of binary alloys [29]. The negative ΔH_{mix} drives the constituent elements to form intermetallic compound(s), while the positive ΔH_{mix} leads to incompatibility of constituent elements which results in separation or segregation of elements in alloys. Theoretical models and experimental results show a good agreement that solid solution is stably formed with ΔH_{mix} close to zero [12, 30]. Additionally, an equilibrium phase diagram is obtained from the calculation of thermodynamic data using the Gibbs free energy for all relevant phases. Figure 2.1 presents examples of three types of phase diagram when the values of ΔH_{mix} are negative, positive and close to zero. They show various phase transformations due to different thermodynamic properties of the alloys.

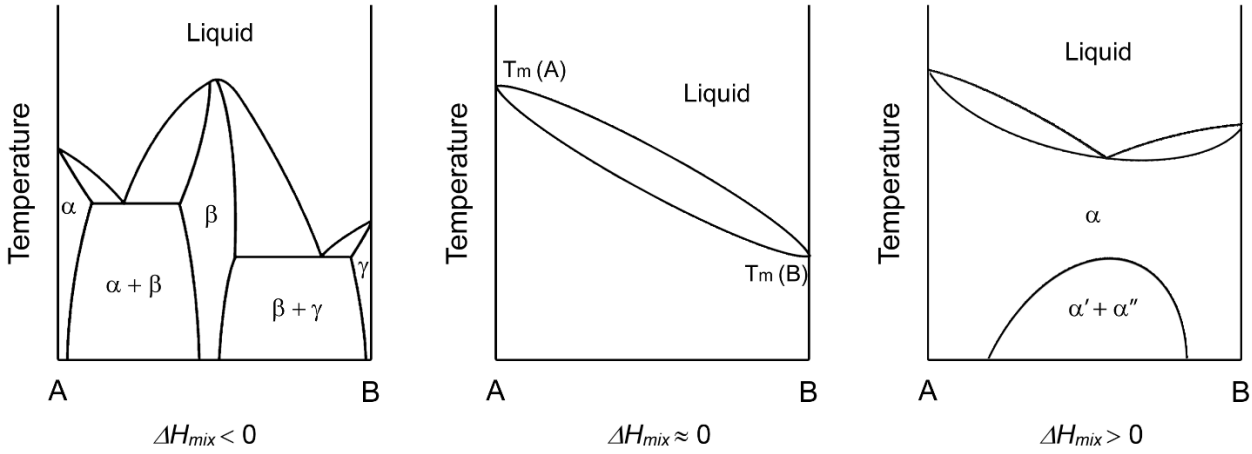

Figure 2.1 Three types of phase diagram when $\Delta H_{mix} < 0$, $\Delta H_{mix} \approx 0$ and $\Delta H_{mix} > 0$.

In HEAs, when they form a disordered solid solution phase, the multiple atom species are expected to randomly occupy the lattice sites. The atomic radius of alloying elements is an important parameter for solid solution forming and hence the phase stability [31, 32]. The large atomic size misfit increases the free-energy in the alloys, which lowers the stability of the solid solution. The Hume-Rothery rule defines that the solid solution can be formed with less than 15% atomic size misfit between alloying elements and host element in conventional alloys [33]. In HEAs, high concentration and the larger number of constituent elements limit the range of atomic size misfit at 6.6% for the borderline between disordered solid solution and other complex crystal structures [34]. The atomic size misfit (δ) can be calculated with the following equation:

$$\delta = 100\sqrt{\sum_{i=1}^{n} c_i\left(1 - \frac{r_i}{\bar{r}}\right)^2} \tag{2.4}$$

where r_i is the radius of individual atomic species, c_i is its concentration and $\bar{r}$ is the average atomic radius.

Figure 2.2 presents the phase selection under the relationship between the parameters ΔH_{mix} and δ. The solid solutions in HEAs are formed in the criterion of $-15 \leq \Delta H_{mix} \leq 5$ kJ/mol and $\delta \leq 6.6\%$. Beyond this criterion, the intermetallic compounds can be decomposed and the amorphous phase can be stable with rapid quenching.

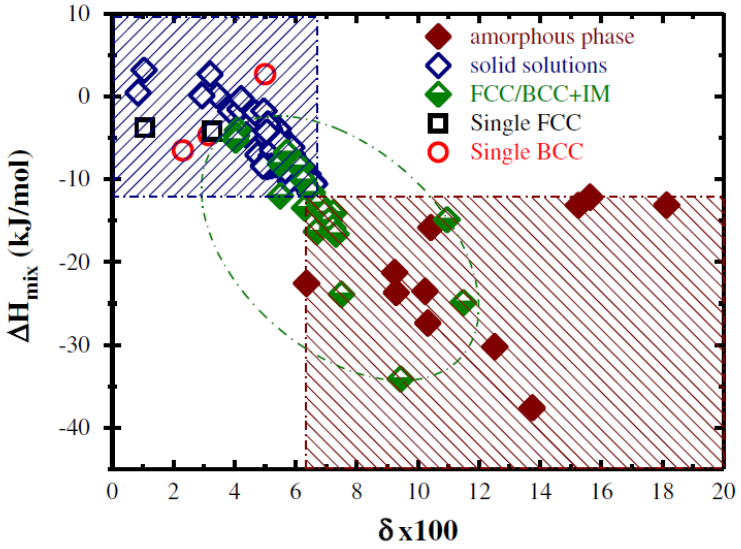

Figure 2.2 Plot between the parameters ΔH_{mix} and δ determines the phase formation. The oval zone is for mixtures of solid solutions, intermetallic compounds (IM), and metallic glasses. Taken from reference [31].

Meanwhile, the ΔS_{mix} is another parameter to be considered. The ΔS_{mix} should be high enough to stabilize the formation of solid solution against either the ordering or segregation of alloy elements [3, 30, 35, 36]. In contrast, the small ΔS_{mix} favors the formation of intermetallic compound [37]. The high ΔS_{mix} increases the randomness of alloy system and lowers the term of ΔG_{mix}. As temperature increases, the higher $T\Delta S_{mix}$ facilitates forming solid solution, which overcome the effect of ΔH_{mix}. As discussed, the ΔH_{mix} and $T\Delta S_{mix}$ are competitive parameters for solid solution formation. Y. Zhang et al. [34] proposed the parameter Ω by combining effects of ΔH_{mix} and ΔS_{mix} on the stability of multicomponent solid solution. The Ω is expressed by the following equation;

$$\Omega = \frac{T_m \Delta S_{mix}}{|\Delta H_{mix}|} \tag{2.5}$$

The melting point (T_m) of a n-element alloy can be estimated by rule of mixture, as shown below:

$$T_m = \sum_{i=1}^{n} c_i \, (T_m)_i \tag{2.6}$$

According to the equation 2.4, the Ω is always positive. The solid solution formation is favorable for high value of $T_m \Delta S_{mix}$ affected by a large number of constituent elements in case of $\Omega > 1$ [25]. X. Yang et al. [30] presented the plot between Ω and δ for different kinds of microstructures, as presented in Figure 2.3. The plot suggested that single solid solution phase would be formed under the criterion of $\Omega \geq 1.1$ and $\delta \leq 6.6$.

Based on experimental reports on the number of HEAs, only limited number of alloys (composing of at least 4 elements) can be called as a single phase solid solution for at least one processing step of sample preparation [21]; for example, FeNiCoCrMn [38, 39], FeNiCoCr [40], $FeNiCoCrAl_{0.3}$ [41], $FeNiCoCrMnAl_{0.2}$ [42], TiNbHfTaZr [43, 44], $TiZrNbMo_{0\text{-}1.5}V_{0.3}$ [45], NbMoTaW [46] and NbMoTaWV [46]. In fact, the magnitude of ΔS_{mix} may vary with temperature [47] and cahnges significantly after a first order phase transformation. It is in a good agreement with the experimental results that the most HEAs show solid solution instability at some range of temperatures [12]. Only NbMoTaWV presents a stable single solid solution phase at all temperature [30, 46, 48].

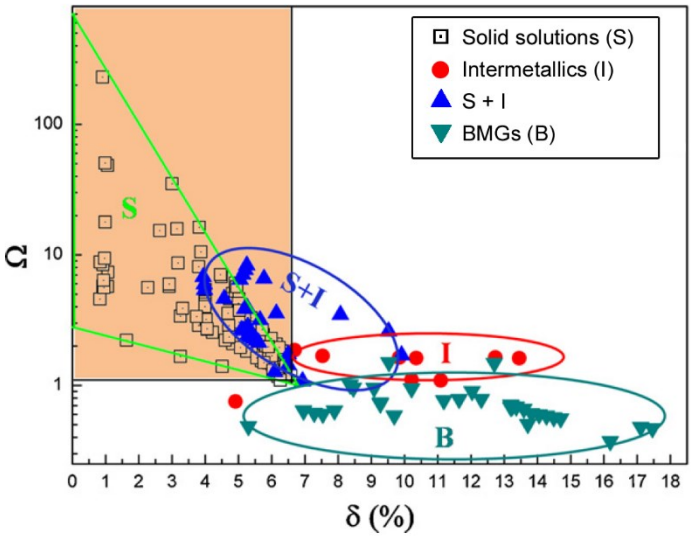

Figure 2.3 Plot between the parameters Ω and δ determines the phase formation. The regions "S", "I", "S+I" and "B" indicate a single solid solution alloys, intermetallic compound contained in alloys, the precipitation of intermetallic compounds with solid solution phase and bulk metallic glass alloys, respectively. Taken from reference [30].

2.1.2 Four core effects

In general, composition and processing determine lattice structure and microstructure, which result in properties. The high concentrations of multiple elements in HEAs contribute to unique characteristic effects on their microstructures and properties. These effects were proposed in 2006, namely as "four core effects": high entropy, sluggish diffusion, severe lattice distortion and cocktail effects [49]. Figure 2.4 demonstrates the role of each effect in the physical metallurgy of HEAs.

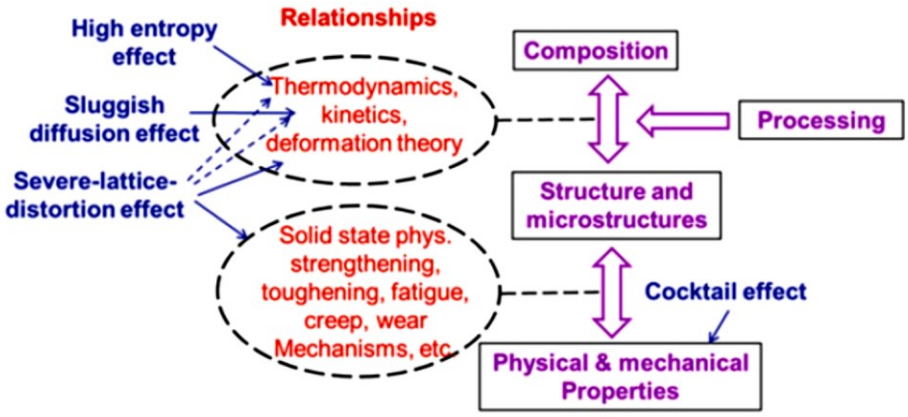

Figure 2.4 Role of four core effects in physical metallurgy of HEAs. Taken from reference [11].

High entropy effect – The high entropy effect is the key effect in the HEA via thermodynamic. As discussed previously, it is led by a large number of constituent elements in high concentration. The high entropy effect causes high possibilites to form solid solution phase in the simple form of *fcc* or *bcc* or *hcp* crystal structures [50]. The number of phase formed in HEAs is far fewer than the maximum phase number expected from the Gibbs phase rule [1, 28, 51]. This indicates that the high entropy effect increases the solubility of their solid solutions, resulting in simpler microstructure [2].

Severe lattice distortion effect – The hypothesis of severe lattice distortion in HEAs is suggested by random arrangements of multiple atom species at their lattice site, comparing with

one dominant element alloys, as illustrated in Figure 2.5. These distortions are caused by atomic size misfit, different bonding energies and different crystal structures among constituent elements [52]. Lattice distortion is related to the deformation theory, kinetics and thermodynamics. J. W. Yeh et al. [53] suggested as an evidence of intrinsic lattice distortion that peak intensities on the X-ray diffraction (XRD) of CuNiAlCoCrFeSi alloy dropped due to the large roughness of the atomic planes and the severe X-ray scattering effect. The lattice distortion is often assumed to cause high hardness and strength, especially in *bcc*-structured HEAs [34, 51, 54], also related to the slower kinetics of HEAs [55].

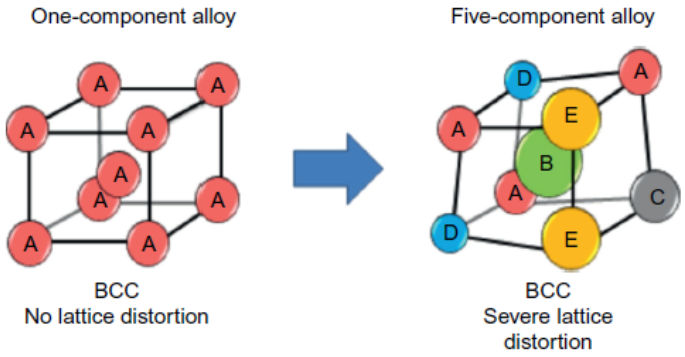

Figure 2.5 Schematic diagram of lattice distortion affected by five different atom species in *bcc* lattice. Taken from reference [2].

Sluggish diffusion effect – The sluggish diffusion in HEAs affects kinetics of phase transformation. This hypothesis is based on an experimental observation of nano-sized crystals precipitation upon cooling in CuCoNiCrAl alloy by J. W. Yeh et al. [22]. It was suggested that difficulties in substitutional diffusion and interdiffusion led to the formation of ultrafine crystallites. Recent evidence revealed that the precipitations in $Al_{0.5}$CrFeCoNiCu HEA could be formed with slow solidification rate, which is similar to the precipitation with rapid solidification [56]. It suggested that sluggish diffusion in HEAs may have a similar effect on the precipitation in samples either obtained by a furnace or rapid cooling [12, 57, 58]. K. Y. Tsai et al. [59] also verified sluggish diffusion effects through a direct measurement of diffusion coefficient in equiatomic

CoCrFeMnNi alloy. The experimental results demonstrated that the diffusion coefficients for each element in the matrix of the CoCrFeMnNi HEA were the lowest when compared with conventional crystalline metals (Figure 2.6). This effect is expected to lead exceptional high-temperature strength [16, 60], high-temperature structural stability [61, 62] and formation of nanostructures [22, 63]. In recent, based on the results from various methods approaching diffusion behavior in HEAs, the concept of "sluggish" diffusion in HEAs have been increasingly questioned [3, 12, 64]. However, it is suggested that the term "sluggish diffusion" cannot be used for all HEA.

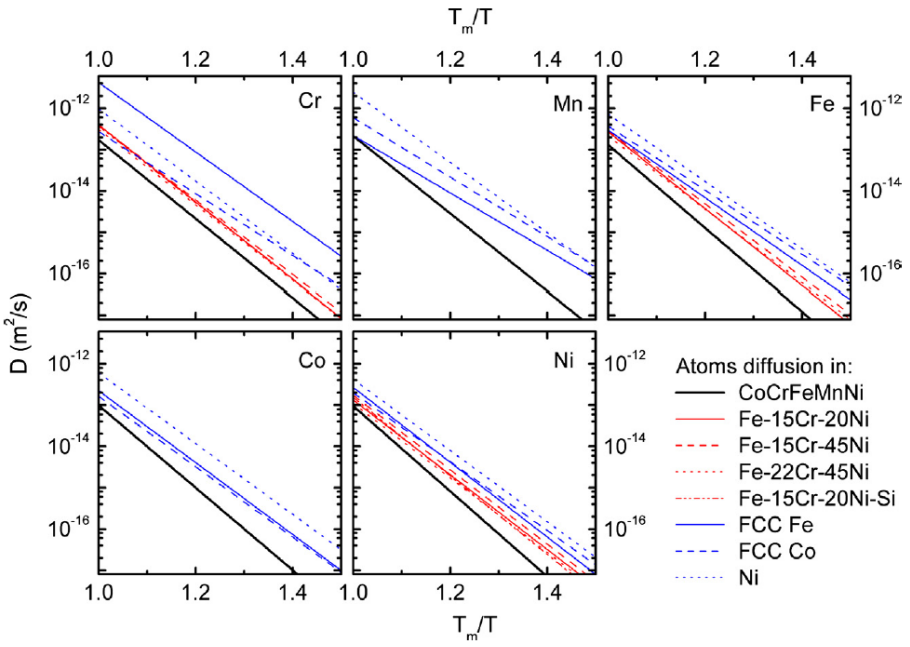

Figure 2.6 Diffusion coefficients as a function of temperature for Cr, Mn, Fe, Co and Ni in different matrixes. Taken from reference [59].

Cocktail effect – The cocktail effect is proposed by S. Ranganathan [65] to imply the enhancement of the properties depend on composition, microstructure and other features of HEAs in complicated and sensitive ways [1, 3]. This effect requires no proof because it is not a hypothesis [3]. This similar effect can be found in conventional alloys, but significant effect is observed in HEAs due to the mutual interactions among all the constituent elements.

2.2 Alloy classification of high entropy alloys

Since the first report on high entropy alloys, there have been huge number of attempts to develop the high entropy alloys based on the concept of high configurational entropy. D.B. Miracle and O.N. Senkov have made an effort to group high entropy alloys (HEAs) and complex concentrated alloys (CCAs) among 408 alloys using 37 elements [66]. Some of these elements is commonly observed in the compositions, i.e. Al, Co, Cr, Cu, Fe, Mn, Ni, Ti, Mo, Nb, V and Zr. It is also mentioned that the number of constituent element is averagely 5 - 6 for an alloy.

The alloys have been classified into three main alloy families; 3d transition metal HEAs (consisting of the 3d transition metallic elements with similar electronic configurations and atomic sizes), refractory metal HEAs (composing of refractory metallic elements), and others. In the first group of 3d transition metal HEAs, the elements having larger atomic size (such as Al, Ti, V, Mo) are also included in the alloys of this group; hence, the mechanical properties of the alloys are complicated and it is hard to obtain a clear trend. Recently, H.Y. Diao et al [13] has modified the classification by dividing the first group into two groups; namely, 3d transition metal HEAs and transition metals HEAs with larger atomic radius elements.

3d transition metal HEAs - This group is the soft solid solution HEAs, only including 3d-transition metals Co, Cr, Fe, Mn and Ni with similar electronic configurations and atomic sizes. This group contains the alloys obtaining single phase *fcc* solid solution. The classical HEA CoCrFeMnNi [39], so called as Cantor alloy, is in this group. The CoCrFeMnNi HEA was firstly experimentally investigated by B.Cantor and his student Alain Vincent [6] in 1981 and this was published in 2004 [39]. Among the alloys of their experiment with 20 elements, only $Co_{20}Cr_{20}Fe_{20}Mn_{20}Ni_{20}$ (in at%) presents single *fcc*-structured solid solution phase. Since the first report, this HEA has been intensively investigated with a particular focus on its mechanical properties and processing [16, 67]. The composition of the CoCrFeMnNi HEA has been modified for further investigations; for example, CoCrFeNi [68, 69], CoFeMnNi [70], CoCrMnNi [70], and $Co_{0.25}Cr_{0.1}Fe_2Mn_{1.35}Ni_{1.3}$ [71].

Transition metal HEAs with larger atomic radius elements - The combination between transition metals and the larger atomic size elements (such as Al, Ti, V, Mo) typically forms duplex

fcc + *bcc* solid solution phases. These alloys in this group are commonly Al-containing alloys; excessive alloying with Al can cause changes in both microstructure and mechanical properties. The precipitation of intermetallic compounds i.e. L12, σ and laves phases can occur. The examples of duplex *fcc* + *bcc* solid solution HEA are $Al_xCoCrCuFeNi$ [22], $Al_xCoCrFeNi$ [55, 72] and $AlCoCrFeNiTi_x$ [51]. Alloying with refractory elements can result in single *bcc* solid solution phase; i.e. AlNbTiV [73] and AlNbTaTiV [74].

Refractory metal HEAs - This alloy family is developed for using in high temperature applications. The *bcc* solid solution phase is commonly formed in this group. This alloy family usually combines at least 4 elements from the 9 refractory elements: Cr, Hf, Mo, Nb, Ta, Ti, V, W, and Zr [24, 25]. NbMoTaW and VNbMoTaW were firstly proposed by O. N. Senkov et al. [46]. These two alloys with single ingle *bcc* solid solution phase have extremely high yield strength of over 400 MPa at 1600°C [48]. In contrast to the Ni-base superalloy Inconel 718, it significantly softens above 600°C. However, the NbMoTaW and VNbMoTaW HEAs have a limited compressive plasticity about 2 – 3% at room temperature [48], which is similar to conventional refractory alloys [75]. Therefore, other compositions of refractory HEAs have been investigated to increase the ductility. It was reported that the compressive strain of $HfMo_xNbTaTiZr$ ($x < 1$) [76] and HfNbTaZrTi [43] at room temperature is above 50%. This alloy group also includes $Hf_{0.5}Nb_{0.5}Ta_{0.5}Ti_{1.5}Zr$ [77] and HfNbTiZr [78].

Besides the alloys mentioned above, *hcp* solid solution alloys were recently developed. It was suggested that HEAs based on rare earth elements can be formed with a HCP structure [25]. Additionally, it was reported that the combinations of at least 4 lanthanide (4f) elements such as Dy, Gd, Lu, Tb and Tm form single *hcp* solid solution HEAs [79]. The example alloys are DyGdLuTbY and DyGdLuTbTm.

2.3 Mechanical properties of high entropy alloys

HEAs present high strength and reasonable ductility at room and elevated temperatures [14, 48, 80, 81]. The mechanical properties of HEAs are resulted by a mutual interaction between

multiple principle elements, unlike conventional alloys which their mechanical properties is mainly dictated by one principle element. It is known that the multiple element HEAs could easily form simple solid solutions with or without nano-precipitates during solidification [1, 63]. Thus, multiple element solid solutions play a vital role in the mechanical properties of HEAs [70, 76, 82, 83] and cause superior mechanical properties when compared to conventional alloys. It is believed that the high degree of solid solution hardening in HEAs is related to lattice distortion. C. M. Lin et al. [84] studied the solid solution hardening by the addition of Al to single *bcc*-structured $Al_xHfNbTaTiZr$ HEA as shown in Figure 2.7. This large effect of hardening is attributed to the strong bonding of Al and other elements in combination with the effect of atomic size misfit. These conclusions are similar to a theoretical study of O. N. Senkov et al. [43] that high degree of solid solution hardening in HfNbTaTiZr is resulted by atomic size misfit and modulus misfit of its constituent atoms. However, it is reported that the degree of solid solution hardening in *fcc*-structured HEA i.e. CoCrFeMnNi is relatively lower due to its smaller lattice distortion [1]. Besides the intrinsic hardening effect, the microstructure features i.e. grain size and secondary phase, influence the mechanical properties of HEAs, similarly to conventional alloys.

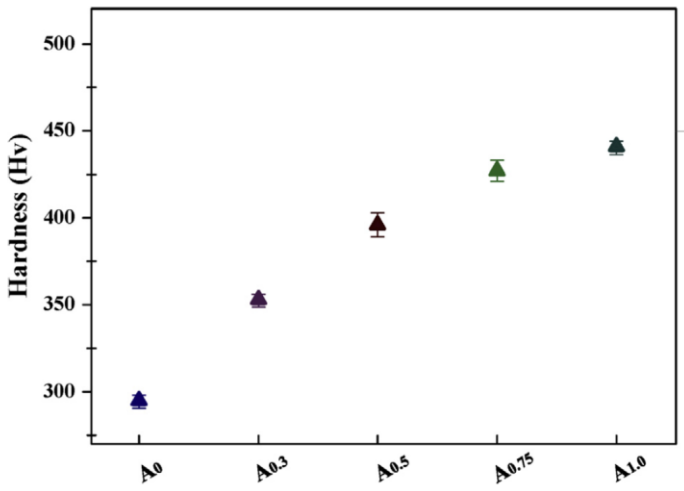

Figure 2.7 Effect of Al content on hardness of single phase $Al_xHfNbTaTiZr$ HEA. Taken from reference [84].

Figure 2.8 presents the hardness values of 20 HEA systems in a comparison with those of conventional alloys. In each alloy system, the hardness values widely vary depending on chemical compositions, fabrication methods, and following heat-treatment processes. It is mentioned that the hardness values of HEAs mainly composed of *fcc*-structured solid solution (i.e. CoCrFeNi, CoCrCuFeNi and CoCrFeMnNi) are relatively low. In the alloys with addition of Ti and Al, the hardness values can be enhanced by the formation of hard secondary phases. The refractory HEAs are based on *bcc*-structured solid solution alloys. For example, the hardness values of HfNbTaTiZrTi, MoNbTaW, MoNbTaVW, $AlMo_{0.5}NbTa_{0.5}TiZr$ and $Al_{0.4}Hf_{0.6}NbTaTiZr$ alloys are 390, 454, 535, 591 and 500 HV, respectively [43, 46, 85]. It is noted that the crystal structure types are the dominant factor for characterizing the strength or hardness of HEAs [86, 87, 88]. It is reported that *fcc*-structured HEAs present low strength and high plasticity, and *bcc*-structured HEAs show high strength and low plasticity as mentioned previously. The valance electron concentration (VEC) has an effect on crystal structure of solid solution phase. S. Guo [89] reported that *fcc* phases were stable at VEC > 8 and VEC < 6.87 stabilized *bcc* phases.

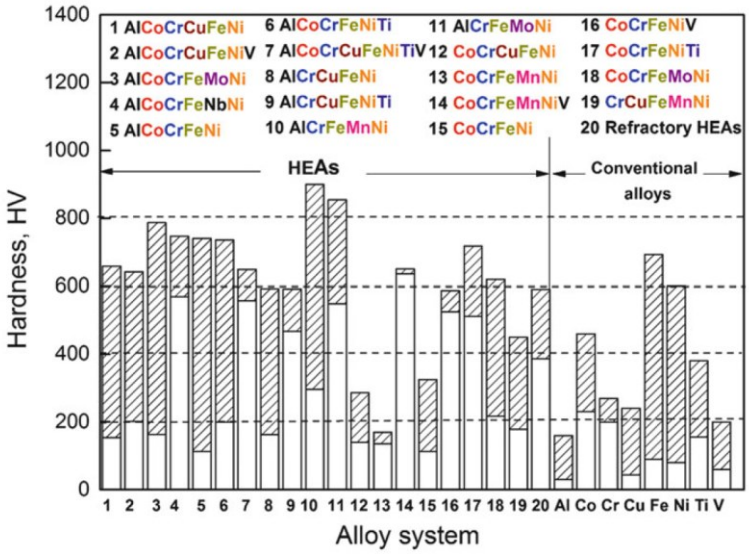

Figure 2.8 Hardness values of 20 most studied HEA systems, compared with conventional alloys; Al-, Co-, Cr-, Cu-, Fe-, Ni-, Ti-, and V-based alloys. The white regions of the bars represent the minimum hardness values and the hatched regions indicate the variable range for each alloy system. Taken from reference [1].

M. C. Gao et al. [1] summarized the published tensile information of HEAs as presented in Figure 2.9. It suggests that the HEAs present a wide range of mechanical properties. The tensile yield stresses of AlCoCrCuFeNi and Al0.5CoCrCuFeNi are comparable to Ti-6Al-4V and Inconel 713. The ductilities of CoCrFeNi and CoCrFeMnNi HEAs are remarkably better than the conventional alloys. In addition to *bcc*-structured HEAs, the HfNbTaTiZr HEA shows the tensile yield stress of approximately 1200 - 1300 MPa and a range of tensile ductility between 2 – 10% depending on the processing route [90]. Its mechanical properties are likely better than Inconel 713 and other conventional alloys.

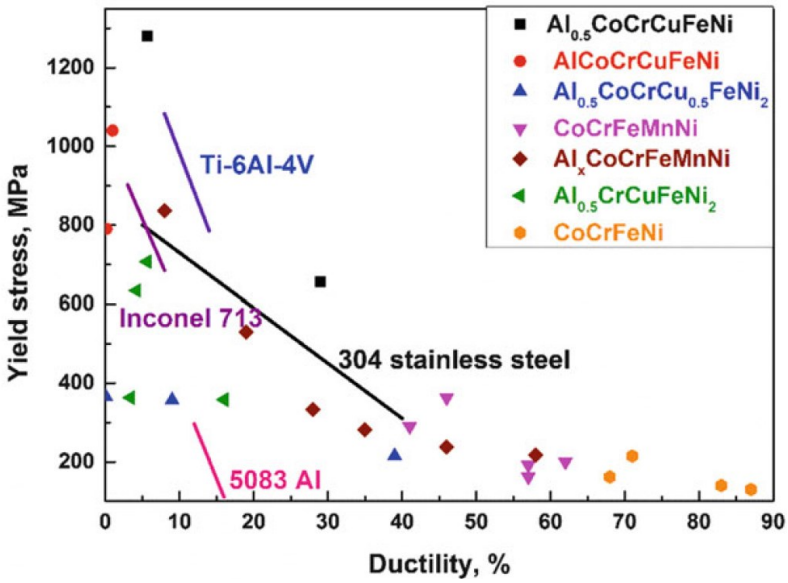

Figure 2.9 Relationship between yield stress and ductility of HEAs at room temperature in comparison with conventional alloys; 304 stainless steel, Ti-6Al-4V, Inconel 713, and 5083 aluminum alloy. Taken from reference [1].

Besides the exceptional strength, HEAs have also shown high ductility, good work hardening and plasticity. These combinations of mechanical properties including strength and hardness are attractive to use HEAs as structural materials for future applications. It is consistent with the conventional alloys that HEAs with *fcc* structure are more ductile than HEAs with *bcc* structure [91]. The high ductility and large deformability of *fcc*-structured HEAs (such as

FeNiCoCrMn) are often explained by low stacking fault energy [1]. Numerous macro slip bands are formed during deformation, which is evident to the extensive ductility for *fcc*-structured HEAs [92]. Although most of reported HEAs with *bcc* structure has limited ductility at room temperature [13, 93], the equiatomic HfNbTaTiZr HEA and some of its derived compositions obtain large plasticity [13]. This large plasticity is attributed to dislocation movement and pile-ups, which is observed by TEM investigation [78]. The previous investigations suggest that the ductility of HEAs is strongly response to the chemical composition and phase structure [91].

3. Experiments

3.1 Alloy preparation

3.1.1 Alloy selection

This study focused on the investigation of single *fcc*-structured and *bcc*-structured solid solution phase high entropy alloys (HEAs). The equiatomic FeNiCoCrMn HEA was investigated for a *fcc*-structured solid solution alloy and the equiatomic TiNbHfTaZr was studied for a *bcc*-structured solid solution alloy. In order to study the effect of a variation of compositional complexity, the single solid solution phase sub-alloys (namely quaternary, ternary and binary alloys) including unary samples were carefully selected with considerations of literature reviews, phase diagrams and experimentally results. For a selection of *fcc*-structured sub-alloys, Figure 3.1 presents the possible phase formation of the sub-alloys and pure metal subsets of the equiatomic FeNiCoCrMn HEA, which is experimentally investigated by Z. Wu et al. [70]. Therefore, the equiatomic FeNiCoCr, FeNiCo, FeNi sub-alloys and pure Ni were systematically studied in a comparison with the FeNiCoCrMn HEA. For a selection of *bcc*-structured sub-alloys, phase formation of some alloys is experimental investigated by arc-melting and homogenization, and the others of the sub-alloys were checked with the theoretical work of Y. Lederer et al. [94]. Figure 3.2 presents the possible phase formation of the sub-alloys and pure metal subsets of the equiatomic TiNbHfTaZr HEA. The equiatomic TiNbHfTa, TiNbHf, TiNb sub-alloys and pure Nb were selected for studying a variation of compositional complexity in the TiNbHfTaZr HEA.

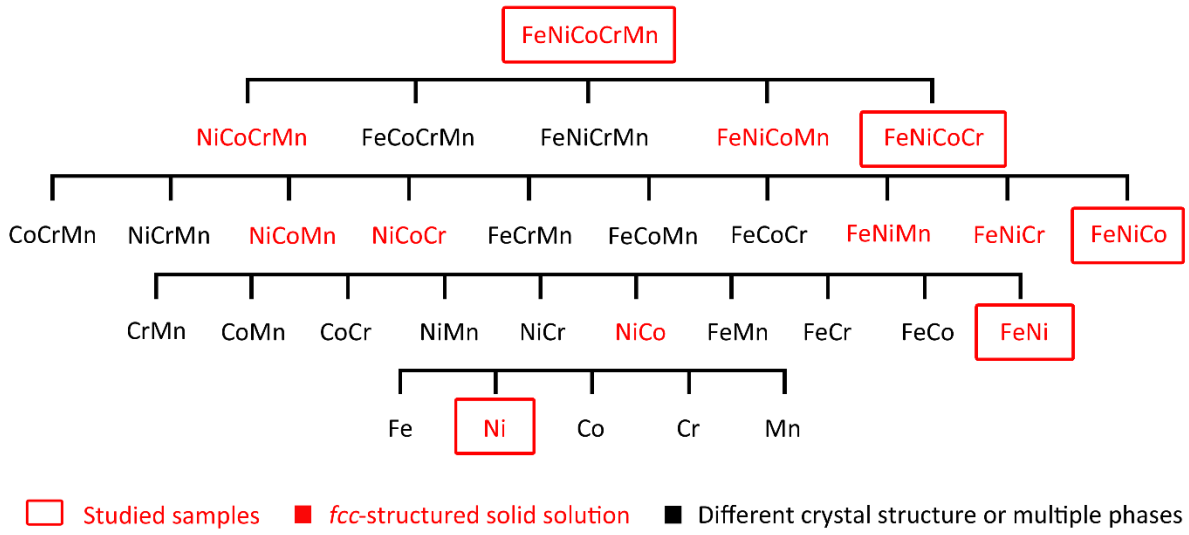

Figure 3.1 Possible phase formations of the sub-alloys and pure metal subsets of the equiatomic FeNiCoCrMn HEA. The data is collected form experimental results of Z. Wu et al. [70].

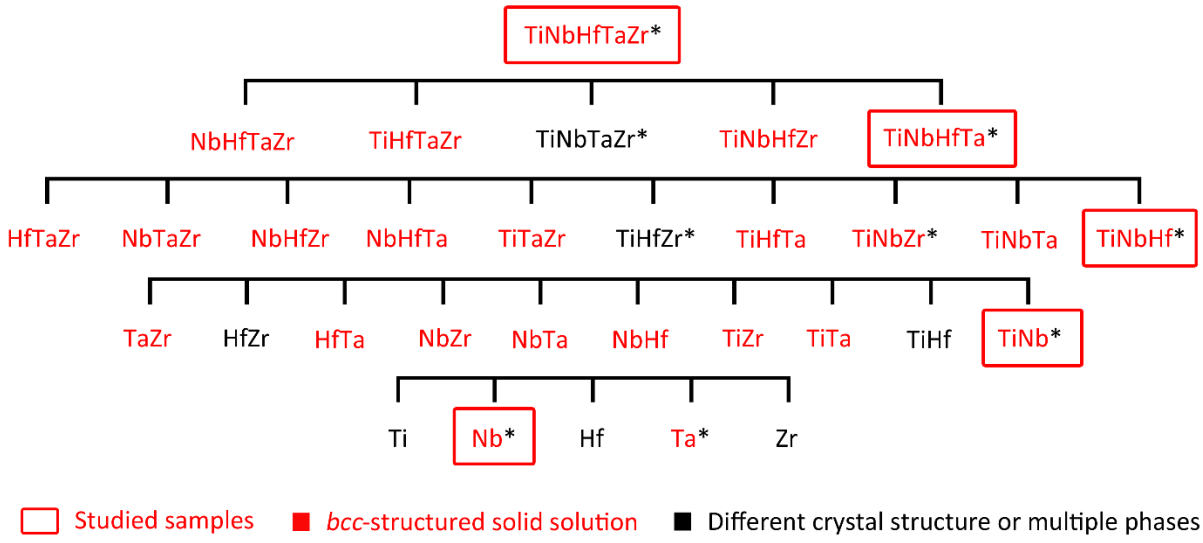

Figure 3.2 Possible phase formations of the sub-alloys and pure metal subsets of the equiatomic Zr HEA. Phase formations of some sub-alloys (masked with *) are experimentally investigated by arc-melting and homogenization, and the others are collected from the theoretical work of Y. Lederer et al. [94].

Table 3.1 shows the alloy composition of the samples in this study. The samples in this this study were divided into three groups; (1) equiatomic *fcc*-structured alloys, (2) equiatomic *bcc*-structured alloys and (3) non-equiatomic *bcc*-structured alloys. The group of the equiatomic *fcc*-structured alloys composed of FeNiCoCrMn HEA and its sub-alloys (FeNiCoCr, FeNiCo, FeNi and Ni), while the group of the equiatomic *bcc*-structured alloys consisting of TiNbHfTaZr HEA and its sub-alloys (TiNbHfTa, TiNbHf, TiNb and Nb). As- received 2 mm diameter Nb rod was used during this study. The compositions of non-equiatomic TiNbHfTaZr alloys were modified based on the TiNbHfTaZr HEA for further investigation of the solid solution hardening; $Ti_{30}Nb_{30}Hf_5Ta_{30}Zr_5$, $Ti_{20}Nb_{18}Hf_{20}Ta_{18}Zr_{24}$ and $TiNbHfTaZrMo_{0.25}$ (in atomic ratio).

Table 3.1 Studied samples in this work are classified into three groups; namely (1) equiatomic *fcc*-structured alloys, (2) equiatomic *bcc*-structured alloys and (3) non-equiatomic *bcc*-structured alloys.

Equiatomic *fcc*-structured alloys	Equiatomic *bcc*-structured alloys	Non-equiatomic *bcc*-structured alloys
FeNiCoCrMn	TiNbHfTaZr	$Ti_{30}Nb_{30}Hf_5Ta_{30}Zr_5$
FeNiCoCr	TiNbHfTa	$Ti_{20}Nb_{18}Hf_{20}Ta_{18}Zr_{24}$
FeNiCo	TiNbHf	$TiNbHfTaZrMo_{0.25}$
FeNi	TiNb	
Ni	Nb	

3.1.2 Melting and casting

Prior alloying, elements with purities of 99.9 wt% or higher were prepared and used for casting 20 - 30 g ingots. The amounts of the constituting elements were weighed using a Mettler Toledo XPE26 with experimental accuracy of ± 0.01 g. Master alloy ingots were prepared in arc melter (Edmund Bühler GmbH) under a purified Ti-gettered argon (Ar) atmosphere on a water-cooled copper substrate. A schematic illustration of the arc melter is shown in Figure 3.3. The pre-alloyed ingots were flipped over and remelted at least 3 times to ensure chemical homogeneity.

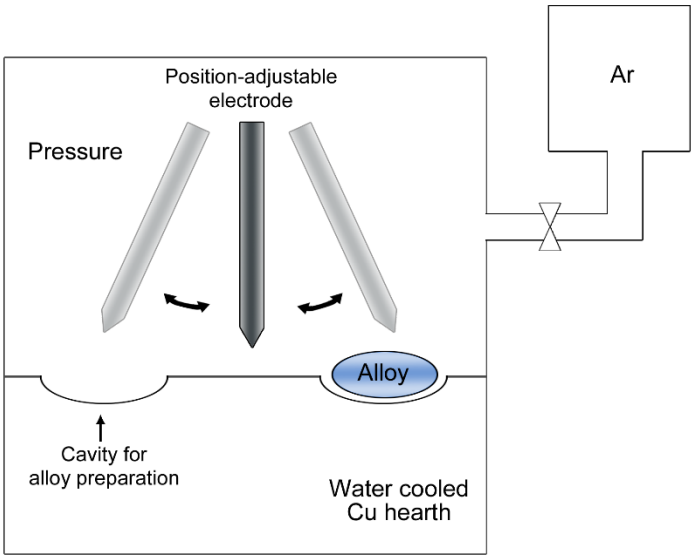

Figure 3.3 Schematic illustration of the arc melting instrument combined with a suction facility at IFW-Dresden.

Subsequently, an in house built cold crucible device as sketched in Figure 3.4 (a) was used to cast rods. The ingots were melted with a high frequency inductive heating and levitated off in a Ti-gettered Ar atmosphere. A fast-moving stick was inserted from below into the mold in order to pull casting rods out of the levitated melt into a water-cooled Cu mold. During melting, the Cu crucible was actively cooled by water. Figure 3.4 (b) presents the cast rod with 6 mm diameter and 80 – 100 mm length. The conical part was removed from each rod before further processing. The non-equiatomic *bcc*-structured alloys were investigated in the form of ingot. The casting was technically supported by S. Donath in Institute for Complex Materials (IKM), IFW-Dresden and C. Blum in the Institute for Solid State Research (IFF), IFW-Dresden.

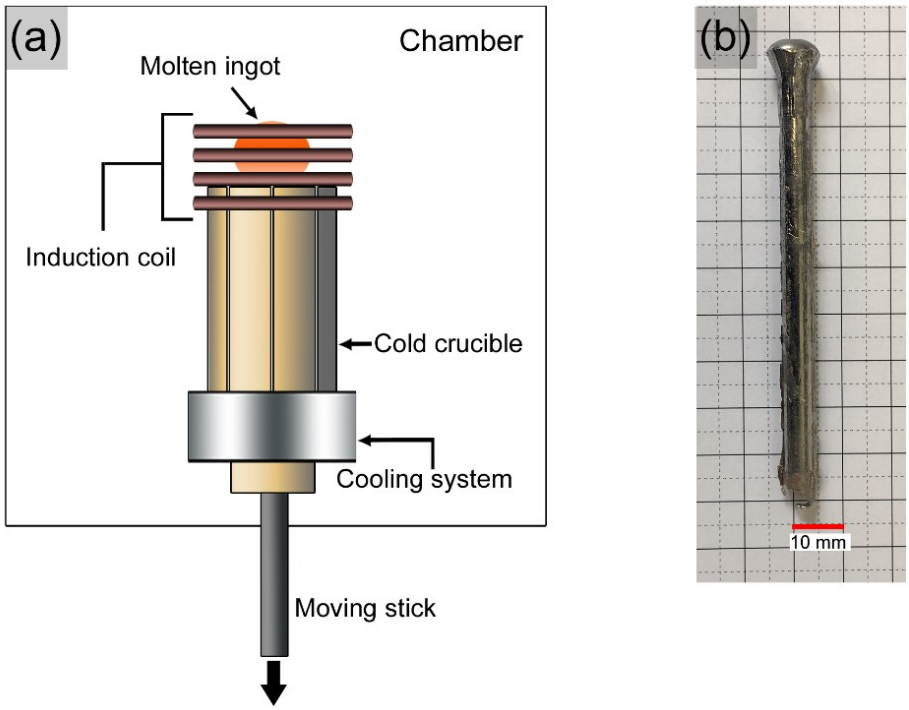

Figure 3.4 (a) Schematic illustration of the cold crucible device at IFW-Dresden and (b) sample rod cast by cold crucible method.

3.1.3 Thermomechanical treatment

After casting, the cast samples were subjected to thermomechanical treatment for specific purpose of characterization. Figure 3.5 presents a schematic illustration of thermomechanical treatment for the samples after casting. The diagram indicates three states of treatment; (1) as-homogenized, (2) as-swaged or as-rolled and (3) as-annealed state.

Due to non-equilibrium solidification during the casting, dendritic segregation was observed in the as-cast microstructures. The homogenization treatment was used to improve chemical homogeneity throughout the samples and the as-homogenized samples were used as starting samples for the investigation in this work. In order to characterize lattice strain with the large number of structural data, the samples should obtain a fine microstructure. Hence, plastic deformation was performed to refine microstructure and subsequent annealing was used to induce

the nucleation of defect-free grains for avoiding textural effect on x-ray diffraction patterns. Furthermore, the as-annealed microstructures should obtain similarly an average grain size in order to exclude the grain size effect on the investigation of lattice strain and solid solution hardening. The conditions of each processing step is described as following paragraphs.

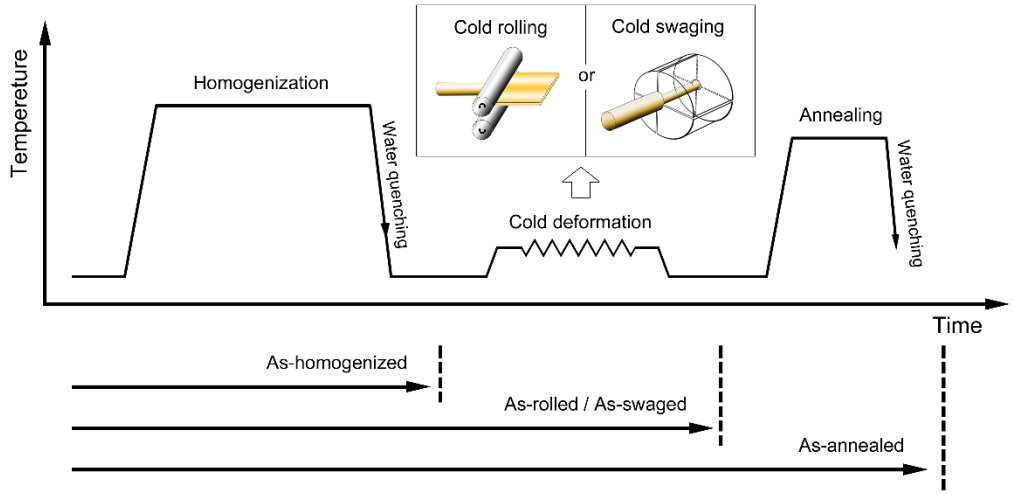

Figure 3.5 Schematic illustration of thermomechanical treatment for the sample preparations after casting.

Homogenization

After casting, the SiC papers were used to remove casting defects on the surface and to produce smooth surface. The cast rods were finished by grinding with approximately 55 mm diameter, followed by cleaning with ethanol. The rods were subsequently encapsulated in quartz tubes evacuated and backfilled with 150 mbar of Ar prior to homogenization. The samples were subjected to high temperature annealing followed by water quenching. After cooling down to room temperature, the samples were taken out by breaking the quartz tubes and then possible oxide layer was removed by grinding with 1200 grit SiC paper for subsequent studies and processing. The conditions of homogenization were different depending on the alloy compositions. The FeNiCoCrMn, FeNiCoCr, FeNiCo and FeNi alloys were homogenized at 1273 K (1000 °C) for 12 hours. Ni sample did not undergo homogenization. The TiNbHfTaZr, TiNbHfTa, TiNbHf and

TiNb alloys were homogenized at 1373 K (1100 °C) for 40 hours of homogenization. The ingots of $Ti_{30}Nb_{30}Hf_5Ta_{30}Zr_5$, $Ti_{20}Nb_{18}Hf_{20}Ta_{18}Zr_{24}$ and $TiNbHfTaZrMo_{0.25}$ were homogenized at 1373 K for 32 hours followed by water quenching.

Cold plastic deformation

In this study, plastic deformation was performed at room temperature in order to limit oxidation contamination. Especially, the *bcc*-structured samples, which contain Ti element, are sensitive to oxidation. In this work, cold rolling and cold rotary swaging were carried out to fabricate the samples.

Cold rolling was used to deform the samples into the form of plate for tensile testing. The as-homogenized rods of 5.5 cm diameter were rolled by 10% thickness reduction per step, at room temperature, until 1 mm thickness of plates. No cracking was observed in the samples.

Cold rotary swaging was used to fabricate the samples into the form of rod for compression testing. The as-homogenized rods were cold swaged by rotary swaging machine (HMP Heinrich Müller Maschinenfabrik GmbH.). Four dies in the machine are used to hammer a round workpiece into a smaller diameter by moving around the center. A cross sectional area reduction of about 19% per step was applied. The as-swaged samples in this thesis were done at the range of 45 - 90% cross sectional area reduction.

Figure 3.6 shows the rolling machine and the rotary swaging. The cold plastic deformation was technically supported by D. Seifert in Institute for Metallic Materials (IMW), IFW-Dresden.

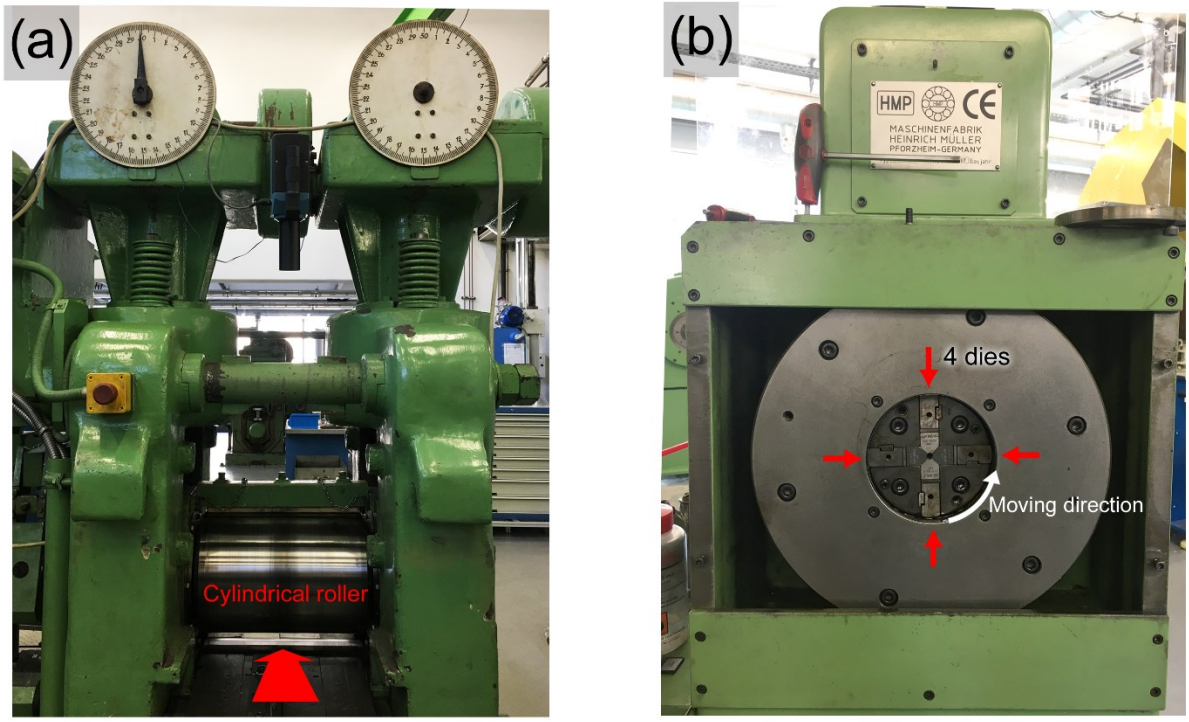

Figure 3.6 (a) Rolling machine and (b) rotary swaging machine at the IFW-Dresden.

Annealing

Prior to annealing, as-deformed samples were cleaned by ethanol in an ultrasonic bath to remove surface contaminations obtained during cold deformation. The as-deformed samples encapsulated in the quartz tubes were subjected to high temperature of annealing. Temperature and time of annealing for each composition were designed by literature surveys and experimental observations in order to obtain similar grain sizes for all compositions. Table 3.2 presents the condition of annealing for each composition. After annealing, the samples were quenched into water by breaking the quartz tubes.

Table 3.2 Annealing conditions for each composition.

fcc samples	Annealing condition	*bcc* samples	Annealing condition
Ni	1073 K, 1 hour	Nb	1223 K, 1 hour
FeNi	1073 K, 2 hours	TiNb	1223 K, 1 hours
FeNiCo	1073 K, 2 hours	TiNbHf	1223 K, 3 hours
FeNiCoCr	1223 K, 6 hours	TiNbHfTa	1223 K, 5 hours
FeNiCoCrMn	1223 K, 6 hours	TiNbHfTaZr	1223 K, 5 hours

3.2 Sample characterization

3.2.1 Chemical analyses

In order to examine the actual chemical composition of the samples before and after the thermomechanical treatment, chemical analyses were performed by using an inductively coupled plasma with optical emission spectrometry (ICP-OES: IRIS Intrepid II XUV, Thermo Fisher Scientific GmbH). Additionally, carrier gas hot extraction method (CGHE: LECO US TC-436 DR) was used to analyze the oxygen content in as-homogenized samples. The chemical analysis was technically supported by A. Voß and H. Bußkamp in Institute for Complex Materials (IKM), IFW-Dresden

3.2.2 Differential scanning calorimetry (DSC)

The thermal phase stability of as-homogenized samples was examined by a differential scanning calorimeter (DSC: Netzsch DSC-404C). The examination was performed between room temperature and 1500 K, which covers the temperature ranges used during the thermal treatment. A 12 – 15 mg test piece was measured using Al_2O_3 crucible. The measurements were carried out with heating and cooling rates of 20°C/min in a continuous Ar-flow. The investigation of the

thermal phase stability of the samples was technically supported by B. Bartusch in Institute for Complex Materials (IKM), IFW-Dresden.

3.2.3 Scanning electron microscopy and microstructural analyses

The samples after each processing step (as-cast / as-homogenized / as-deformed (as-swaged and as-rolled) / as-annealed states) were cut by an abrasive wheel saw using a SiC blade. The cut samples were hot embedded with red phenolic powder. The embedded samples were ground with sequence of 320, 600, 1200, 2400 and 4000 grit size of SiC paper. After grinding, the samples were polished with 0.3, 0.1 and 0.25 μm of diamond suspension, respectively. In addition to EBSD analysis, the samples were finalized by polishing with colloidal silica (particle size 0.05 mm) on a vibratory polisher (Buehler Vibromet 2).

A scanning electron microscopy (SEM: Zeiss Gemini 1530) was used to observe the microstructures. An energy-dispersive X-ray spectrometer (EDX: Bruker XFlash 4010) equipped with the SEM were used to examine the chemical composition of phases and samples.

The microstructures after thermomechanical treatment were characterized by electron backscatter diffraction (EBSD: Bruker e-Flash HR detector) equipped with the SEM. Grain size, twin boundary density and residual strain were quantitatively analyzed with EBSD post-processing the HKL CHANNEL 5 software (Oxford instruments). The EBSD maps with 0.5 – 1.0 μm step size obtained at least 500 grains were acquired from each sample. A grain was defined as an aggregate of neighboring data points having relative misorientations smaller than 2°. A critical misorientation angle of $\theta \geq 10°$ was used for grain size determination. Σ3 twin boundaries with a misorientation angle were not counted as grain boundaries for grain size determination. The twin boundaries were determined by the calculation of the $\Sigma 3^n$ (n = 1, 2, 3) coincidence-site lattice (CSL) boundaries. The deformed, substructured and undeformed (recrystallized) fractions was evaluated by misorientation distribution. If the internal average misorientation angle within the grain exceeded the minimum angle (2°) to define a subgrain, the grain was classified as being “deformed”. If grains consist of subgrains whose internal misorientation was under 2° but the

misorientation from subgrain to subgrain was above 2°, these grains were classified as "substructured". The rest of grains was classified as "undeformed grains".

3.2.4 X-ray diffraction (XRD)

The X-ray diffraction (XRD) in Bragg-Brentano geometry was carried out to analyze phase formation in as-cast and as-homogenized samples. The phase identification was examined by using a Panalytical X'pert Pro diffractometer using CoKα radiation (λ = 1.78897 Å), equipped with a sample spinner. The diffractometer was operated at a voltage of 40 kV and a current of 40 mA. The Bragg intensities were obtained at 2 theta (2θ) between 20 and 100 degrees with a step size of Δ2θ = 0.017 ° and an exposure time per step of 500 s.

3.2.5 High energy synchrotron X-ray diffraction

In order to analyze local structure of the samples, the high energy synchrotron X-ray diffraction was performed in transmission geometry at E = 60 keV (λ = 0.2067150 Å) with assistance of Dr. J. Bednarčik at High Resolution Powder Diffraction Beamline P02.1, PETRA III, DESY in Hamburg, Germany. Figure 3.7 shows the schematic of the experiment. A studied sample was a long rectangular rod with dimension of 1 x 1 x 25 mm^3. During the measurement, the samples were spin for increasing the scattering statistic.

The high energy synchrotron X-ray diffraction allows the assessment of local structural information of the samples due to high statistic counting associated with high intensity of a synchrotron beam [95]. In the study with the high energy synchrotron X-ray diffraction, the diffraction data is simply given as a function of the scattering vector (Q);

$$Q = \frac{4\pi \sin\theta}{\lambda} \tag{3.1}$$

where θ is the diffraction angle and λ is the wavelength of the radiation. From the equation 3.1, the parameter Q is independent on the wavelength (λ) but the value of 2θ is dependent on the

wavelength. However, the diffraction data as a function of Q and 2θ was used to be analyzed in this work. The lattice strain in micro and local scales was analyzed on high energy synchrotron X-ray diffractions with different experimental setting. The diffraction data with Q_{max} = 12 Å^{-1} of experimental setting was used to investigate the micro lattice strain with Williamson-Hall method. The diffraction data with Q_{max} = 26 Å^{-1} was performed to analyze the local lattice strain with pair distribution function (PDF) [8].

The two-dimensional diffraction patterns were integrated to one-dimensional patterns by using Fit2D [96] and Python (Python Software Foundation, https://www.python.org) software packages. A standard CeO_2 powder sample was measured in order to calibrate a condition of measurement.

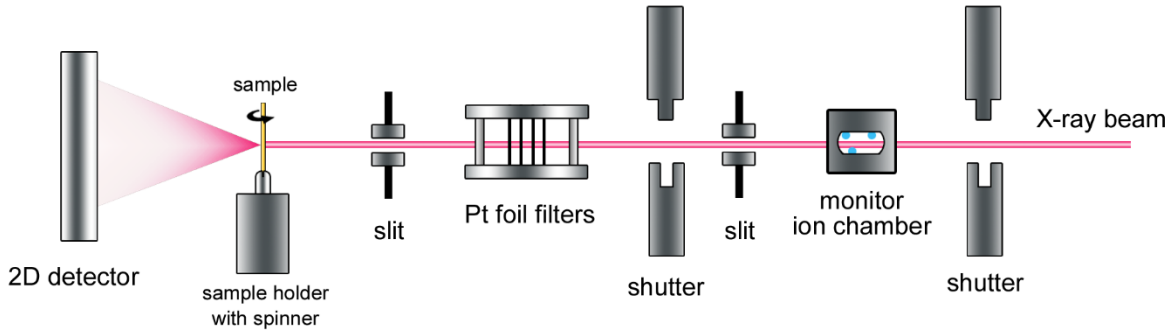

Figure 3.7 Schematic of High Resolution Powder Diffraction Beamline P02.1 of DESY in Hamburg, Germany equipped with sample spinner.

Williamson-Hall method

Micro lattice strain arising from crystal imperfections and distortion [97] can be extracted from peak broadening on Bragg data of XRD patterns with Williamson-Hall method [98, 99]. The synchrotron XRD diffraction data can obtain high statistics from a large number of grains due to a high intensity and penetration of the synchrotron beam into the samples. In this thesis, micro lattice strain affected by interactions between atoms in a solid solution phase was investigated in

the rolled samples after annealing as will be discussed in chapter 5. Also, effects of deformation on lattice strain were studied in as-swaged samples as will be demonstrated in chapter 8.

Williamson and Hall [100] suggested that the crystalline size (D_v) and lattice strain (ε_{str}) leads to a broadening of the diffraction peaks as shown in the following equations:

$$\beta_D - \beta_{inst} = \beta_{size} + \beta_{strain} \quad (3.2)$$

$$(\beta_D - \beta_{inst})\cos\theta = \lambda/D_v + 4\varepsilon_{str}(\sin\theta) \quad (3.3)$$

where β_D is an integral breadth of Bragg peak (in radians 2θ), and β_{inst}, β_{size} and β_{strain} are the integral breadths dependent on instrumental, grain size and strain effects. The equation 3.2 suggests that the breadth of the Bragg peak is a combination of both instrument and sample dependent effects. In this study, the instrumental broadening was determined upon the diffraction patterns of LaB_6. From the equation 3.3, namely the Williamson-Hall plots, a linear relationship between $(\beta_D - \beta_{inst})\cos\theta$ and $4\sin\theta$ can be plotted, By fitting the data, the crystalline size (D_v) was estimated from the y-intercept, and the micro lattice strain (ε_{str}) was derived from the slope of the fit line.

Pair distribution function (PDF)

Diffuse scattering intensities on total diffraction patterns allow assessing a local atomic arrangement deviating from average structural information reflected in the Bragg intensities [12]. A wide angular range of Q provided a maximum possibility to obtain high resolution of the diffuse intensity. In this work, a local lattice strain was investigated in the rolled sample after annealing by pair distribution function (PDF).

In this study, the reduced pair distribution function (PDF) was obtained from a total scattering pattern using PDFgetX3 software [101]. The reduced pair distribution function, $G(r)$ is derived from the pair distribution function, $g(r)$. The $G(r)$ has remarkable benefits and is widely used [102]. The $G(r)$ is most directly related to the intensity data; thus $G(r)$ include the average number density, ρ_0. In contrast, it requires to assume a value of ρ_0 for obtaining the $g(r)$. The PDF,

G(r), is processed by Fourier transforms of structure function, *S(Q)*, as shown in the following equation;

$$G(r) = 4\pi r[\rho(r) - \rho_0] = \frac{2}{\pi}\int_0^\infty Q[S(Q)] - 1]sin(Qr)dQ \quad (3.4)$$

where $\rho(r)$ is the microscopic pair density, *S(Q)* is the total structure function related to only the coherent/elastic part of the scattered X-ray intensities. The PDF profile included both the Bragg and diffuse components [8, 10, 103]. The PDF yields the probability of finding a pair of atoms separated by a distance *(r)*, including information on the local environment surrounding each atom [104]. As illustrated in Figure 3.8, a one-dimension PDF profile presents the peaks identifying the pairs of atoms corresponding to interatomic distances. The width of the PDF peaks is proportional to number of atoms finding and the distribution of distances for the given atomic pair due to dynamic and static atomic displacements [10]. In HEAs, the multiple atom species leads to complex atomic arrangement due to differences in atomic size and electronic structure. These differences are expected to be attributed to the PDF peaks broadening, which implies the lattice distortion.

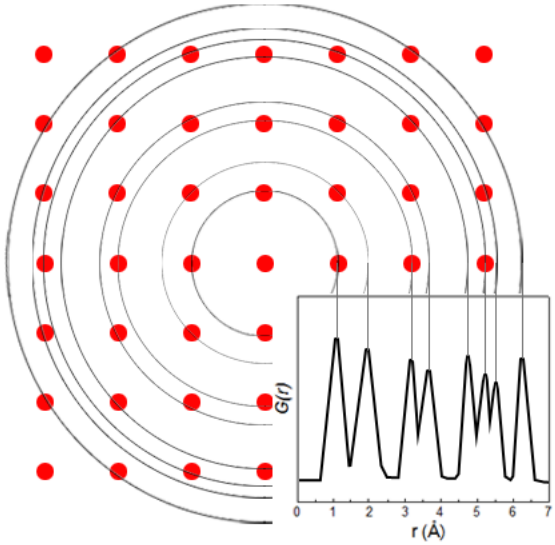

Figure 3.8 PDF peaks at distance separating pairs of atoms, proportional to the number of atoms at lattice sites. Redrawn from reference [103].

3.2.6 Mechanical Properties

Hardness

Hardness tests were carried out using a micro Vickers hardness tester (Shimadzu HVM-2000) with applied load of 200 g for 10 s of holding time. The hardness was examined with at least 15 indents with a distance of at least 5 times diagonal length of hardness indentation marks between each indent. The hardness was performed on ground and polished cross sections of as-homogenized rods and longitudinal sections of as-deformed samples.

Tensile and compression test

Tensile and compression tests were performed by using Instron 5869. A constant strain rate of 5×10^{-4} s^{-1} was applied to all tensile and compression test samples. The strain was measured by a laser extensometer (Fiedler Optoelektronik). The test of each sample was conducted with at least 3 test specimens for better statistic.

The tensile test specimens were prepared by wire cutting into a flat "dog-bone" shape, as illustrated in Figure 3.9. Prior to the test, the specimens were polished in order to remove processing defects on the surface.

The compression test pieces were prepared in a form of cylindrical rod with a dimension of a height to diameter ratio of 2:1. The test specimens should have a coplanar surfaces for a good quality of data.

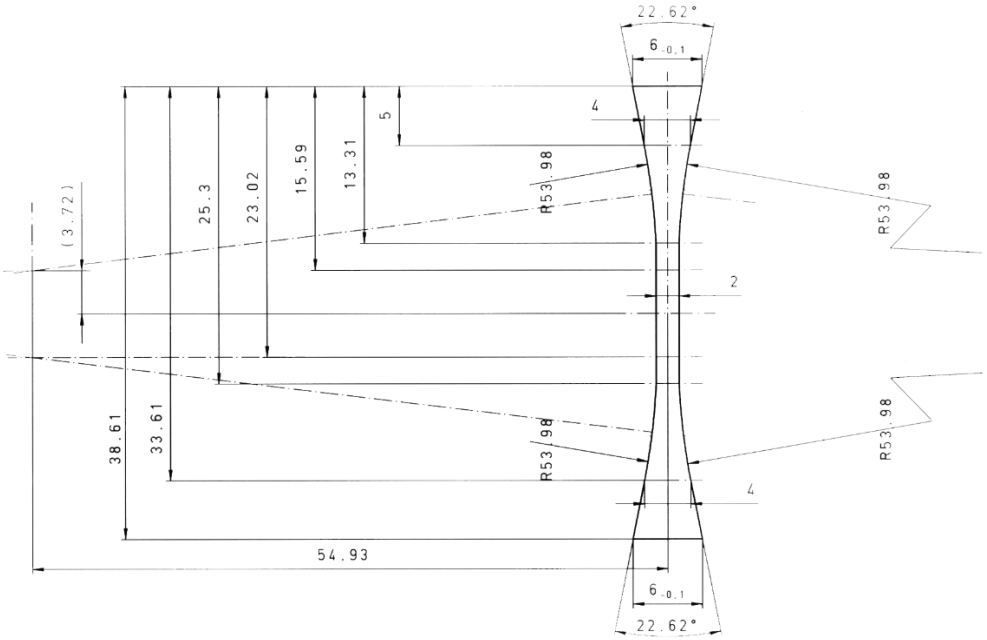

Figure 3.9 Schematic of a tensile test specimen.

4. Thermal phase stability of single phase high entropy alloys

The effect of solid solution phase in the equiatomic FeNiCoCrMn and TiNbHfTaZr HEAs and their equiatomic sub-alloys was studied on their microstructure and mechanical properties. Due to the non-equilibrium solidification during cold crucible casting, the dendritic microstructure and chemical microsegregation were observed in as-cast microstructures. The as-cast microstructures could not be investigated to represent the effect of the interactions between constituent elements due to chemical inhomogeneity at non-equilibrium state. In order to improve chemical homogeneities, the as-cast rod were subjected to the homogenization treatment. Figure 4.1 and 4.2 show EDX mappings of the homogenized *fcc*- and *bcc*-structured alloys, respectively, which indicate the chemical homogeneity of the alloys after homogenization (1273 K, 12 hours for the *fcc*-structured alloys and 1373 K, 24 hours for the *bcc*-structured alloys). The homogenized samples were used as starting samples in order to investigate the effect of the solid solution phase.

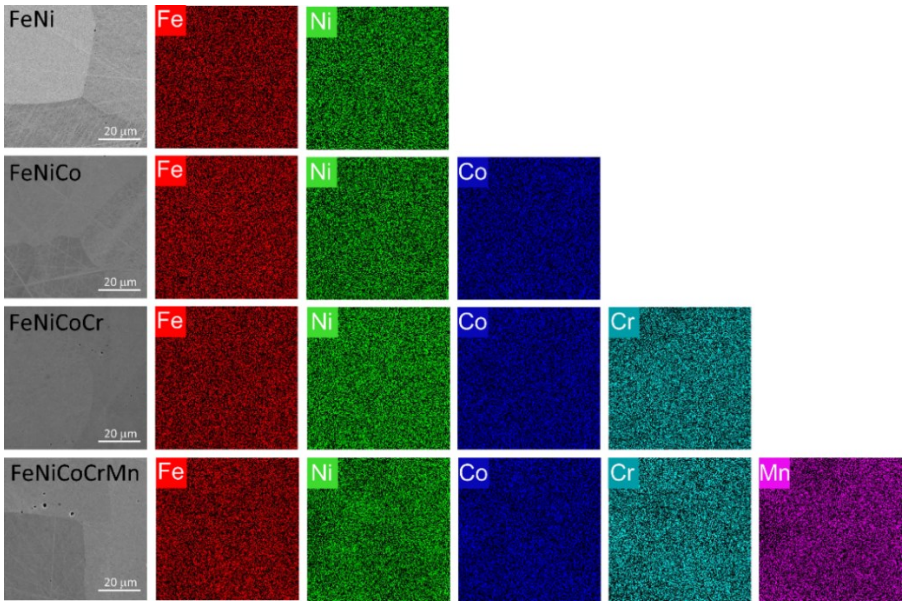

Figure 4.1 EDX element maps of As-homogenized microstructures for FeNi, FeNiCo, FeNiCoCr and FeNiCoCrMn.

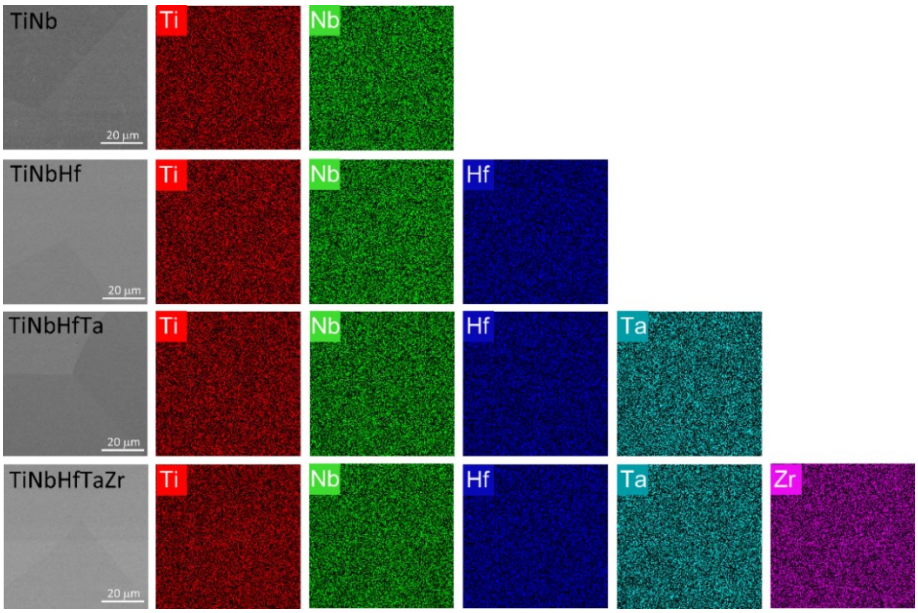

Figure 4.2 EDX element maps of As-homogenized microstructures for TiNb, TiNbHf, TiNbHfTa and TiNbHfTaZr.

The chemical homogeneities and compositions were firstly investigated by EDX at both two sides (top and bottom sides) of the as-homogenized rods. The two sides of each homogenized rod obtain similar chemical composition and the average chemical compositions for each alloy are presented in Table 4.1. For more precise measurement, the chemical compositions of the as-homogenized rods were measured by the ICP-OES method. The results showed similar chemical composition investigated by the EDX, as presented in Table 4.1. The all samples with exception of the TiNb alloy presented the equiatomic compositions. It was mentioned that the chemical composition of the TiNb alloy was shifted from the nominal composition. This might result from incomplete melting of the TiNb ingot during the casting. The large portion of the TiNb was remained at a conical-shaped part of the cast TiNb rod, which was possibly evident to the incomplete melting. However, the similar chemical compositions between the two sides of the TiNb rod (investigated by EDX) indicated the chemical homogeneity throughout the TiNb rod.

In this thesis work, the samples were subjected to the maximum temperature of 1223 K for sample preparations. Hence, the thermal phase stability of the samples were investigated between 300 - 1500 K.

Table 4.1 Chemical composition (in at%) of the studied *fcc*- and *bcc*-structured samples after homogenization examined by ICP-OES and EDX techniques.

fcc samples	ICP-OES					EDX				
	Fe	Ni	Co	Cr	Mn	Fe	Ni	Co	Cr	Mn
FeNi	50.15	49.85	-	-	-	51.16	48.84	-	-	-
FeNiCo	33.30	33.19	33.51	-	-	32.46	32.53	35.01	-	-
FeNiCoCr	25.02	25.14	25.13	24.70	-	24.56	24.81	26.38	24.26	-
FeNiCoCrMn	20.23	20.17	20.34	19.82	19.45	20.55	19.82	21.16	19.23	19.24
bcc samples	Ti	Nb	Hf	Ta	Zr	Ti	Nb	Hf	Ta	Zr
TiNb	61.53	38.47	-	-	-	63.44	36.56	-	-	-
TiNbHf	34.81	32.41	32.09	-	-	36.16	33.85	29.99	-	-
TiNbHfTa	25.04	25.31	25.00	24.66	-	25.87	23.92	24.87	25.34	-
TiNbHfTaZr	19.18	20.16	18.92	21.80	19.47	21.56	18.42	21.50	17.80	20.72

Phase stability of the fcc-structured FeNiCoCrMn high entropy alloy

Figure 4.3 presents the X-ray diffraction patterns of the equiatomic FeNiCoCrMn HEA and its sub-alloys (FeNi, FeNiCo and FeNiCoCr) after homogenization at 1273 K for 12 hours. The XRD patterns of as-homogenized HEA and its sub-alloys are in a good agreement with *fcc*-structured phase of Ni powder (Alfa Aesar; 325 mesh, 99.8% pure). The patterns of these samples are identified as a single *fcc*-structured phase without secondary phases. The peak positions are varied with an increase in the number of constituents, indicating different lattice parameters of the samples. The lattice parameters were calculated as 3.5242, 3.5791, 3.5738, 3.5682 and 3.5828 Å for Ni, FeNi, FeNiCo, FeNiCoCr and FeNiCoCrMn, respectively. It is observed that an increase in the number of constituents expanded the lattice parameter. The peak position difference between the HEA and Ni samples is the largest, which indicates the largest chemical complexity in the HEA. However, the lattice parameters slightly change between the HEA and its sub-alloys. Lattice

strain affected by the number of constituents is further investigated by pair distribution function (PDF) as will be presented in the chapter 5.

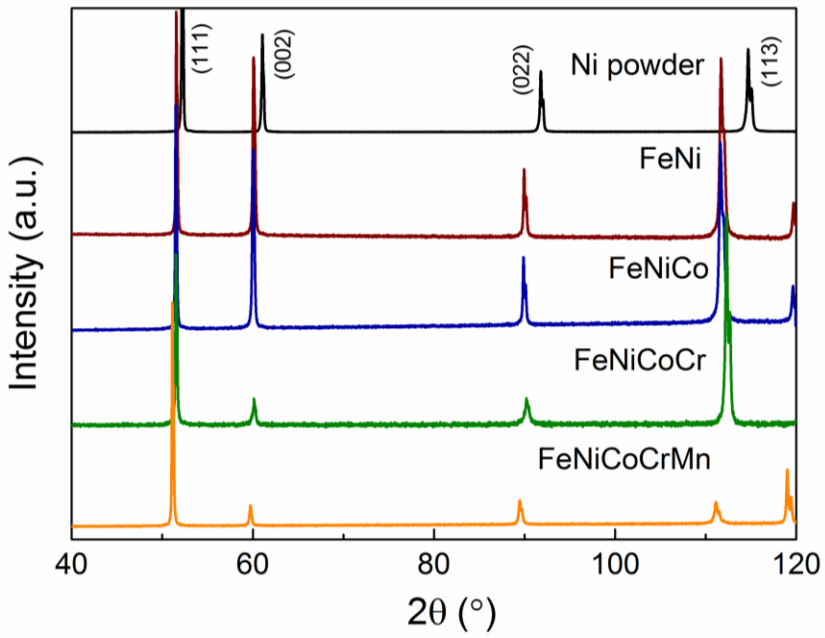

Figure 4.3 X-ray diffraction patterns of as-homogenized FeNiCoCrMn HEA and its sub-alloys comparing with Ni powder.

To study phase stabilities of *fcc*-structured HEA and its sub-alloys during thermal exposure, a differential scanning calorimeter (DSC) was carried out to inspect as-homogenized samples at heating and cooling rate of 20 K/min. Figure 4.4 presents DSC profiles, which show no endothermic or exothermic peaks for all alloys. It indicates that no solid state phase transformation occured during heating and cooling between 300 and 1500 K. However, on the cooling curve of the as-homogenized FeNiCoCrMn HEA, there is a fluctuation possibly due to Mn vaporization. The Mn vaporization gave an evidence of brown color on the top of sample crucible. Another evidence for Mn vaporization is found in the research works on sintering of Mn-containing steel at elevated temperatures [105, 106]. With loss of Mn through the vaporization, it seemed to cause fluctuation on cooling until approximately 1300 K. A certain time was needed to reach a stable heat flux as mentioned at temperature below 1300 K. However, chemical composition of the as-

homogenized FeNiCoCrMn HEA is not largely shifted from the nominal composition, which the amount of Mn loss during the homogenization is not significant.

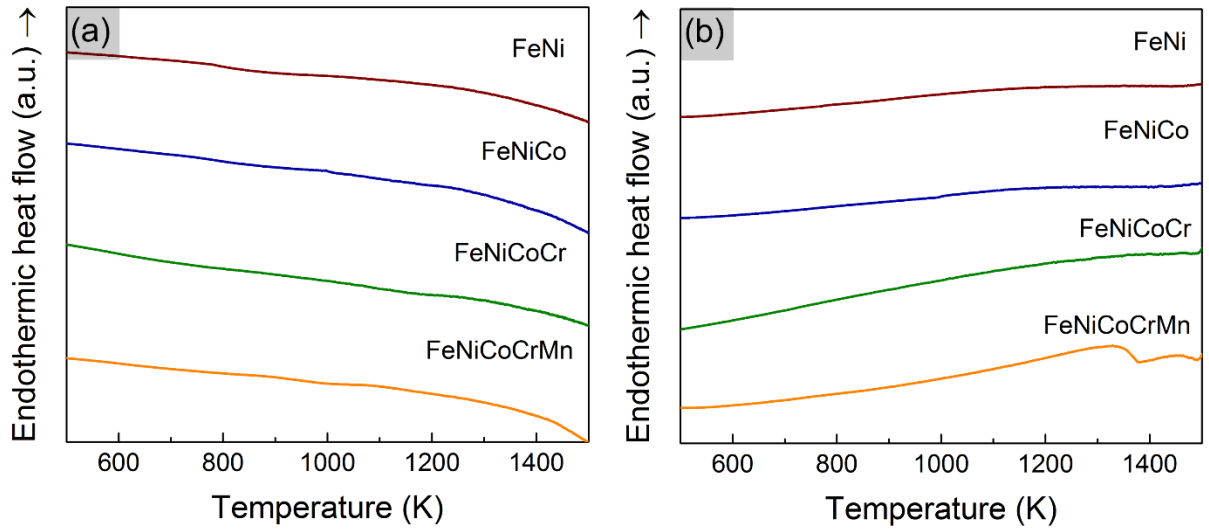

Figure 4.4 DSC thermograms; (a) heating and (b) cooling for as-homogenized FeNiCoCrMn HEA and its sub-alloys.

In thermodynamic aspects as discussed in the chapter 2, the enthalpy of mixing (ΔH_{mix}) is an important parameter to evaluate the phase formation in these multiple components HEAs. In case of ΔH_{mix} close to zero, the different elements can randomly distributed in the stable form of solid solution [30]. According to equation 2.2, the ΔH_{mix} were calculated as -4.16, -3.75, -1.33 and -2.00 kJ/mol for the FeNiCoCrMn HEA and its sub-alloys FeNiCoCr, FeNiCo and FeNi, respectively. It is clear that the solid solution phase in FeNi and FeNiCo can be stable due to relatively closer to zero ΔH_{mix} values. Despite the higher absolute values of ΔH_{mix}, the high configuration entropies (ΔS_{conf}) for the FeNiCoCrMn HEA (13.38 J/K·mol) and FeNiCoCr (11.52 J/K·mol) have more influence over the enthalpies of formation of intermetallic compounds (negative ΔH_{mix}) to stabilize solid solution phase [12, 30]. The Ω parameter [34], combining ΔH_{mix} and ΔS_{conf}, were calculated by the equation 2.5 with parameters ΔH_{mix}, ΔS_{conf} in Table 4.2 and T_m in Table 4.3. The parameters Ω for the studied *fcc*-structured alloys are between 4 – 12, as shown

in Table 4.2. Figure 4.5 shows the Ω and δ parameters for the studied *fcc*-structured alloys (marked as blue square) on the plot taken from reference [30]. All the studied alloys fall in the region of single solid solution formation ($\Omega \geq 1.1$ and $\delta \leq 6.6$).

Table 4.2 Configurational entropy (ΔS_{conf}) and enthalpy of mixing (ΔH_{mix}) for the studied *fcc*-structured and *bcc*-structured samples.

	Sample	ΔS_{conf} (J/K·mol)	ΔH_{mix} (kJ/mol)	Ω
fcc-structured sample	FeNi	5.76	-2.00	4.90
	FeNiCo	9.13	-1.33	11.76
	FeNiCoCr	11.53	-3.75	5.21
	FeNiCoCrMn	13.38	-4.16	5.02
bcc-structured sample	TiNb	5.76	2.00	6.75
	TiNbHf	9.13	2.67	8.20
	TiNbHfTa	11.53	2.50	12.09
	TiNbHfTaZr	13.38	2.72	12.42

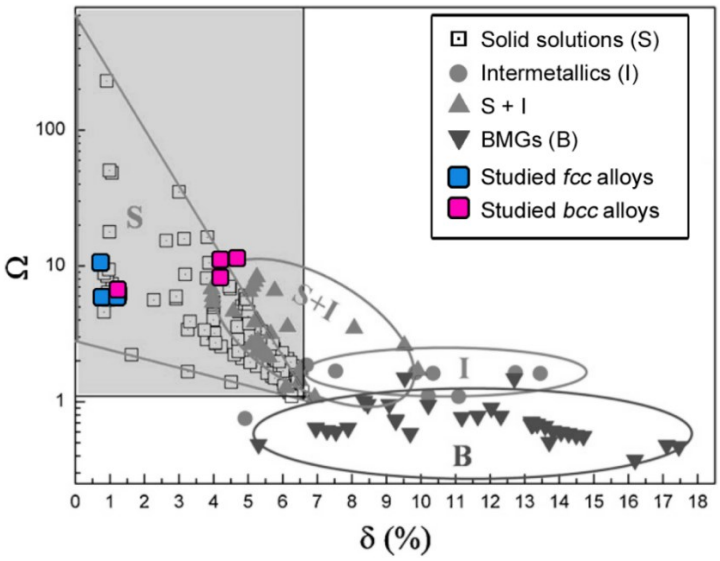

Figure 4.5 Relationship between the Ω and δ parameters determines the phase formation of the alloys studied in this chapter and alloys collected from literature. Adapted from reference [30].

Table 4.3 Atomic radius of the elements in the studied samples and atomic size misfit and the melting points the studied samples.

Element	*r* (pm)	Samples	δ (%)	T_m (K)
Ni	124[107]	Ni	0.00	1728[1]
Fe	126[107]	FeNi	0.80	1703[1]
Co	125[107]	FeNiCo	0.65	1713[1]
Cr	128[107]	FeNiCoCr	1.18	1693[1]
Mn	127[107]	FeNiCoCrMn	1.12	1562[1]
Nb	143[3]	Nb	0.00	2750[3]
Ti	146[3]	TiNb	1.12	2346*
Hf	158[3]	TiNbHf	4.28	2399*
Ta	143[3]	TiNbHfTa	4.13	2622*
Zr	160[3]	TiNbHfTaZr	4.98	2524[1]

*Calculated by using equation 2.5 with melting points of each element form the reference [108]

The X-ray diffraction patterns, DSC curves and calculated Ω value indicate a stability of single solid solution phase in the studied *fcc*-structured alloys. However, the possibility of second phase formation in these alloys cannot be completely eliminated. The formation of single solid solution phase can be facilitated applying high cooling rate during cold crucible casting and with homogenization temperature above the ordering temperature. The binary phase diagrams related to FeNi and FeNiCo alloys indicate a broad range of *fcc* solid solution formation at high temperatures near equiatomic composition, as presented in Figure 4.6. The ordered (B2) FeCo phase can be formed below 730 °C (1103 K) at equiatomic composition. Additionally, the ternary Fe-Ni-Co diagram shows complete solubility above 800 °C (1073 K) [109]. With Cr and Mn additions, it is observed that there are formations of several intermetallic compounds as can be seen in the binary diagrams of Co-Cr and Cr-Mn presented in Figure 4.7. It is reported that σ phase can be formed with Cr addition into this alloy system [36, 40]. M. C. Gao [36] presented the

theoretical calculation that the driving force for σ phase formation is strong in the binary Co-Cr system, but it decreases with increasing configurational entropy for the CoFe-Cr, CoFeMn-Cr, and CoFeMnNi-Cr system. According to the binary phase diagrams of Co-Cr, Cr-Mn system, it is possibly expected that Cr-rich σ phase can be precipitated a low temperature heat treatments for very long treatment time [40].

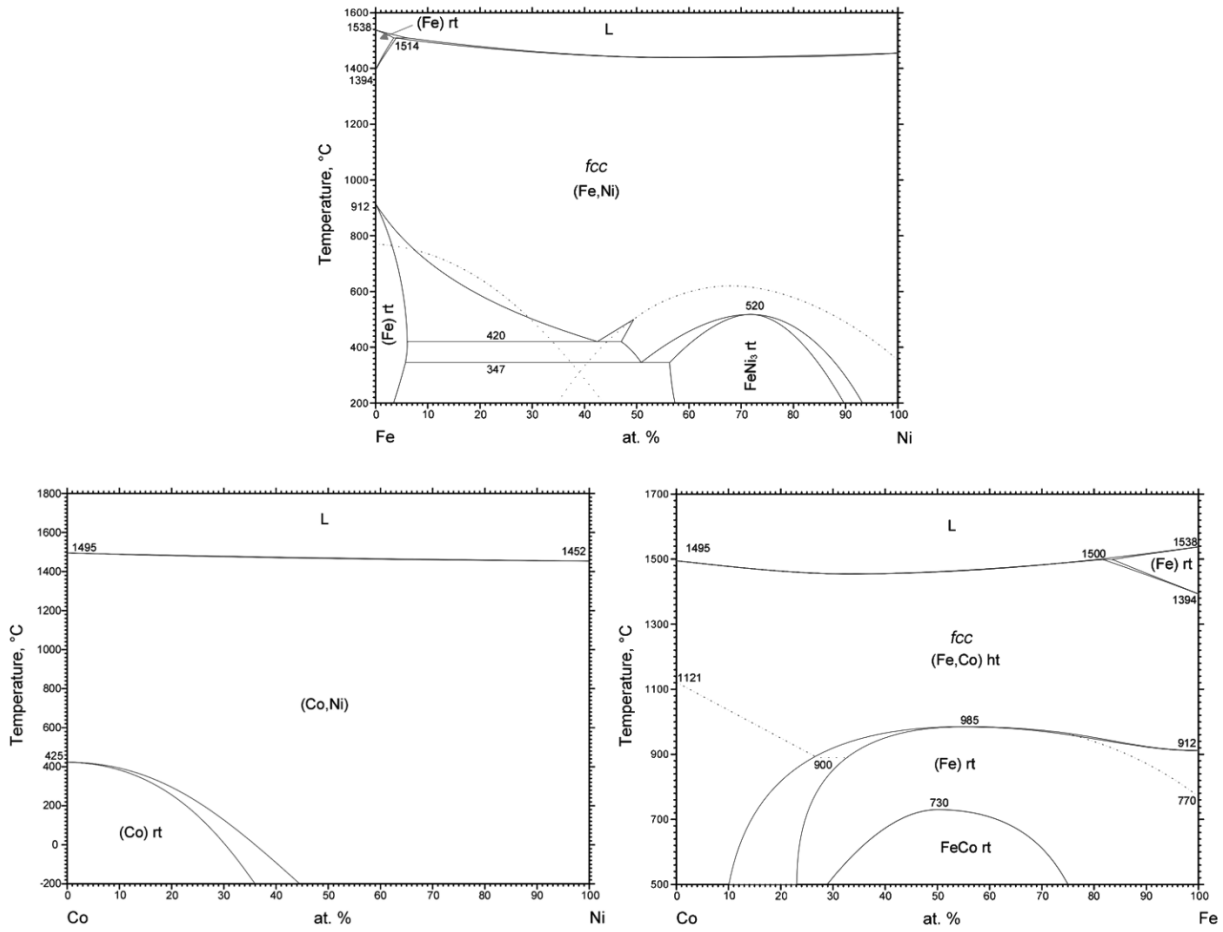

Figure 4.6 Binary phase diagrams of Fe-Ni, Co-Ni and Co-Fe systems [110].

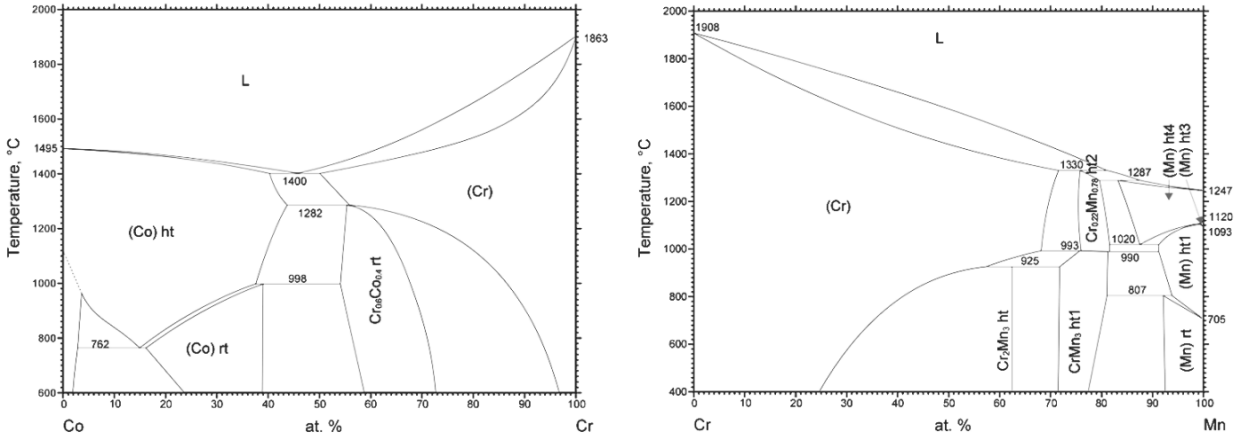

Figure 4.7 Binary phase diagrams of Co-Cr and Cr-Mn systems related to addition of Cr and Mn [110].

Recently, the instability of solid solution phase in FeNiCoCrMn HEA has been evidently reported. The FeNiCoCrMn HEA is often observed to show solid solution phase formation with tidy fraction of second phase particles. The Cr-rich phase is precipitated as fine particles after exposure between 873 - 1073 K [111, 112, 113]. N. D. Stepanov et al. [112] reports that the volume fraction of second phase particle reached the maximum about 2% at 973 K and decreased to about 0.3% at 1073 K. The second phase particles were not found after 1173 K annealing [112]. However, in this study, the microstructure of the FeNiCoCrMn HEA after annealing at 1223 K was not observed a presence of second phase. The presence of tiny fraction of the second phase is expected to have a minor effect on the microstructure and mechanical properties of FeNiCoCrMn HEA. The second phase formation are also observed in most of other HEAs [3, 12, 114]. E. J. Pickering et al. [12] suggests that the role of enthalpy is more influential than the configurational entropy. However, a number of investigations accepts that the configurational entropy (ΔS_{conf}) plays an important role in the stability of solid solution phase in HEAs and it affects greater than in conventional alloys.

Phase stability of the bcc-structured TiNbHfTaZr high entropy alloy

Figure 4.8 presents the XRD patterns of as-homogenized (1373 K, 40 hours) TiNbHfTaZr HEA and its selected sub-alloys; TiNbHfTa, TiNbHf and TiNb. The XRD patterns of the all samples are in a good agreement with the pattern of *bcc*-structured Nb powder (Alfa Aesar; 325 mesh, 99.8% pure). The XRD patterns indicate that the TiNbHfTaZr HEA and its selected sub-alloys obtain a single *bcc*-structured phase without secondary phases. The increase in the number of constituent elements results the peak shifts associated with the different lattice parameters. The lattice parameters were determined as 3.3030, 3.2986, 3.3973, 3.3597 and 3.4181 Å for Nb, TiNb, TiNbHf, TiNbHfTa and TiNbHfTaZr, respectively. The TiNbHfTaZr HEA demonstrated the largest lattice parameter because of its largest chemical complexity, similar with the largest lattice parameter of the FeNiCoCrMn HEA.

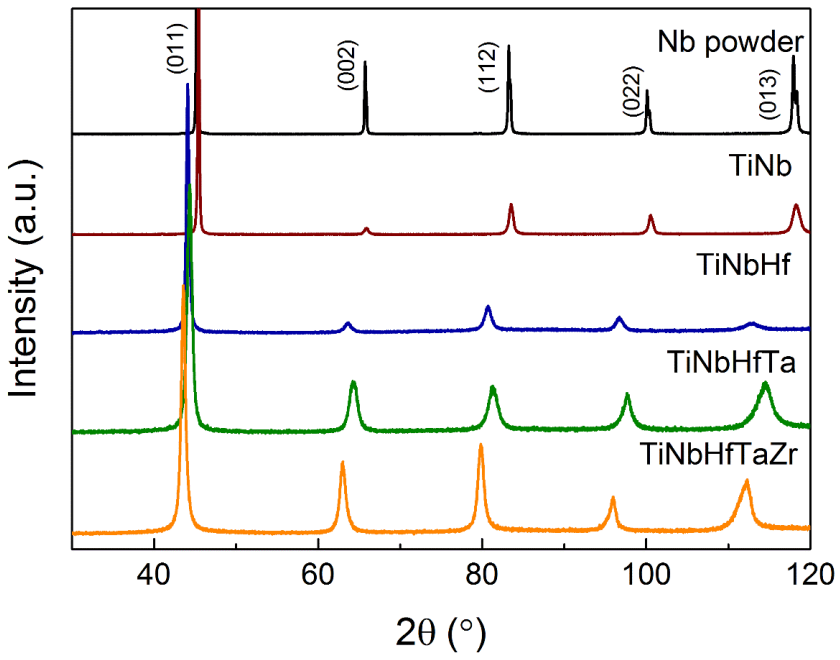

Figure 4.8 X-ray diffraction patterns of as-homogenized TiNbHfTaZr HEA and its sub-alloys comparing with Nb powder.

Figure 4.9 shows the DSC thermograms of the TiNbHfTaZr HEA and its sub-alloys. On both curves of heating and cooling at 20 K/min, no peak was observed, which imply no solid-state phase transformation during the temperature range (300 – 1500 K). However, a slight fluctuation on the cooling curve of the TiNb sample was observed at approximately 1200 K. The experimental error could be a reason because a phase diagram of Ti-Nb (Figure 4.10) shows a broad range of *bcc*-structured solid solution phase all the compositional range above approximately 600°C.

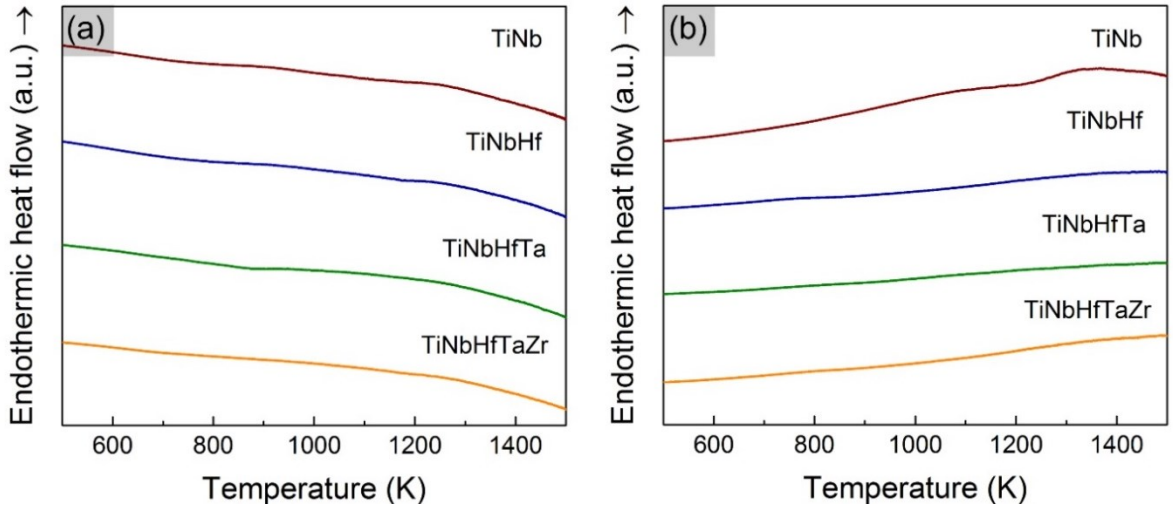

Figure 4.9 DSC thermograms; (a) heating and (b) cooling for as-homogenized TiNbHfTaZr HEA and its sub-alloys

Nb and Ta have only one stable *bcc* structure, while Ti, Zr and Hf have a *hcp* structure at lower temperatures and a *bcc* structure at high temperatures. The combination of these elements in the TiNbHfTaZr forms the *bcc*-structured solid solution phase. Despite a lack of equilibrium phase diagram of the TiNbHfTaZr alloy, the binary phase diagrams related to Ti-Nb-Hf-Ta-Zr alloy system also demonstrate the formation of *bcc*-structured solid solution phase over the broad range of temperature. Addition of Hf promotes the formation of *hcp* phase. For example, the Hf-Ti phase diagram (Figure 4.10), *bcc* solid solution phase is stable at high temperature before allotropic transformation at about 900°C (1173 K) for equiatomic composition. It is also observed that addition of Zr causes decomposition of the *bcc* solid solution phase into two *bcc* phases, as

presented in the Ta-Zr and Nb-Zr binary phase diagrams (Figure 4.10). However, according to the equation 2.2, the TiNbHfTaZr HEA obtains $\Delta H_{mix} \approx 2.72$ kJ/mol (close to zero values of ΔH_{mix}), which support the tendency to form single solid solution phase. The TiNbHfTa, TiNbHf and TiNb alloys also obtain close to zero values of ΔH_{mix}, calculated as 2.50, 2.67 and 2.00 kJ/mol, respectively. Furthermore, the calculated Ω parameter for the TiNbHfTaZr HEA and its sub-alloys is between 6 – 12, as shown in Table 4.2 and the atomic size misfits (δ) are between 1 – 5%, as presented in Table 4.3. The Ω and δ parameters for these alloys are plotted in the diagram of Figure 4.5 (marked as pink squares) and fit the criterion for solid solution formation ($\Omega \geq 1.1$ and $\delta \leq 6.6$). In experimental evidence, O. N. Senkov et al. [43] reported that no phase transformation was observed after 3 hours of hot isostatic pressing (HIP) of TiNbHfTaZr HEA. Additionally, the TiNbHfTaZr HEA was examined to obtain a very small fraction of fine second phase precipitation after annealing above 1273 K [90]. Many experimental reports present that solid solution phase in the most HEAs is not stable at all temperature of process treatments [9].

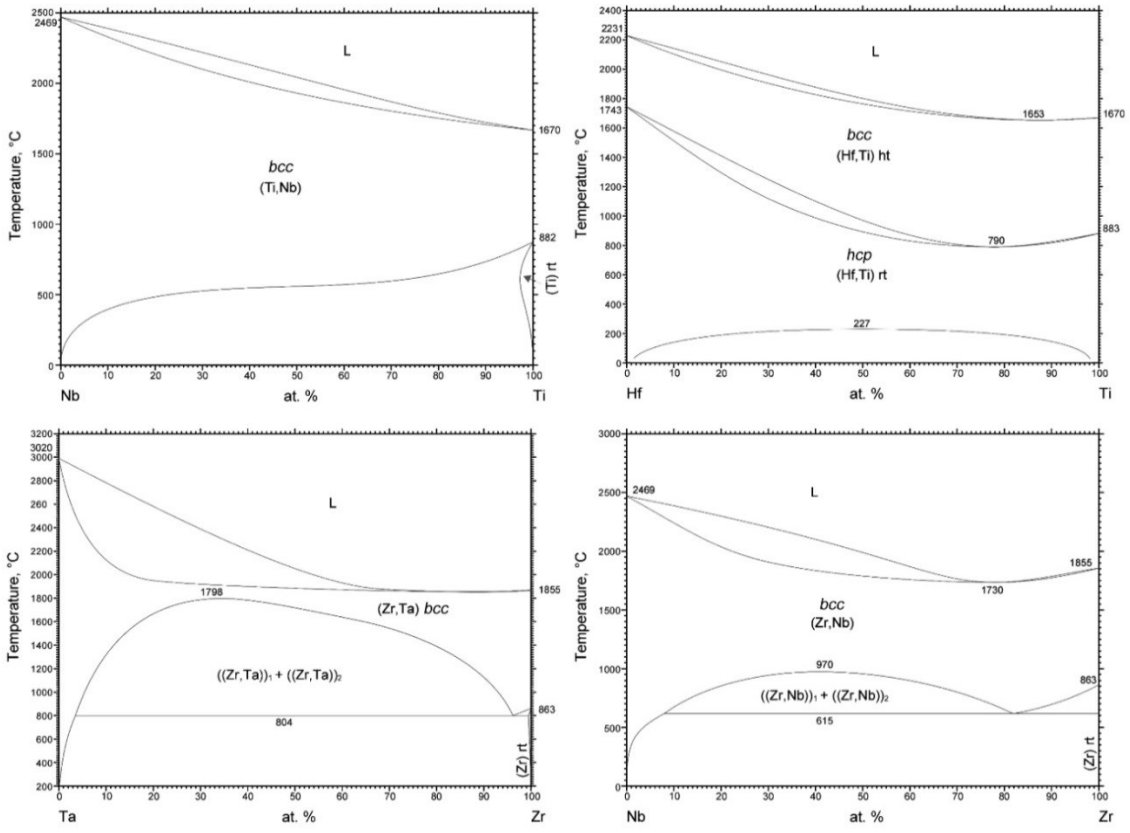

Figure 4.10 Binary phase diagrams of Nb-Ti, Hf-Ti, Ta-Zr and Nb-Zr systems [110].

Despite the hypothesis that the configurational entropy may favor the formation of single solid solution phase, the values of the configurational entropy in HEAs is normally high due to a large number of constituent elements. In this study, the all studied alloys present single solid solution phase, which obtain close to zero values of the mixing enthalpy and different values of the configurational entropy. It can imply that the mixing enthalpy is an important parameter for the formation of solid solution phase. It is in a good agreement with literatures that the mixing enthalpy and atomic size misfit are intensively used for a determination of solid solution formation [12, 115, 116].

5. An assessment of lattice strain in single phase high entropy alloys

The random atomic arrangement in solid solution phase of high entropy alloys (HEAs) is more complex than in conventional dilute alloys because of high concentration of multiple atom species in HEAs. The presence of multiple atom species at lattice sites are expected to give rise to a high level of lattice strain, which influences the HEAs behaviors. Thus, this chapter focuses on the quantitative analysis of the lattice strain of HEAs. The assessments of lattice strain in the both micro and local scales of lattice strain are determined by using the synchrotron X-ray diffraction.

As described in chapter 3, the samples in a study of lattice strain were prepared by thermomechanical treatments consisting of rolling and subsequent annealing. The samples obtained homogeneous fine microstructures with small strain-free grains. The high statistics of the synchrotron X-ray diffraction data can be collected from the large number of refined grains in the samples. In order to determine intrinsic lattice strain, the residual strain of the samples was removed by annealing. The measured chemical composition and oxygen content in the samples after thermomechanical treatment were measured and are shown in Table 5.1. The alloys containing Ti showed higher oxygen amount when compared with the other samples, but the content were quite low, below ≈ 1 at%. The limited content of oxygen probably gives a minor effect on lattice strain and the investigation of lattice strain can be focused on the effect of the alloy composition as discussed in the following.

Table 5.1 Chemical composition of the studied *fcc*- and *bcc*-structured samples after thermomechanical treatment examined by ICP-OES and CGHE.

fcc samples	Chemical Composition (at%)					
	Fe	Ni	Co	Cr	Mn	O
Ni	-	100	-	-	-	0
FeNi	50.04	49.96	-	-	-	0.03
FeNiCo	33.38	33.21	33.41	-	-	0.03
FeNiCoCr	25.18	24.92	25.12	24.72	-	0.07
FeNiCoCrMn	20.17	20.11	20.23	19.88	19.54	0.08
bcc samples	Chemical Composition (at%)					
	Ti	Nb	Hf	Ta	Zr	O
Nb	-	99.97	-	-	-	0.03
TiNb	58.09	40.82	-	-	-	1.09
TiNbHf	34.78	32.27	31.84	-	-	1.10
TiNbHfTa	24.90	25.10	24.81	24.48	-	0.71
TiNbHfTaZr	20.09	20.30	19.93	18.60	20.46	0.61

5.1 Analysis of micro lattice strain on *fcc*- and *bcc*-structured high entropy alloys

In this section, the analysis of micro lattice strain was demonstrated with the Williamson-Hall method applied on high energy synchrotron X-ray diffractions with Q_{max} = 12 Å^{-1}. Bragg intensities give a spatially averaged picture of the structure [8]. The Bragg peak broadening is particularly due to grain size, micro strain effects as well as instrumental effect [97, 99]. In this study, the instrumental broadening can be estimated by calibration measurement with a LaB_6 standard sample. The external stress and textural effect were minimized by annealing the samples

in order to assess the lattice strain associated with crystal imperfections and intrinsic lattice distortion [97, 117].

Micro lattice strain of the fcc-structured FeNiCoCrMn high entropy alloy

Figure 5.1 presents the high energy synchrotron X-ray diffraction patterns of as-annealed *fcc*-structured samples. The patterns of the FeNiCoCrMn HEA and its sub-alloys (FeNi, FeNiCo and FeNiCoCr alloys) fit well with the dataset of Ni solid solution. It suggests that the HEA and its sub-alloys obtain single *fcc*-structured solid solution phase with variation in lattice parameter. It is observed that the peak positions are shifted toward lower 2 theta values with an increase in the number of constituent elements. The lattice parameters of all the samples are presented in Table 5.2. The result suggests that the FeNiCoCrMn HEA presented the largest lattice parameter possibly due to the highest chemical complexity.

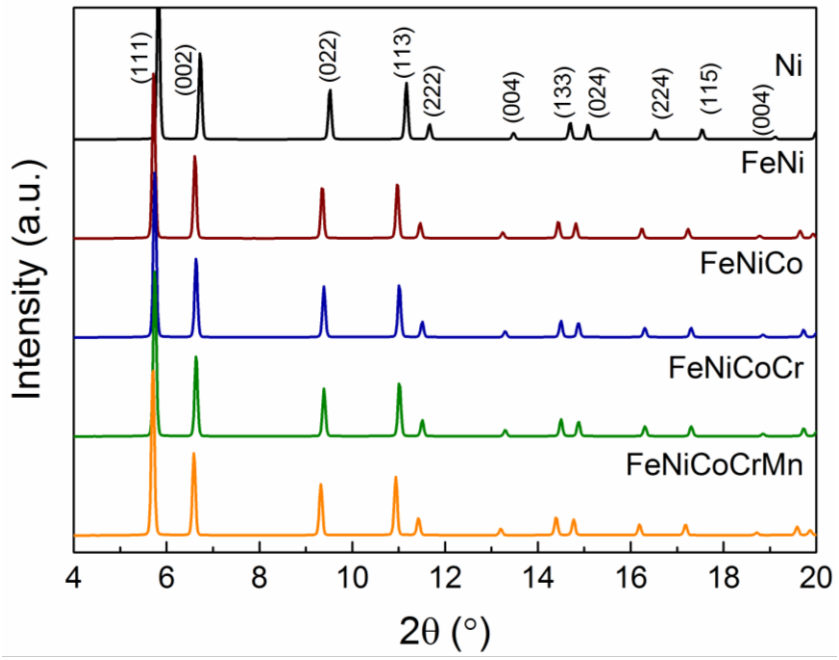

Figure 5.1 High energy synchrotron X-ray diffraction patterns of as-annealed *fcc*-structured samples.

Table 5.2 Lattice parameters and micro lattice strain of as-annealed *fcc*- and *bcc*-structured samples determined from high energy synchrotron X-ray diffraction data.

fcc samples	*a* (Å)	ε_{str} (%)	*bcc* samples	*a* (Å)	ε_{str} (%)
Ni	3.5207	0.0337	Nb*	3.2971	0.2263
FeNi	3.5828	0.0350	TiNb	3.2960	0.0282
FeNiCo	3.5690	0.0342	TiNbHf	3.3740	0.0280
FeNiCoCr	3.5691	0.0388	TiNbHfTa	3.3539	0.0429
FeNiCoCrMn	3.5942	0.0389	TiNbHfTaZr	3.4011	0.0466

*As-received Nb rod

Figure 5.2 (a) presents the Williamson-Hall plots of the FeNiCoCrMn HEA and its sub-alloys as well as pure Ni sample. The details of Williamson-Hall method were described in section 3.3.5 of chapter 3. The marks represent the integral breadths and 2θ values of the (111), (002), (022), (113), (222), (004), (133), (024), (224), (115) and (044) reflections. By fitting the data, the micro lattice strain was derived from the slope of the linear fit and presented in Figure 5.2 (b). The result shows that the values of micro lattice strain were between 0.0337 and 0.0389%. The pure Ni sample obtained the lowest value of micro lattice strain with 0.0337%, similar to those of the FeNi and FeNiCo alloys. With the addition of Cr which has the largest atom, the FeNiCoCr and FeNiCoCrMn alloys presented larger magnitudes of the micro strain; 0.0388 and 0.0389%, respectively. The atomic radius of the elements (Fe, Ni, Co, Cr and Mn) are not significantly different and their atomic radius are between 124 -128 Å. This may suggests that the values of micro lattice strain were not significantly different among all the samples. Although the largest number of constituent elements in the FeNiCoCrMn HEA leads to the complex arrangement of atoms at the lattice sites, the micro lattice strain in the FeNiCoCrMn HEA is not anomalously large.

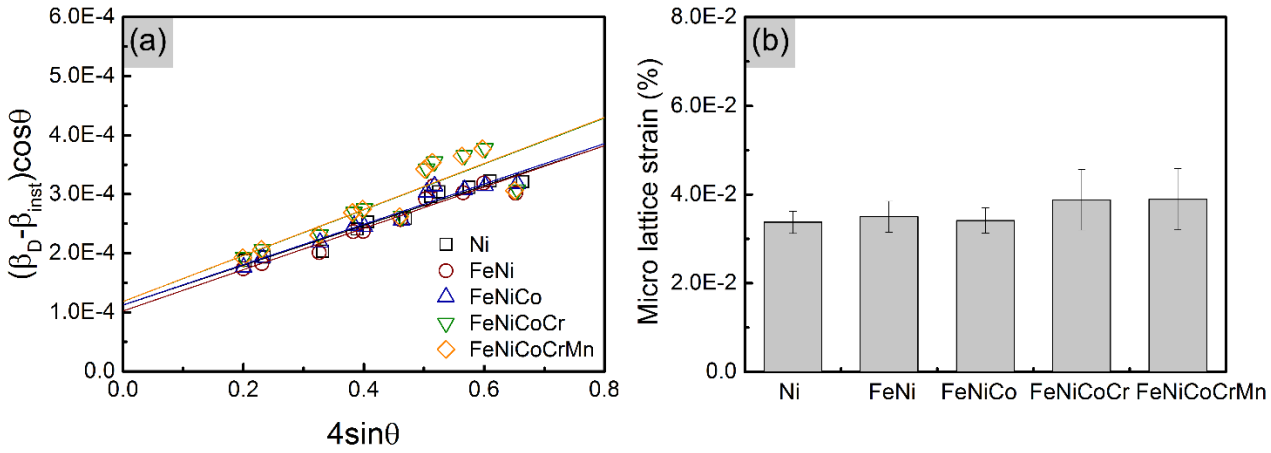

Figure 5.2 (a) Williamson-Hall plots and (b) micro lattice strain of as-annealed *fcc*-structured samples.

Micro lattice strain of the bcc-structured TiNbHfTaZr high entropy alloy

Figure 5.3 shows the high energy synchrotron X-ray diffraction patterns of the *bcc*-structured samples; they are similar for all samples. The patterns of the TiNbHfTaZr HEA and its sub-alloys agree with the Nb pattern. It indicates the presence of single *bcc*-structured solid solution phase in all alloys. An increase in the number of constituent element in this alloy family leads to peak shift toward lower 2 theta values, similar to the result of the *fcc*-structured samples. The lattice parameters of Nb, TiNb, TiNbHf, TiNbHfTa and TiNbHfTaZr were determined as 3.2971, 3.2960, 3.3740, 3.3539 and 3.4011 Å, respectively, as shown in Table 5.2. An increase in the number of the constituent elements increased the lattice parameters of the samples. It is observed that the increase in the lattice parameter with the effect of element number was significant in the *bcc*-structured samples rather than in the *fcc*-structured samples. Besides the number of constituent elements, the characteristic of the elements has more effect on the lattice parameter.

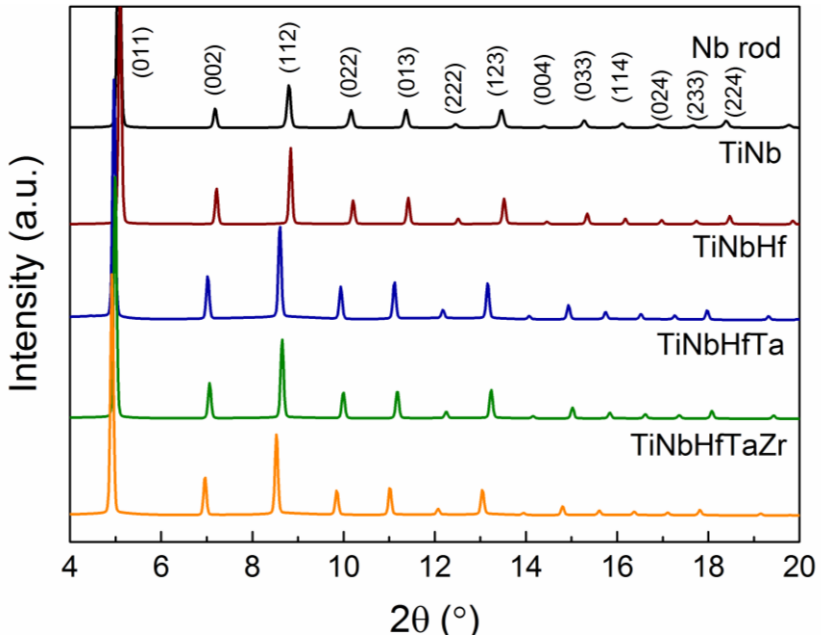

Figure 5.3 High energy synchrotron X-ray diffraction patterns of as-annealed *bcc*-structured samples.

Figure 5.4 presents the Williamson-Hall plots of the TiNbHfTaZr HEA and its sub-alloys including the Nb sample. The marks represent the integral breadths and 2θ positions of (011), (002), (112), (022), (013), (222), (123), (033), (114), (024), (223) and (224) reflections. It is observed that the slope for the Nb sample is significantly large when compared to those for the other samples. Due to Bragg peak broadening including the effect of all crystal defects, it suggests that the Nb sample possibly obtained a large amount of residual strain from production process. It also indicates that the Nb sample was not properly annealed to obtain a completely refined microstructure. Therefore, the Nb sample (obtaining 0.2263% micro lattice strain) was excluded from this investigation of intrinsic micro lattice strain associated with the constituent elements. Figure 5.5 (a) presents the Williamson-Hall plots and Figure 5.5 (b) shows a comparison of micro lattice strain between the TiNbHfTaZr HEA and its sub-alloys (excluding the Nb sample). The dislocation densities of the TiNb, TiNbHf, TiNbHfTa and TiNbHfTaZr samples were determined as 0.0282, 0.0280, 0.0429, 0.0466%, respectively. It indicates that an increase in the number of constituent elements increased the level of the dislocation density. The TiNbHfTaZr HEA obtained the highest level of micro strain probably due to the largest level of chemical complexity. In a comparison with the dislocation density of the FeNiCoCrMn HEA (0.0389%), that of the

TiNbHfTaZr HEA was higher. It might also be a result of a large difference between the atomic radius of Ti, Nb, Hf, Ta and Zr. The atomic radius of the elements in the range of 143 – 160 Å. It is also observed that the addition of Ta in the TiNbHfTa samples increased the dislocation density, which was higher than that of the TiNbHf sample. It should be noted that the remarkable transition of the micro strain level was also found in between the ternary and quaternary alloys of the Fe-Ni-Co-Cr-Mn system. The large increase in micro lattice strain might be caused by an increase in chemical complexity.

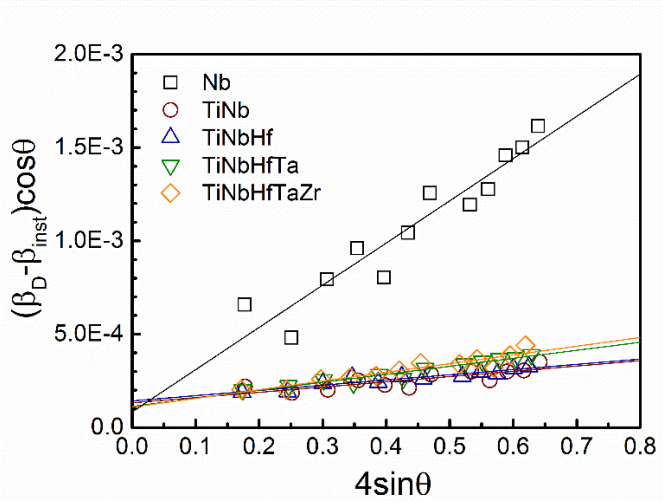

Figure 5.4 Williamson-Hall plots of as-annealed *bcc*-structured samples including Nb sample.

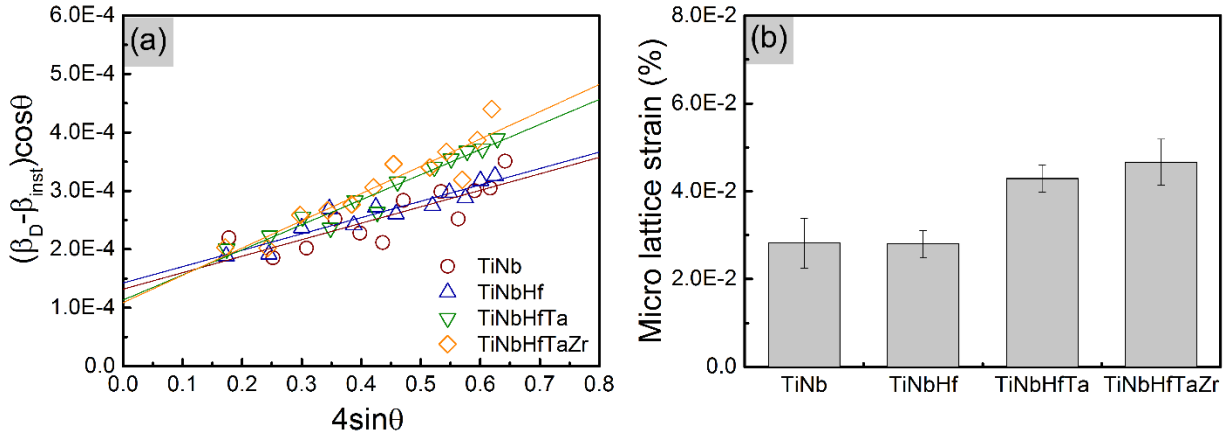

Figure 5.5 (a) Williamson-Hall plots and (b) micro lattice strain of as-annealed *bcc*-structured samples excluding Nb sample.

It is reported that the displacement of lattice points from their ideal position may cause both shift and broadening of the diffraction peaks [98]. The random presence of multiple atom species at lattice sites in HEAs was expected to cause the high level of strain-induced peak broadenings and peak shifts, which was in a good agreement with the results in both the FeNiCoCrMn and TiNbHfTaZr HEAs. However, the levels of micro lattice strain were not significantly different among the HEAs and their sub-alloys. T. Egami et al. [102] suggests that crystallographic information on Bragg intensity demonstrates only the average bond distance and the lattice parameter. Additionally, the experimental result also showed the effect of residual strain on the level of micro lattice strain. It suggests that the investigation on Bragg intensities is not sufficient to proof the hypothesis of severe lattice distortion in HEAs. Hence, the pair distribution function (PDF) will be used to analyze the effect of constituent elements on intrinsic lattice strain.

5.2 Analysis of local lattice strain on *fcc*- and *bcc*-structured high entropy alloys

The local lattice strain was assessed by a pair distribution function (PDF) transformed from the total scattering data with a wide range of Q value (Q_{max} = 26 $Å^{-1}$). The PDF profile includes both the Bragg and diffuse components on total scattering patterns [8], as described in the section 3.3.5. The diffuse scattering intensities allow assessing a local variation in the structure deviating from average structural information reflected in the Bragg intensities [9]. Hence, residual strain from production process has a minor effect on the determination of local lattice strain with PDF method. The Nb sample, which did not obtain completely refined microstructure, can be studied the intrinsic local lattice strain by PDF method.

Local lattice strain of the fcc-structured FeNiCoCrMn high entropy alloy

Figure 5.6 presents the reduced pair distribution functions, *G(r)* of the *fcc*-structured samples. The PDF profiles of the HEA and its sub-alloys are similar to the profile of *fcc* Ni, which

indicate *fcc*-structured phase. The positions of peaks of PDF profiles are related to the distribution of the interatomic distances directly in the real-space, *r* [9, 10]. There are slight peak shifts among the studied alloys because of a variation of the lattice parameters. The distance at second coordination shell (or second PDF peak) in *fcc*-structured materials is equivalent to a length of the unit cell. They were measured as 3.5339, 3.5823, 3.5662, 3.5711 and 3.5892 Å for Ni, FeNi, FeNiCo, FeNiCoCr and FeNiCoCrMn, respectively. These values were very similar to the lattice parameters measured by the position of the Bragg peaks.

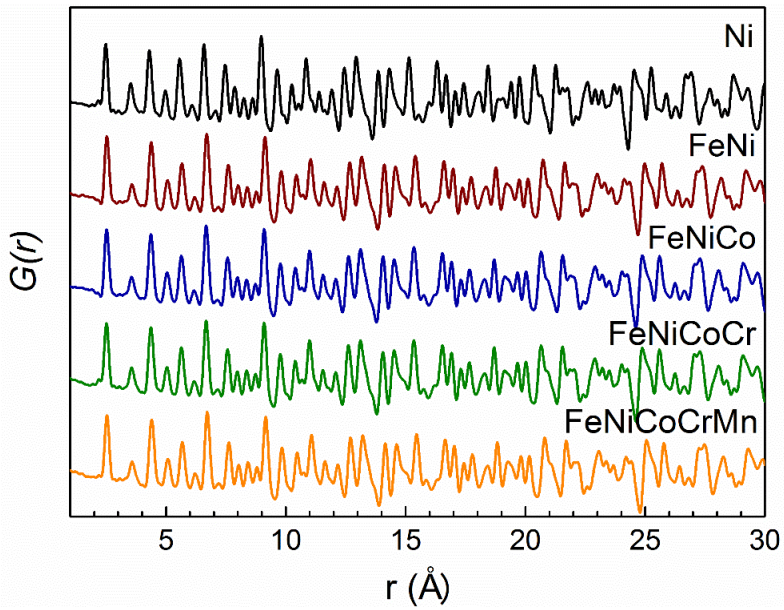

Fig. 5.6 Normalized pair distributions functions for all of the *fcc*-structured studied alloys.

The width of the peaks depends on the coordination number and the distribution of distances for the given atomic pair [10, 104, 118, 119]. The local lattice distortion associated with the displacement of multiple atoms from their ideal positions is expected to cause significant local lattice strain-induced PDF peak broadening in HEAs. The expanded PDF spectrums and full width at half maximum (FWHM) determined by Gaussian fitting for the first six coordination shells are shown in Figure 5.7 (a) and (b), respectively. In an ideal case, the width of the peak is the function of dynamic and static atomic displacements [10, 119]. The dynamic displacement is due to thermal

vibrations, which are expressed by the neighboring atomic positions and the melting point [120]. The amplitude of thermal vibration is inversely proportional to their homologous temperature (T/T_m) [104]. The homologous temperatures for the studied samples were similar; between 0.17 - 019. Due to the measurement at room temperature (T = 298 K) for all samples, the thermal vibration is dependent on the melting point of the samples. As shown in Table 4.3, the melting points of the Ni, FeNi, FeNiCo and FeNiCoCr samples are in a narrow range between 1693 – 1728 K, but the melting point of the FeNiCoCrMn HEA (1562 K) is lower. The lower melting point of the HEA might lead to the larger dynamic displacement, but the level of the peak broadening were insignificant. Hence, it could be assumed that the magnitude of the dynamic displacement in the studied alloys was constant.

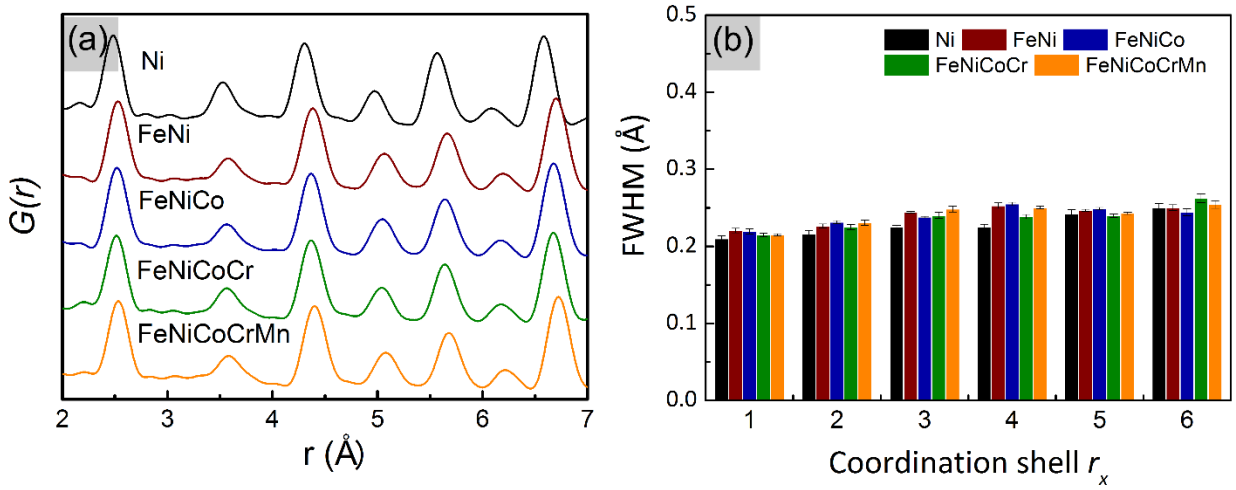

Figure 5.7 (a) Expanded pair distribution functions and (b) full width at half maximum (FWHM) values measured by Gaussian fits for the six coordination shells of as-annealed *fcc*-structured samples.

The static displacement of the PDF peak broadening is a measure of local lattice distortion caused by atomic size misfit between substitutional atoms in the solid solutions [121]. The PDF peak at the first coordination shell is normally sharper than those at higher coordination number. It is caused by the motion between different pairs of near-neighbor atoms, while far-neighbor atoms move more independently [119]. The static displacement for pure Ni can be assumed to be zero in an ideal case due to single species of all atoms perfectly located on the *fcc* lattice points

[122]. As the result, the FWHM of Ni sample at the first coordination shell was assumed to be equivalent to the value of dynamic displacement (~ 0.2100 Å). The FWHMs at the first coordination shell of the FeNiCoCrMn HEA, FeNiCoCr, FeNiCo and FeNi were 0.2205, 0.2193, 0.2148 and 0.2148 Å, respectively. After subtraction of the equivalent dynamic displacement, the equivalent values of static displacement were between 0.0048 – 0.0105 Å. These values were not significant large and the values for the HEA was just 0.0048 Å. The FWHM values for the first six coordination shells presented in a narrow variation for all the samples. It suggested that the local lattice distortion in the FeNiCoCrMn HEA is not significantly larger than its sub-alloys and Ni sample.

The level of the lattice strain or the lattice distortion was considered to be related to the magnitude of the atomic size misfit. The atomic size misfit is calculated with the equation 2.4. The calculated magnitude of atomic size misfit (δ) are 0.80, 0.65, 1.18 and 1.12% for FeNi, FeNiCo, FeNiCoCr and FeNiCoCrMn, respectively. These values are not relatively high because of a small variation of the atomic size as presented in Table 4.3. The similar atomic radius of Ni, Fe and Co result in similar values of δ in FeNi and FeNiCo. With the addition of Cr (having the largest atomic size), the atomic size misfit increases to 1.18% in FeNiCoCr. As a result of small magnitudes of the atomic misfit in the *fcc*-structured samples, the considerable differences were not seen in the level of local lattice strain. This experimental study showed no evidence that a severe lattice distortion was observed in the FeNiCoCrMn HEA.

Local lattice strain of the bcc-structured TiNbHfTaZr high entropy alloy

Figure 5.8 displays normalized pair distributions functions for all of the *bcc*-structured studied alloys. The PDF spectrums of TiNbHfTaZr HEA and its sub-alloys are likely that of Nb sample, which implies single *bcc*-structured solid solution in the samples. The PDF spectrum of Nb sample presents clearly individual peaks for each coordination shell; in contrast, the peaks of TiNbHfTaZr HEA for first and second coordination shells are overlapped. It indicates the peak broadening in the HEA. The distance at second coordination shell is equivalent to the lattice parameter of *bcc* lattice structure. The distances at second peak were measured as 3.3030, 3.2727,

3.2940, 3.2300 and 3.3088 Å for Nb, TiNb, TiNbHf, TiNbHfTa and TiNbHfTaZr, respectively. It led to a doubt about the remarkable differences with the lattice parameter of TiNbHf, TiNbHfTa and TiNbHfTaZr determined on Bragg data as shown in Table 5.2. The measurement of Bragg data determines only the long range order of the lattice and may not provide sufficient information to explain local atomic displacements away from the crystallographic sites [8, 102]. It might result in the errors of the lattice parameter examination on Bragg data.

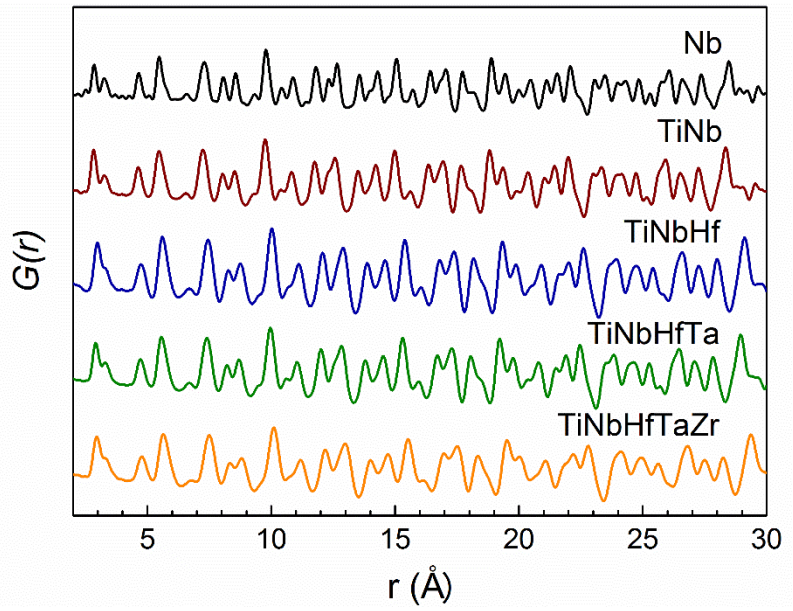

Figure 5.8 Normalized pair distributions functions for all of the *bcc*-structured studied alloys.

Figure 5.9 (a) presents the expanded PDF profiles and Figure 5.9 (b) shows the calculated FWHM for the first six coordination shells. It is apparent that the PDF peak widths show significant deviation among the *bcc*-structured samples and the width of the TiNbHfTaZr HEA is remarkably larger among the *bcc*-structured samples. As discussed above, the PDF peak width collects the information of static and dynamic disorder of atoms involved in the pair. The term of dynamic disorder is correlated to exposure temperature and melting point of samples. The melting points of the samples are largely different; 2750, 2346, 2399, 2622 and 2524 K for Nb, TiNb, TiNbHf, TiNbHfTa and TiNbHfTaZr, respectively, as shown in Table 4.3. The melting points of

the TiNb and TiNbHf are relatively lower than the others; thus, the dynamic displacement of these two samples was possibly larger. However, the homologous temperatures (T/T_m) for all the *bcc*-structured samples (between 0.11 - 0.13) were not much different due to their high melting points. The dynamic atomic displacements were assumed to be similar in all the *bcc*-structured samples. In an ideal case, the PDF peak width of the Nb sample should be resulted by only dynamic atomic displacement.

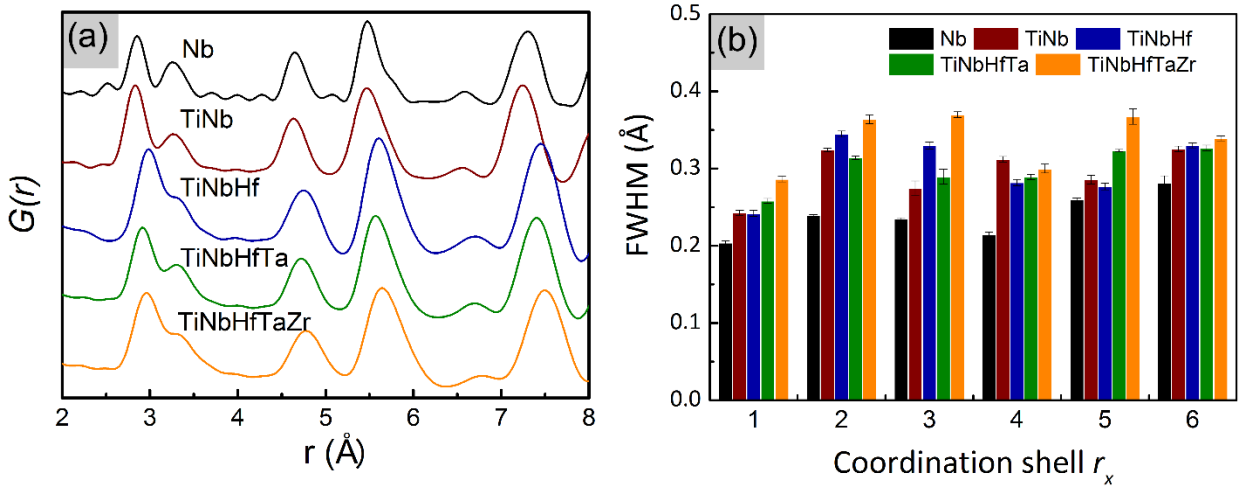

Figure 5.9 (a) Expanded pair distribution functions and (b) full width at half maximum (FWHM) values measured by Gaussian fits for the six coordination shells of as-annealed *bcc*-structured samples.

The static atomic displacement of TiNbHfTaZr HEA and its sub-alloys could be determined by subtraction of the width of Nb sample from their widths. Considering the PDF peak at the first coordination shell, the values of the FWHM were examined as 0.2038, 0.2429, 0.2420, 0.2581 and 0.2862 Å for Nb, TiNb, TiNbHf, TiNbHfTa and TiNbHfTaZr samples, respectively. The equivalent magnitudes of the static displacement, determined on the first PDF peak, were 0.0391, 0.0382, 0.0543 and 0.0824 Å for TiNb, TiNbHf, TiNbHfTa and TiNbHfTaZr samples, respectively. The increase in the amplitude was possibly caused by local lattice strain associated with atomic misfit and the number of constituent elements. The significantly higher value of static

displacement of TiNbHfTaZr HEA suggested the large atomic displacements from their ideal lattice sites and severe local lattice distortion.

The values of atomic size misfit in all the *bcc*-structured samples were calculated from the atomic radius as shown in Table 4.3. The calculated values of atomic size misfit are 1.12, 4.28, 4.13 and 4.98% for TiNb, TiNbHf, TiNbHfTa and TiNbHfTaZr samples, respectively. The atomic size misfits are significant in TiNbHf, TiNbHfTa and TiNbHfTaZr because of the large differences in atomic radius between small atoms (Nb, Ti and Ta) and large atoms (Hf and Zr). The larger size misfit of TiNbHf than that of TiNbHfTa might lead to the broader peaks at the second and third coordination shells. The largest values of atomic size misfit in the HEA produced the high local strain resulting in the broadest peak. It suggested an assumption that the atomic size misfit had more effect on the local lattice strain than the number of components.

To carefully compare the level of local lattice distortion between the *fcc*- and *bcc*-structured samples, an average PDF peak width as shown in Table 5.3 were calculated by the first three PDF peaks for minimizing the effects of overlapped PDF peaks and fitting method. Although the first peak simply reflects the absolute effect of atomic size misfit [107], the clearly broader peaks at second and third peaks emphasized local lattice strain associated with the increase in the number of component. Thus, in this study the first three peaks within r = 5 Å for both two alloy systems were considered. The different information about the local structure is contained at different atomic pair distance [102]. The PDF peak slowly becomes beyond the pair-atomic interaction with increasing atomic pair distance. The near-neighbor PDF peaks reflect the discrete interatomic distances within the phase, resulting in sharper peak than that at high r [119, 123, 124]. In the PDF spectrums of the *bcc*-structured samples as shown in Figure 5.9, the blurred peak distinction are observed between the first and second peak. There are only eight nearest neighbor atoms in *bcc* lattice structure, but the close packed *fcc* lattice structure presents twelve nearest neighbor atoms. In case of local lattice distortion, the second neighbor atoms were possibly distorted close to the positions of the nearest atoms. The strong broadening is remarkably observed at the second peak, which implies high degree of lattice distortion in the *bcc*-structured alloys. Hence, the second peak should not be eliminated for the consideration.

Table 5.3 The values of FWHM for the first three peaks, the average FWHM values and the different values subtracted by the FWHM of pure metal ($\Delta FWHM = FWHM_i - FWHM_{Ni/Nb}$).

	Composition	FWHM (Å)				ΔFWHM
		1st peak	2nd peak	3rd peak	Average	
fcc-structured sample	Ni	0.2100	0.2162	0.2255	0.2172	-
	FeNi	0.2205	0.2262	0.2442	0.2303	0.0131
	FeNiCo	0.2193	0.2314	0.2380	0.2296	0.0123
	FeNiCoCr	0.2148	0.2251	0.2401	0.2267	0.0094
	FeNiCoCrMn	0.2148	0.2307	0.2484	0.2313	0.0141
bcc-structured sample	Nb	0.2038	0.2389	0.2345	0.2257	-
	TiNb	0.2429	0.3244	0.2744	0.2806	0.0548
	TiNbHf	0.2420	0.3446	0.3298	0.3055	0.0797
	TiNbHfTa	0.2581	0.3140	0.2897	0.2872	0.0615
	TiNbHfTaZr	0.2862	0.3640	0.3699	0.3401	0.1143

Figure 5.10 shows the atomic size misfit and the equivalent static atomic displacement (ΔFWHM) for *fcc*-structured and *bcc*-structured samples. The equivalent values of static atomic displacement as a function of atomic size misfit in the HEAs and their sub-alloys were determined by subtraction of the FWHM of pure metal (Ni or Nb) from the FWHM of the alloys, as discussed above. Among the *fcc*-structured alloys with a narrow range of atomic size misfit, the ΔFWHM were slightly different for about 0.01 Å. The low values of equivalent static displacement could lead to an assumption of slight lattice distortion in the FeNiCoCrMn HEA. The ΔFWHM of the *bcc*-structured TiNbHFTaZr HEA and its sub-alloys were relatively higher. The *bcc*-structured alloys obtain relatively larger range of atomic size misfit. It resulted in the larger level of ΔFWHM. It can be noticed that ΔFWHM was varied with the change of atomic size misfit. The ΔFWHM of the TiNbHfTaZr HEA with $\delta = 4.98\%$ was doubled from that of TiNbHfTa having $\delta = 4.13\%$. The larger atomic size misfit in TiNbHf might cause the higher values of ΔFWHM than that of

TiNbHfTa; meanwhile, the effect of dynamic atomic displacement in the TiNbHf might be not completely removed due to the association with its relatively lower melting point. The result suggests that the atomic size misfit had an important effect on the static atomic displacement than the number of alloy composition. The largest atomic size misfit in the TiNbHfTaZr HEA led to a significant magnitude of equivalent static atomic displacment (0.1143 Å), proportional to the large local lattice distortion. In contrast, the pronouncement for lattice distortion in the *fcc*-structured FeNiCoCrMn HEA was not evident from the result indicating the relatively small magnitude of static atomic displacement (0.0141 Å).

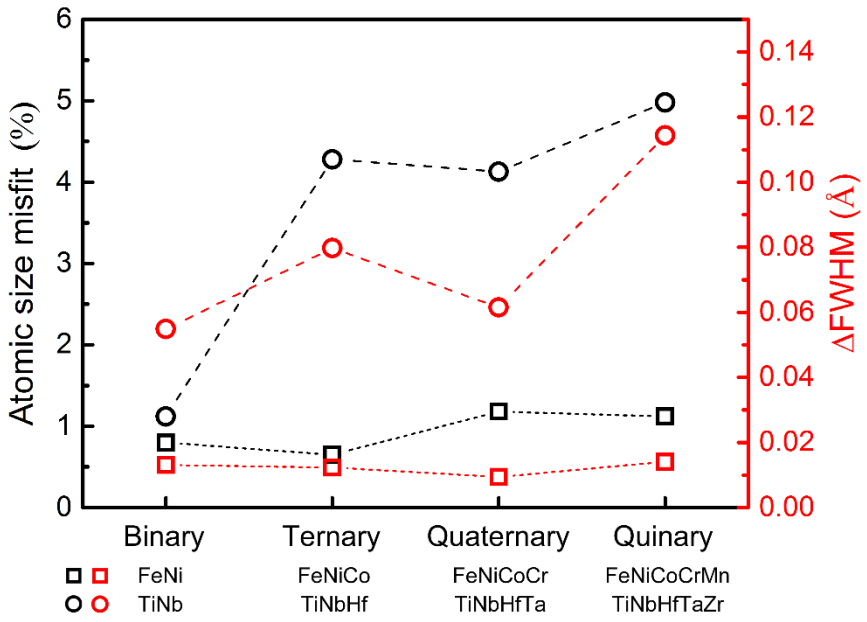

Figure 5.10 The atomic size misfit (δ) and the equivalent static atomic displacement (ΔFWHM) for the *fcc*-structured and *bcc*-structured samples.

6. Solid solution hardening in single phase high entropy alloys

It is generally known that the strength and hardness of crystalline materials is related to the resistance of dislocation mobility [4, 125]. The hardening mechanisms in the interaction with the dislocation are traditionally divided into four main factors; solid-solution hardening, grain boundary hardening, strain hardening and precipitation and/or dispersion hardening [4, 54, 126]. Other hardening factors are constraints from neighboring grains, preferred orientations and crystal structure [126].

This chapter focuses on the effect of solid solution hardening on mechanical properties of the high entropy alloys. The other three main hardening effects were controlled in order to quantify the solid solution hardening in the HEAs. In the FeNiCoCrMn and TiNbHfTaZr HEAs and their sub-alloys, the precipitation hardening was not considered due to their single phase alloys. The other two factors, work hardening and grain boundary hardening associated with grain size effect, were controlled by the thermomechanical treatment and measurement condition. This study examined the solid solution hardening by hardness and tensile tests.

6.1 Hardness of *fcc*- and *bcc*-structured high entropy alloys

The hardness as an indication of the level of solid solution hardening in the HEAs was measured in as-homogenized microstructures. The homogenization could eliminate internal stress resulted from casting and drove toward equilibrium microstructures. The FeNiCoCrMn HEA and its sub-alloys after homogenization at 1000°C for 12 hours obtained the chemical homogeneity, as measured by EDX mapping method (Figure 4.1). The TiNbHfTaZr HEA and its sub-alloys were homogenized at 1100°C for 40 hours due to their higher melting points and the chemical homogeneity of these samples were obtained (as shown in EDX maps of Figure 4.2).

Figure 6.1 presents as-homogenized microstructures for the FeNiCoCrMn HEA and its sub-alloys, and Figure 6.2 shows as-homogenized microstructures for the TiNbHfTaZr HEA and its sub-alloys. A second phase was not observed in as-homogenized microstructures of all samples. The casting defect (tiny pores) was found in as-homogenized microstructures. All as-homogenized microstructures show coarse and equiaxed grains with different grain sizes. The grain sizes estimated from SEM images were averagely 199 ± 18, 305 ± 42, 187 ± 32 and 99 ± 12 μm for FeNi, FeNiCo, FeNiCoCr and FeNiCoCrMn, respectively. For the *bcc*-structured alloys, the average grain sizes were determined as 733 ± 182, 231 ± 54, 170 ± 18 and 239 ± 17 μm for TiNb, TiNbHf, TiNbHfTa and TiNbHfTaZr, respectively. In order to minimize an effect of grain boundary hardening, the micro Vickers hardness were indented inside grains. Figure 6.3 shows the microhardness indentation marks for the FeNiCoCrMn and the TiNbHfTaZr HEAs. The indentation marks for all studied sample were smaller than the size of measured grains. The diagonal lengths of the indentation marks were approximately 50 μm for the FeNiCoCrMn HEA and its sub-alloys, whereas the diagonal lengths for the TiNbHfTaZr HEA and its sub-alloys were in the range between 30 – 45 μm.

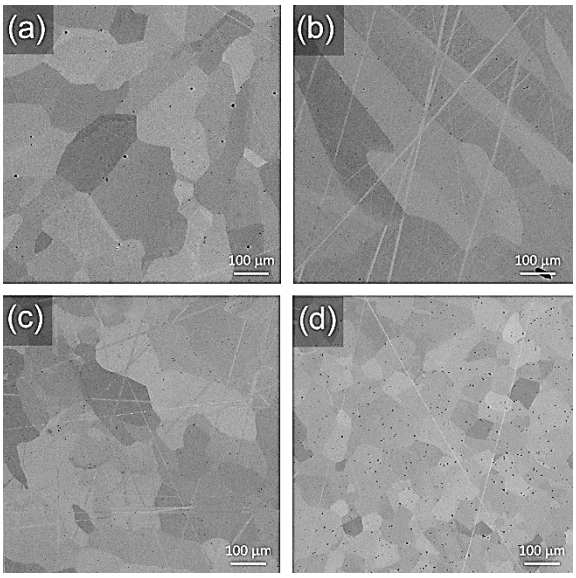

Figure 6.1 As-homogenized microstructures of (a) FeNi, (b) FeNiCo, (c) FeNiCoCr and (d) FeNiCoCrMn.

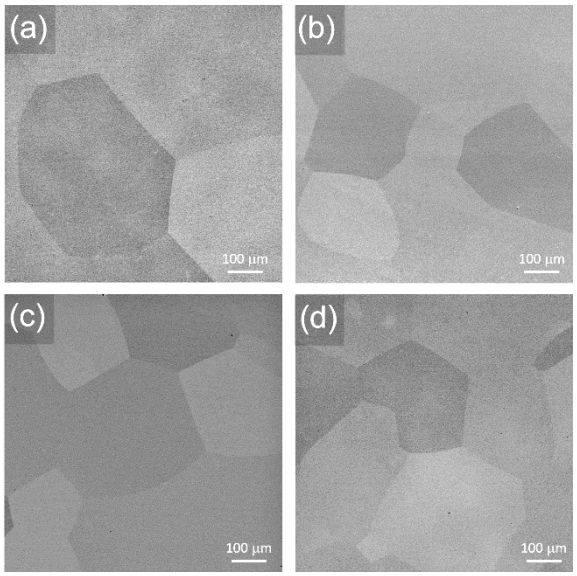

Figure 6.2 As-homogenized microstructures of (a) TiNb, (b) TiNbHf, (c) TiNbHfTa and (d) TiNbHfTaZr.

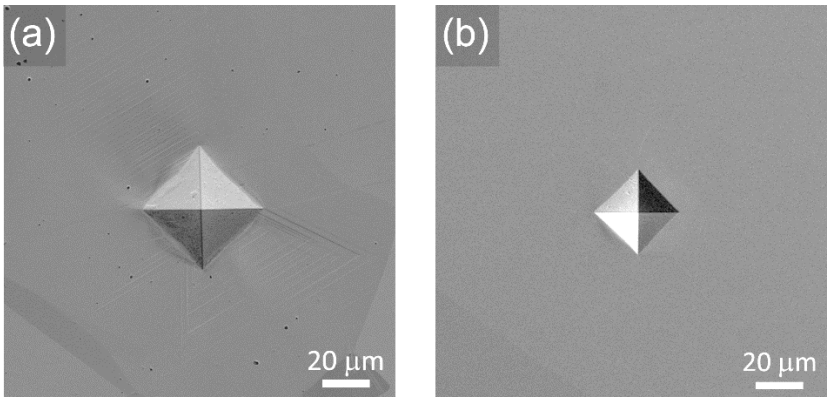

Figure 6.3 Indentation marks on as-homogenized grains of (a) FeNiCoCrMn and (b) TiNbHfTaZr HEAs

Hardness of the fcc-structured FeNiCoCrMn high entropy alloy

Table 6.1 summarizes the values of microhardness for all the samples including the reference value of annealed pure Ni [127] and Figure 6.4 presents a bar graph for a comparison of the microhardness among the samples. The hardness values of the FeNi, FeNiCo, FeNiCoCr and FeNiCoCrMn were 116 ± 2, 112 ± 2, 132 ± 2 and 129 ± 1 HV, respectively, and the reference

value of the Ni sample is 64 HV. The presence of the substitutional Fe atom in the FeNi alloy induced solid solution hardening by disrupting the periodicity of the lattice. It increased the hardness from 64 HV of pure Ni to 116 HV of theFeNi alloy. The hardness of the FeNiCo alloy was slightly different from that of the FeNi alloy; hence, the addition of Co has a slight effect on hardness change. The addition of the largest Cr atom caused large hardening in FeNiCoCr and FeNiCoCrMn due to its largest atomic radius. I. Toda-Caraballo et al. [128] studied the strengthening model which demonstrated strong strengthening effects of Cr in FeNiCo-based alloys. However, the addition of Co and Mn resulted in insignificant changes of the hardness. The hardness values of the FeNiCoCrMn HEA and its sub-alloys were in a narrow range between 112 -132 HV. The slight change in the hardness was supported by the slight pronouncements of lattice strain in this alloy system, which was investigated with the PDF method (as described in chapter 5). The small magnitudes of the lattice strain led to a slight effect of solid solution hardening on the hardness among the *fcc*-structured samples.

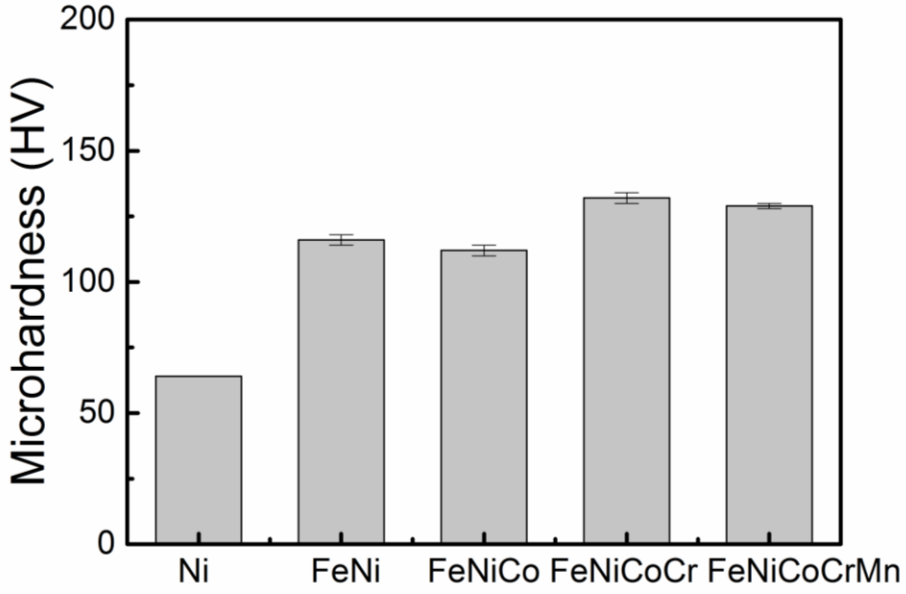

Figure 6.4 Microhardness of as-homogenized *fcc*-structured samples

Table 6.1 Microhardness of the as-homogenized *fcc*- and *bcc*-structured samples

fcc samples	Microhardness (HV)	*bcc* samples	Microhardness (HV)
Ni	64 [127]	Nb	80 [127]
FeNi	116 ± 2	TiNb	179 ± 1
FeNiCo	112 ± 2	TiNbHf	290 ± 2
FeNiCoCr	132 ± 2	TiNbHfTa	307 ± 5
FeNiCoCrMn	129 ± 1	TiNbHfTaZr	327 ± 3

Hardness of the bcc-structured TiNbHfTaZr high entropy alloy

The values of microhardness for the TiNbHfTaZr HEA and its sub-alloys are summarized in Table 6.1 including the reference value of annealed pure Nb [127] and Figure 6.5 presents a bar graph for a comparison of their microhardness. The hardness values were 179 ± 1, 290 ± 2, 307 ± 5 and 327 ± 3 HV for TiNb, TiNbHf, TiNbHfTa and TiNbHfTaZr alloys, respectively, and the reference value of the Nb sample is 80 HV. It is not surprised that the *bcc*-structured alloys were harder than the *fcc*-structured alloys because slip planes in the *bcc* structure is made more difficult than the *fcc* structure [1]. For the *bcc*-structured alloys, the hardness values increased as the chemical complexity of alloys increased. The addition of Ti induced solid solution hardening to increase the hardness from the Nb to TiNb alloy. The large increase in the hardness was also observed between the TiNb and TiNbHf alloys. This increase was caused by an increase in atomic size misfit. The values of atomic size misfit for TiNbHf, TaNbHfTa and TiNbHfTaZr were above 4%, while that of TiNb was about 1%. As investigated in chapter 5, the lattice strain increases from the Nb to TiNbHfTaZr HEAs as a result of an increase in atomic size misfit. The large atomic size misfit produce localized elastic strain fields which interact with those of dislocations [129]. By overcoming lattice distortions, the amount of energy is required for motion of dislocation, which results in hardening the materials [54, 125]. The large hardening for the Ti-Nb-Hf-Ta-Zr system might be given from the high magnitude of lattice strain associated with large atomic size misfit.

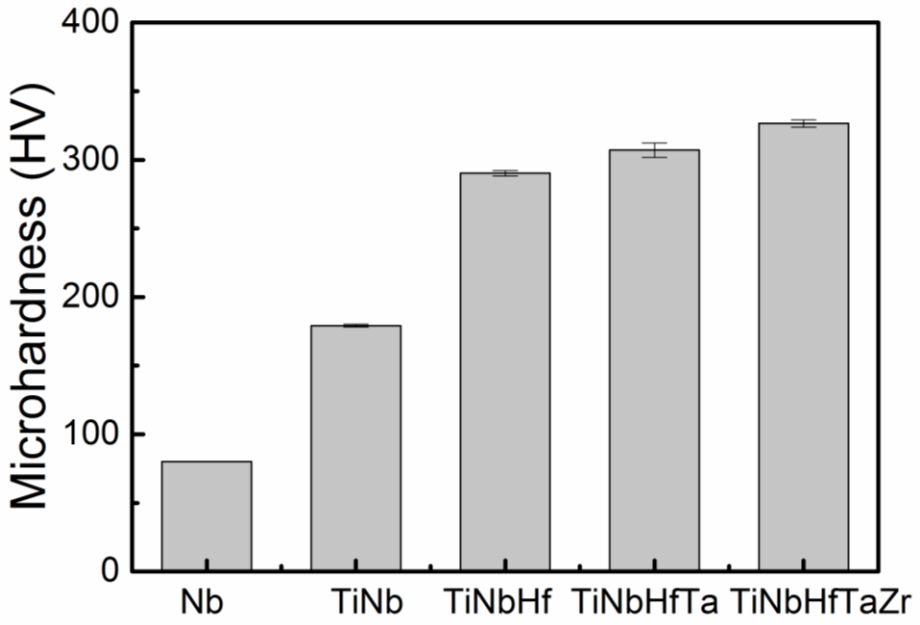

Figure 6.5 Microhardness of as-homogenized *bcc*-structured samples and indentation mark on as-homogenized grain of TiNbHfTaZr HEA in the inset.

6.2 Tensile strength of *fcc*- and *bcc*-structured high entropy alloys

To prove the solid solution hardening in the HEAs, the tensile strength is needed for a parallel study. The tensile test was conducted with thermomechanically treated samples composing of fine recrystallized grains. The sample preparation for tensile test was described in chapter 3.

Tensile strength of the fcc-structured FeNiCoCrMn high entropy alloy

For analyzing the microstructure, EBSD was used to quantify the microstructure, as listed in Table 6.2. After thermomechanical treatment, the recrystallization was achieved in all samples. All samples showed nearly free of deformed grains and main fraction of recrystallized grains. It is observed that the FeNi and FeNiCo alloys obtained the high fraction of substructured boundaries possibly due to the annealing condition (low temperature and short exposure time). Figure 6.6

presents EBSD grain orientation maps of the *fcc*-structured samples for tensile test. The microstructures were controlled to obtain average grain size between 13 – 22 μm in all alloys. The grain sizes in all samples were not significantly different; thus, the effect of grain size hardening was controlled in order to compare the level of solid solution hardening between the alloys.

Table 6.2 Microstructural analysis of *fcc*-structured tensile tested samples evaluated on EBSD maps.

Alloys	Grain Size (μm)	Residual strain analysis			Twin Σ3 (%)
		Undeformed (%)	Substructured (%)	Deformed (%)	
Ni	21.1 ± 1.5	94	6	0	2
FeNi	13.4 ± 2.6	75	25	0	14
FeNiCo	12.9 ± 1.3	87	13	0	14
FeNiCoCr	18.4 ± 1.3	92	8	0	12
FeNiCoCrMn	21.9 ± 2.4	96	4	0	14

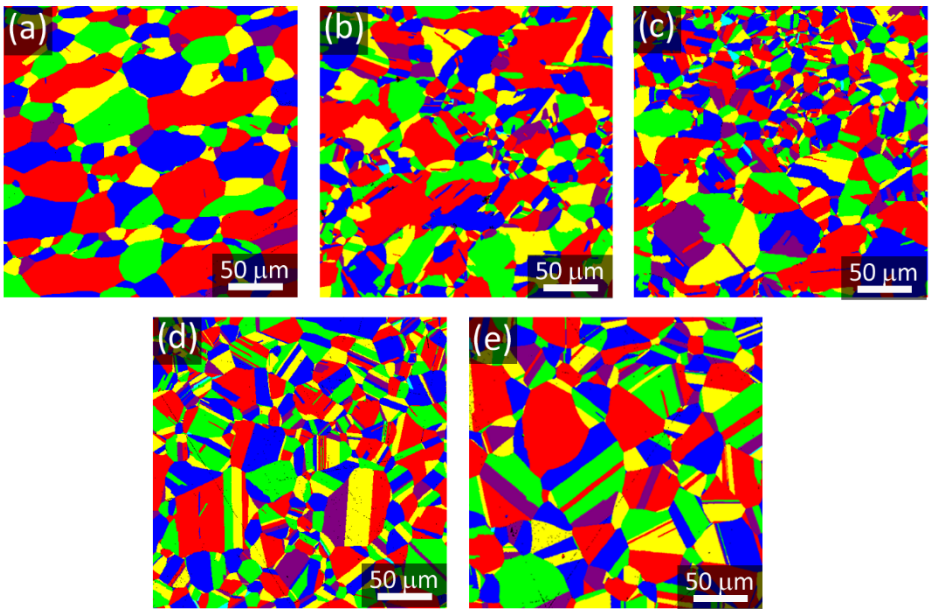

Figure 6.6 EBSD grain orientation maps of (a) Ni, (b) FeNi, (c) FeNiCo, (d) FeNiCoCr and (e) FeNiCoCrMn.

It was observed the concentration of annealing twin boundaries (measured as $\Sigma 3^n$, n = 1, 2, 3 in coincidence site lattice notation) in the FeNiCoCrMn HEA and its sub-alloys. The annealing twin formation is related to grain boundaries migration due to the occurrence of stacking errors [130]. It is commonly known that Ni-based alloys with low stacking fault energy (SFE) shows twin grains during annealing [131]. The twin boundaries is also found in other low SFE materials. The stacking fault energy (SFE) of nickel is between 120 – 130 mJ/m^2 [132] and the SFEs of FeNi, FeCoNi, FeNiCoCr and FeNiCoCrMn are 79, 31 , 25 and 25 mJ/m^2 [1, 133, 134], respectively. The value of SFE decreases with increasing number of elements [1]. Figure 6.7 shows the large amount of Σ3 boundaries; while the quantities of Σ9 and Σ27 boundaries were relatively limited. The formation of Σ9 and Σ27 boundaries are responsible for the multiple twinning [135]. The major attention was paid on the twin formation of Σ3 boundaries. The FeNiCoCrMn HEA and its sub-alloys obtained 12 – 14% of Σ3 twin boundaries fraction, but the pure Ni sample presented the small fraction about 2% due to its relatively high SFE. It is considered that the lowering the SFE is effective to reduce the twin boundary energy [136, 137, 138], which stimulates the formation of annealing twinning boundaries. The annealing temperature and time also influences the twin formation during grain boundary mobility [139].

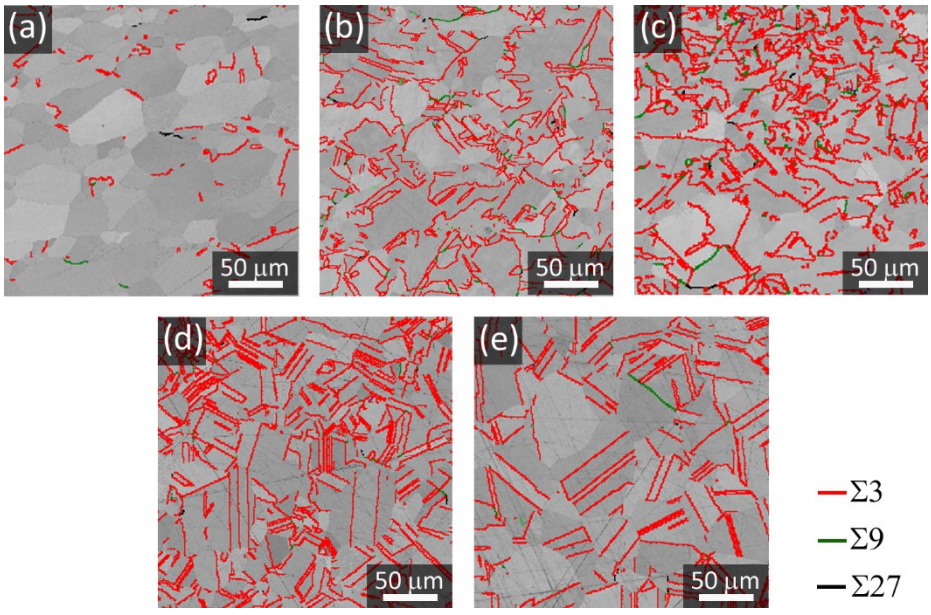

Figure 6.7 EBSD special grain boundaries (Σ3, Σ9 and Σ27) maps of (a) Ni, (b) FeNi, (c) FeNiCo, (d) FeNiCoCr and (e) FeNiCoCrMn.

Fig. 6.8 presents the true tensile stress-strain curve. The tensile mechanical properties in terms of yield strength ($\sigma_{0.2}$), ultimate strength (σ_{max}), uniform elongation (e_u) and total elongation (e_t) are summarized in Table 6.3. The total elongations of all samples were larger than 40%. The necking was clearly observed for all samples during tensile test. The uniform elongation is determined at the maximum stress and better represents ductility or formability of these materials in uniaxial deformation. The uniform elongation of the sample is also large; between 32 – 44%. These large elongations were because of the *fcc* crystal structure having 12 slip systems, high concentration of annealing twin boundaries. The serration behaviors were observed as saw-like curve on the stress-strain curves of FeNiCo, FeNiCoCr and FeNiCoCrMn and also found by other studies [13]. R. Carroll et al. [140] reports that the serration increases with the number of constituent elements in the HEA. It is suggested that various microstates of the plastic deformation (introduced by the interaction between moving dislocations and substitutional atoms) hint the serration behavior of the HEAs [141, 142].The serrated flows could be related to deformation-induced twinning [13, 16, 143]. It is reported that the deformation twins were observed in the FeNiCoCr and FeNiCoCrMn alloys during plastic deformation [144, 145]. The values of yield strength ($\sigma_{0.2}$) were 60, 197, 154, 177 and 156 MPa for the Ni, FeNi, FeNiCo, FeNiCoCr and FeNiCoCrMn, respectively. By reviewing the yield strength of the FeNiCoCrMn HEA, it revealed a wide range of yield strength (100 – 600 MPa) and elongation (40 – 60%) dependent on grain size and processing [1, 11, 35]. In this study, the yield strength of the HEA was in the range of reference values. The pure Ni showed the lowest yield strength. The addition of Fe into the FeNi alloys enhanced the yield strength by the effect of solid solution hardening, similar to the hardness results. However, an increase in the number of substitutional elements did not lead to a significant enhancement in the yield strength between the HEA and its sub-alloys. The microstructural features (in terms of grain size, grain size distribution and a level of residual strain) also had an effect on the mechanical properties of the alloys. The small changes in the yield strength suggested that the level of solid solution hardening in the HEA was insignificant, compared to its sub-alloys.

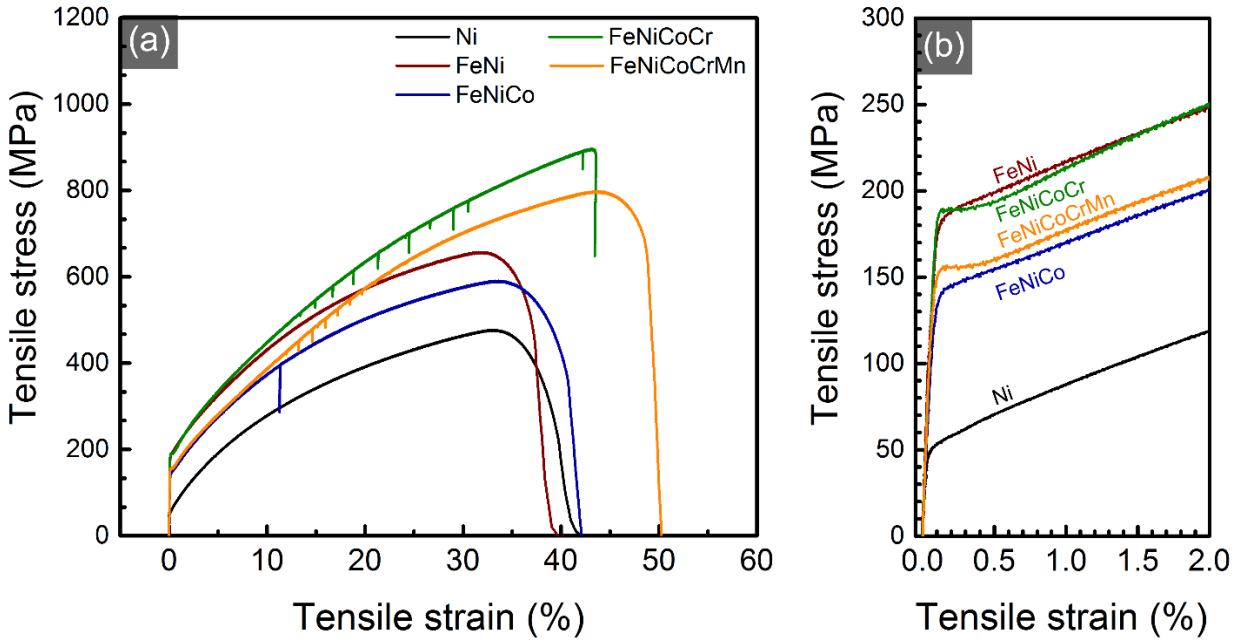

Figure 6.8 (a) Overall tensile stress-strain curve of the thermomechanically treated *fcc*-structured samples and the curves between 0 – 2% tensile strain.

Table 6.3 Tensile mechanical properties in terms of yield strength ($\sigma_{0.2}$), ultimate strength (σ_{max}), uniform elongation (e_u) and total elongation (e_t) of *fcc*-structured samples after thermomechanical treatment.

bcc samples	$\sigma_{0.2}$ (MPa)	σ_{max} (MPa)	e_u (%)	e_t (%)
Ni	60	477	33	42
FeNi	192	657	32	40
FeNiCo	147	591	33	42
FeNiCoCr	189	896	43	43
FeNiCoCrMn	156	798	44	50

After the tensile failure of the FeNiCoCrMn HEA, pronounced necking was evident as shown in Figure 6.9 (a). It indicated ductile behavior of the HEA [146]. Figure 6.9 (b) and (c) are the fractography characterized by numerous deep dimples through the formation and coalescence of microvoids. Cr-Mn rich oxide particles were found inside the voids; it was possibly an initial site of a crack. N. D. Stepanov [112] reported that the oxide particles were formed during annealing

at low temperature (873 – 1073 K) in the FeNiCoCrMn HEA and these particle was not found in the HEA after annealing at high temperature (1173 K). This was supported by microstructural observation in this work that the HEA annealed at 1223 K presented a single phase without any second phase. Hence, it was possible that this oxide particles were formed during the tensile test. The presence of these particles might give no adverse effect on the mechanical properties because the HEA was as ductile as the FeNi and FeNiCo alloys, which had no Cr-Mn oxide particles. Figures 6.9 (d) and (e) present the lateral surface revealing intensively slip band. Numerous slip bands in different orientations were formed during tensile test, resulting in the extensive ductility in the *fcc*-structured FeNiCoCrMn HEA.

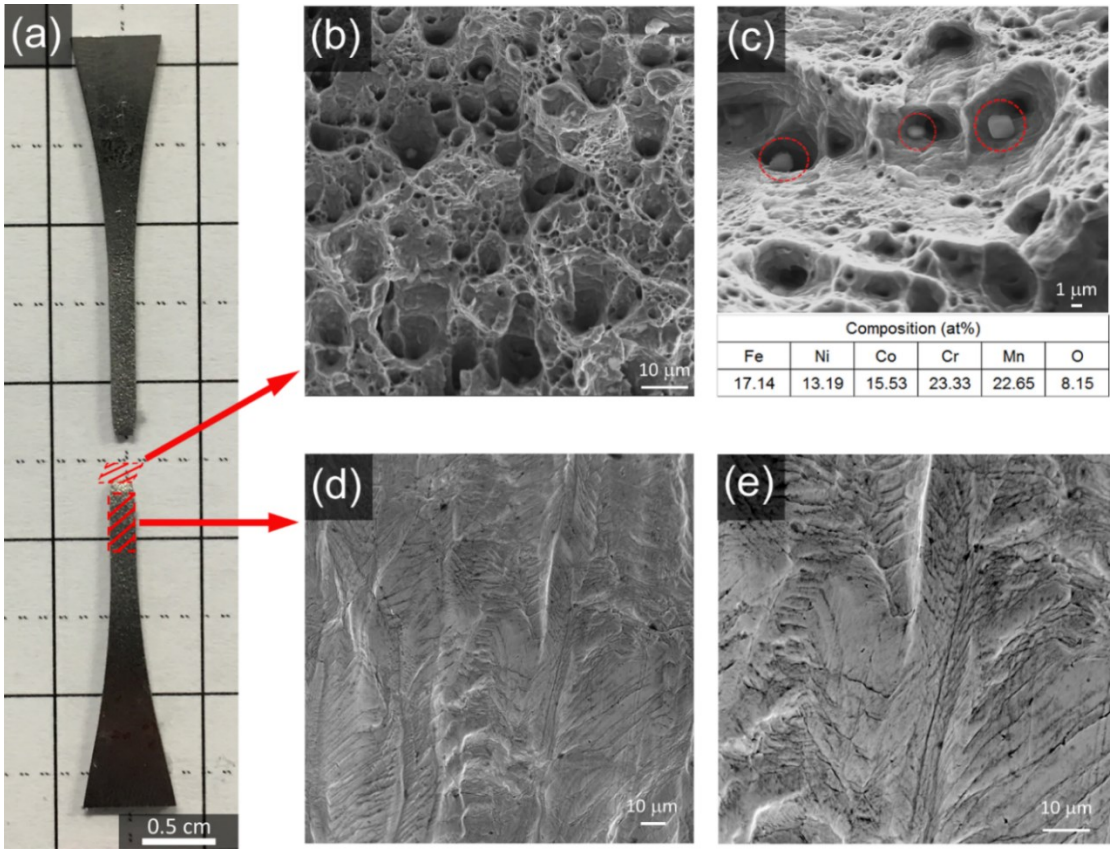

Figure 6.9 (a) FeNiCoCrMn HEA after tensile test, (b) - (c) fracture surface and EDX spectrum of Cr-Mn rich particle indicated by red circles and (d) – (e) lateral surface.

Tensile strength of the bcc-structured TiNbHfTaZr high entropy alloy

Table 6.4 summarizes the results of post processing on EBSD maps of the *bcc*-structured samples. All samples obtained free of deformed grains. With the exception of the TiNb sample, all samples were almost fully recrystallized and obtained slight fraction of substructured grains. The high fraction of substructure in the TiNb sample possibly was resulted by insufficient annealing time. Figure 6.10 shows the EBSD grain orientation maps of the as-thermomechanically treated *bcc*-structured samples. The *bcc*-structured samples revealed equiaxed and recrystallized grains. Although the microstructure of the TiNb was slightly different from the others, the average grain sizes was not significantly different. The grain sizes of the TaNbHf, TiNbHfTa and TiNbHfTaZr samples lied in the range between 14 -22 μm, but the grain size of the TiNb sample was larger to 29 μm. The annealing twin boundaries were slightly observed as presented in Figure 6.11. The annealing twin boundaries were relatively less in this alloy system, compared to the *fcc*-structured samples. The annealing twins are slightly formed in *bcc*-structured materials due to their high stacking fault energy [147]. The values of the stacking fault energy of the TiNbHfTaZr HEA and its sub-alloys were not found.

Table 6.4 Microstructural analysis of *bcc*-structured tensile tested samples evaluated on EBSD maps.

Alloys	Grain Size (μm)	Residual strain analysis			Twin Σ3 (%)
		Undeformed (%)	Substructured (%)	Deformed (%)	
TiNb	28.9 ± 3.1	44	56	0	1
TiNbHf	14.5 ± 1.5	97	3	0	2
TiNbHfTa	14.3 ± 0.7	95	5	0	2
TiNbHfTaZr	22.4 ± 1.5	96	4	0	2

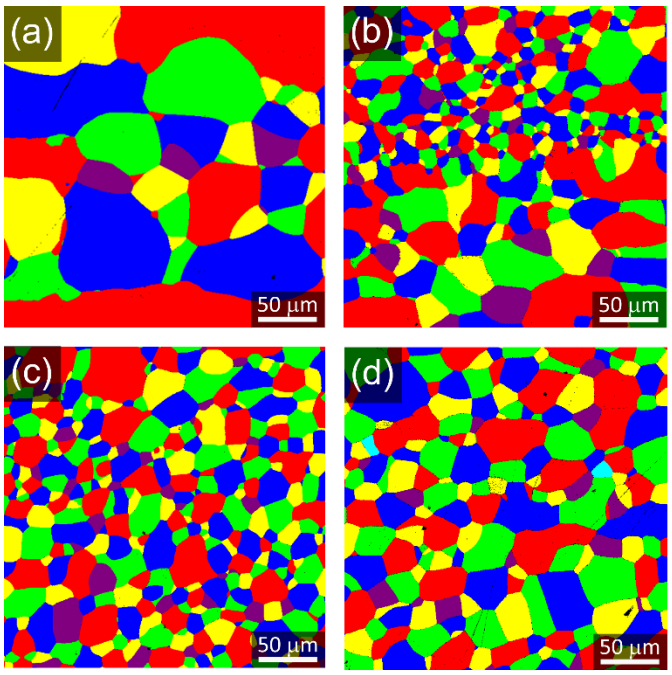

Figure 6.10 EBSD grain orientation maps of (a) TiNb, (b) TiNbHf, (c) TiNbHfTa and (d) TiNbHfTaZr.

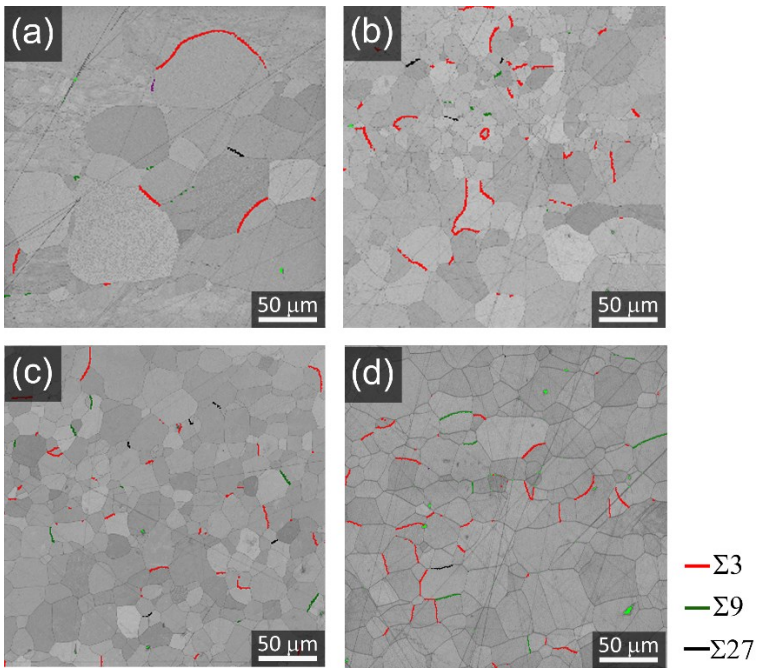

Figure 6.11 EBSD special grain boundaries (Σ3, Σ9 and Σ27) maps of (a) TiNb, (b) TiNbHf, (c) TiNbHfTa and (d) TiNbHfTaZr.

The true tensile stress-strain curves are presented in Figure 6.12 and the tensile mechanical properties are summarized in Table 6.5. The yield strength ($\sigma_{0.2}$) were 574, 857, 783 and 985 MPa for the TiNb, TiNbHf, TiNbHfTa and TiNbHfTaZr, respectively. The yield strength of Nb collected from the reference is 207 MPa. The yield strength of the TiNbHfTaZr HEA was comparable with the values of other works, such as 1073 MPa for as-cast sample with 120 μm of grain size [84] and 966.0 - 973.3 MPa for theoretically calculated values corresponding the grain sizes between 100 - 200 μm [54]. The yield strength increased with the number of constituent elements. The addition of new constituent elements enhanced the solid solution hardening associated with intrinsic local lattice strain. The atomic size misfit in the *bcc*-structured samples was large and subsequently caused the high level of local lattice strain, as discussed in chapter 5. Strictly speaking, the lower yield strength of TiNbHfTa than those of TiNbHf were probably related to the smaller level of local lattice strain and homogeneity of grain size distribution homogeneous. The recrystallized grain sizes of the TiNbHf were largely distributed, obtaining the smaller grain sizes in the middle of sample as shown in Figure 6.11 (b). This heterogeneous grain size distribution strengthened the TiNbHf sample. However, it led to a conflict that the values of the microhardness for TiNbHf was lower than that of TiNbHfTa. The solid solution hardening in the TiNbHfTaZr HEA was higher than the FeNiCoCrMn HEA due to the larger lattice strain. Despite the small twin density and *bcc* lattice structure with no truly close-packed planes, the elongations in these alloys were not extremely low. The slight necking was observed in all *bcc*-structured samples. The total elongation (e_t) can be represented ductility of the samples. The total elongation of the TiNbHf, TiNbHfTa and TiNbHfTaZr samples were 11, 17 and 12%, respectively. The TiNb sample presented relatively lower total elongation (5%) because of the higher fraction of substructure. For the uniform elongation (e_u), the values were 1, 11, 12 and 7% for the TiNb, TiNbHf, TiNbHfTa and TiNbHfTaZr samples, respectively. The trend in the uniform elongation change was not different from that of the total elongation. In addition to the stress-strain curve of the TiNbHfTaZr HEA, the serration behavior characterized by saw-like curve was observed. The serration flow in the TiNbHfTaZr HEA might related to the deformation twinning under the tensile load. The deformation twins was reported to be observed in the TiNbHfTaZr during plasticity [60].

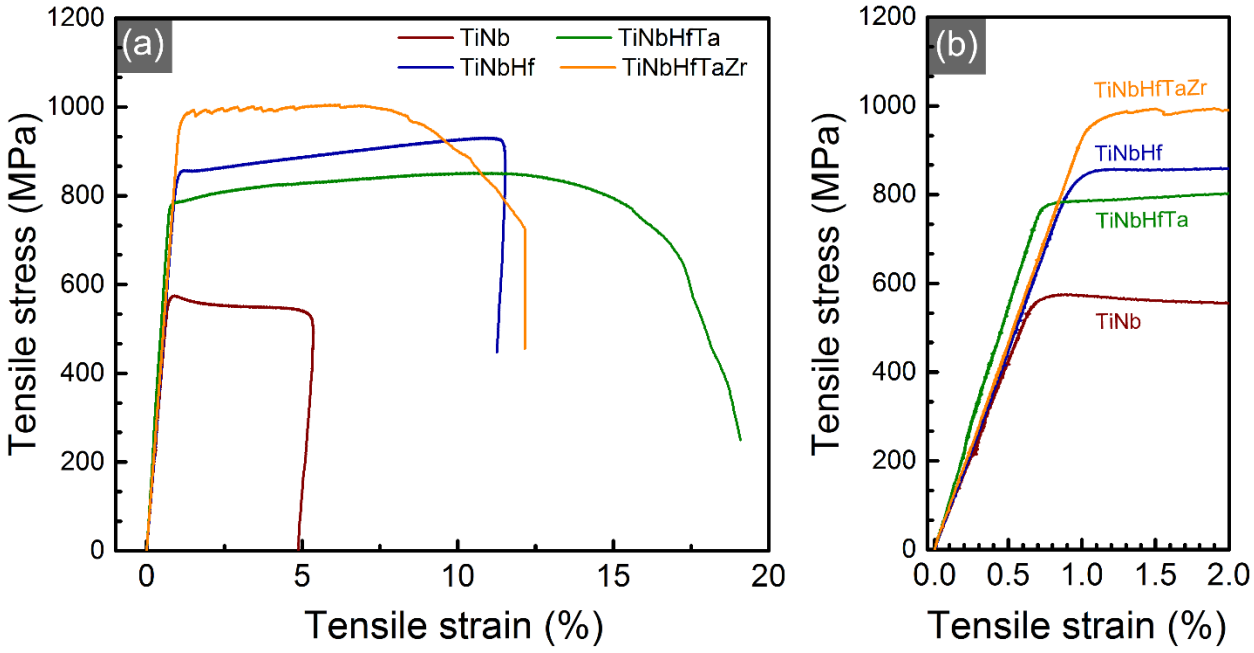

Figure 6.12 (a) Overall tensile stress-strain curves of the thermomechanically treated *bcc*-structured samples and (b) the curves between 0 – 2% tensile strain.

Table 6.5 Tensile mechanical properties in terms of yield strength ($\sigma_{0.2}$), ultimate strength (σ_{max}), uniform elongation (e_u) and total elongation (e_t) of *bcc*-structured samples after thermomechanical treatment.

bcc samples	$\sigma_{0.2}$ (MPa)	σ_{max} (MPa)	e_u (%)	e_t (%)
Nb[127]	207	275	-	30
TiNb	574	575	1	5
TiNbHf	857	931	11	11
TiNbHfTa	783	852	12	17
TiNbHfTaZr	985	1005	7	12

Figure 6.13 shows the fracture and lateral surfaces of the TiNbHfTaZr HEA after tensile failure. Figure 6.13 (a) indicated that the failure was occurred by shear and necking was not apparently seen on the sample in contrast to the FeNiCoCrMn HEA sample. The presence of shallow dimples on the fracture surfaces indicated a ductile fracture mode of the TiNbHfTaZr HEA. In a comparison with the fractography of the FeNiCoCrMn HEA, the dimples of the

TiNbHfTaZr HEA were shallower. It is well known that the shallower dimples indicate less ductility [148]. The lateral surfaces (in Figure 6.13 (d) and (e)) shows observable grain structures and slight amount of slip bands. These behaviors presented ductile fracture mode in the TiNbHfTaZr HEA.

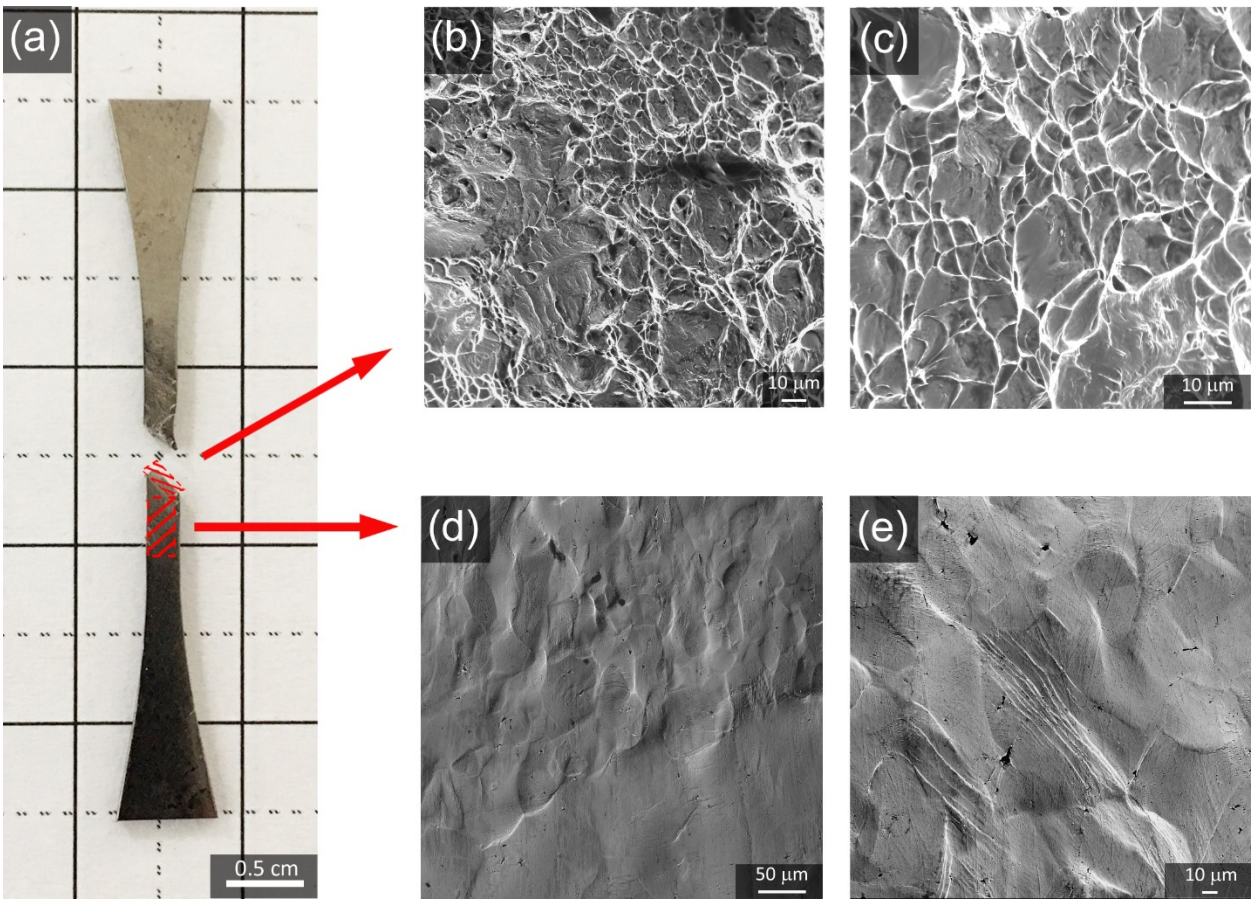

Figure 6.13 (a) TiNbHfTaZr HEA after tensile test, (b) - (c) fracture surface and (d) – (e) lateral surface.

For understanding better the effect of solid solution hardening on the HEAs compared to their sub-alloys, the correlation between local lattice strain and solid solution hardening was made in the following discussion. Traditionally, it has been known that the most important mechanism of solid solution hardening is correlated with the elastic interactions between the local stress field of solute atoms and surrounding dislocations [83, 149, 150, 151]. In HEAs with equiatomic ratios

of constituent elements, it is indistinguishable solvent and solute atoms. The classic solid solution hardening model in a conventional dilute solid solution may become invalid for the multi-component solid solutions due to rough consideration of the effect of serious lattice distortion associated with high concentration of substitutional atoms [13, 128]. Recently, the expression of the solid solution hardening in HEAs involved the presences of multiple solute atoms, the elastic interaction due to atomic size misfit, interatomic bonds and lattice distortion [128].

Figure 6.14 shows the correlation between the level of local lattice strain, microhardness and tensile yield strength for several samples having a range of chemical complexity. The level of microhardness and tensile yield strength were relatively higher in the *bcc*-structured samples than those of the *fcc*-structured samples. An increase in constituent number slightly increased the both hardness and tensile yield strength for the *fcc*-structured alloy system; in contrast, they rose significantly up with the number of constituent elements in the *bcc*-structured alloys. These changes indicate that the number of constituent elements is not a key factor for the enhancement of hardness and yield strength. As presented in Figure 6.14, the changes in both hardness and tensile yield strength is a function of the local lattice strain in a term of the equivalent static displacement. As discussed in chapter 5, the increase in the number of the constituent elements for the *fcc*-structured samples caused the small change in the static displacement from the unary sample (Ni) to the quinary alloy (FeNiCoCrMn). This small change of the static displacement in the *fcc*-structured alloy system caused the similar levels of hardness and tensile yield strength with an increase in the number of the constituent elements. The solid solution hardening in the FeNiCoCrMn HEA and its sub-alloys was not anomalously large due to the small level of the static displacement. On the contrary to the *fcc*-structured alloy system, an increase in the number of the constituent elements in the *bcc*-structured samples produced the large local lattice strain due to large atomic size misfits. This large increase in lattice strain led to large solid solution hardenability and strengthening ability, especially between the unary Nb and the ternary TiNbHf alloy. The addition of Ta for the TiNbHfTa alloy lowered local lattice strain because of smaller atomic size misfit than that of the TiNbHf alloy. This might decrease the tensile yield strength. The hardness and the yield strength of the TiNbHfTa alloy were remarkably higher than that of TiNb, although the magnitude of the relative local lattice strain in the TiNbHfTa alloy was slightly higher. It is because the presence of more constituent elements in the quaternary alloy resulted in more intensive elastic interaction between a dislocation and the strain field of multiple atoms species.

Among all studied samples, the TiNbHfTaZr HEA presented the highest levels of hardness and tensile yield strength due to the largest local lattice strain. It could be drawn that solid solution hardenability and strengthen ability are dependent on local lattice strain, which is induced by the atomic size misfit.

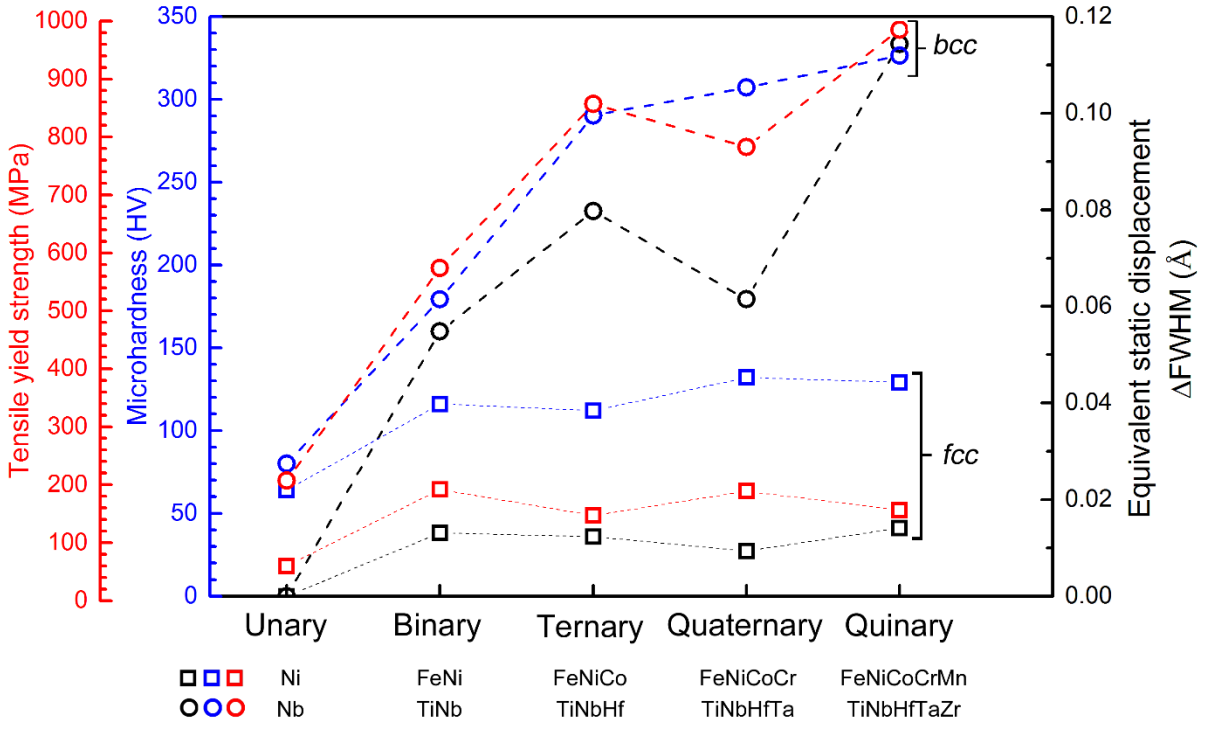

Figure 6.14 Microhardness, tensile yield strength and relative local lattice strain for the *fcc*- and *bcc*-structured samples.

6.3 Correlation between atomic size misfit and solid solution hardening in Ti-Nb-Hf-Ta-Zr system

The results in the previous section indicate that the atomic size misfit (δ) strongly correlates to the level of lattice distortion and the solid solution strengthening. An extension of atomic size misfit range is needed to clarify the effect. Figure 6.15 shows the values of atomic size misfit (δ)

for all studied samples. With the values of the atomic size misfit of the equiatomic *fcc*- and *bcc*-structured samples, there are gaps of the atomic size misfit, such as a gap between 1 and 4% and gap between 4 -5%. The new compositions were developed to fill these gaps and the compositions were created based on the composition of the equiatomic TiNbHfTaZr HEA due to their different atomic radius of the constituent elements.

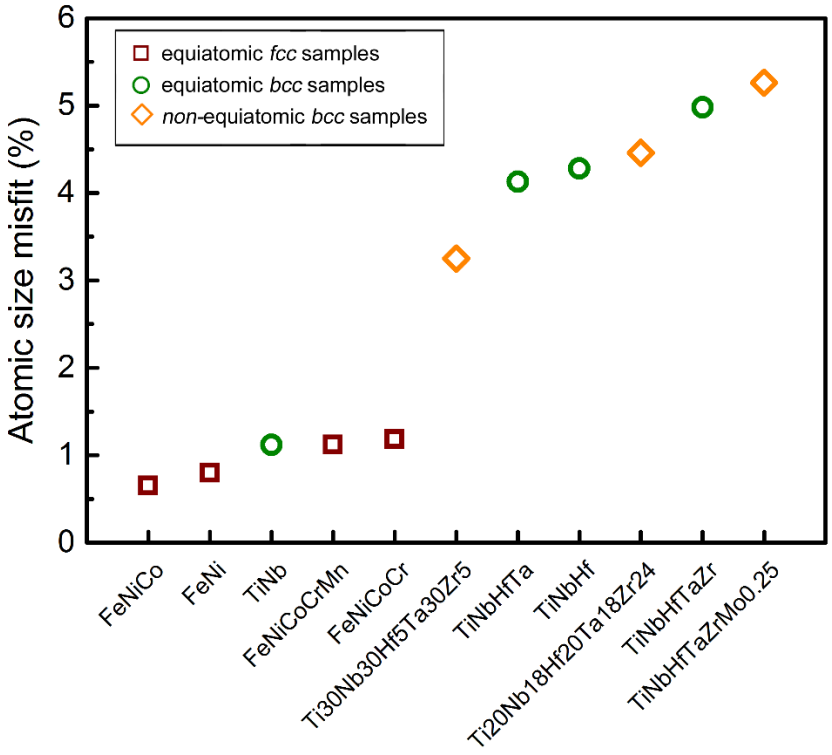

Figure 6.15 The values of atomic size misfit (δ) for the samples in this section comparing with equiatomic *fcc*- and *bcc*-structured samples.

The selected compositions are $Ti_{30}Nb_{30}Hf_5Ta_{30}Zr_5$, $Ti_{20}Nb_{18}Hf_{20}Ta_{18}Zr_{24}$ and $TiNbHfTaZrMo_{0.25}$ (in atomic ratio). The configurational entropy (ΔS_{conf}), enthalpy of mixing (ΔH_{mix}) and atomic size misfit (δ) for the studied samples are listed in Table 6.6. To complete the gaps of the atomic size misfit, the $Ti_{30}Nb_{30}Hf_5Ta_{30}Zr_5$ ($\delta \sim 3.25\%$) and $Ti_{20}Nb_{18}Hf_{20}Ta_{18}Zr_{24}$ ($\delta \sim 4.46\%$) alloys were designed. The $TiNbHfTaZrMo_{0.25}$ alloy was created in order to have the atomic size misfit larger than the TiNbHfTaZr HEA ($\delta \sim 4.98\%$). The atomic size misfit of the

TiNbHfTaZr is likely maximum for this alloy system. The addition of Mo can increase the atomic size misfit to reach nearly the maximum theoretical value for solid solution limit ($\delta \leq 6.6\%$) [31]. The ΔH_{mix} for all the alloys are positive and close to zero, which suggest the high possibility for solid solution formation [12, 30, 31]. The ΔS_{conf} for these samples are between the ΔS_{conf} of the equiatomic quaternary TiNbHfTaHf and quinary TiNbHfTa alloys, which is highly favorable to stabilize the solid solutions [12, 30].

Table 6.6 Melting points (T_m), configurational entropy (ΔS_{conf}), enthalpy of mixing (ΔH_{mix}) and atomic size misfit (δ) for the studied samples.

Sample	T_m* (K)	ΔS_{conf} (J/K·mol)	ΔH_{mix} (kJ/mol)	δ (%)
$Ti_{30}Nb_{30}Hf_5Ta_{30}Zr_5$	2626	11.50	1.92	3.25
$Ti_{20}Nb_{18}Hf_{20}Ta_{18}Zr_{24}$	2487	13.33	2.65	4.46
TiNbHfTaZr	2524	13.38	2.72	4.98
$TiNbHfTaZrMo_{0.25}$	2542	14.34	2.22	5.26

*Calculated by using equation 2.5 with melting points of each element form the reference [108].

In this section, the studied samples including the equiatomic TiNbHfTaZr HEA were investigated in as-homogenized button-shaped ingots. Figure 6.16 presents X-ray diffraction patterns of the samples. The XRD patterns of all studied samples indicate single *bcc*-structured solid solution phase with variation of lattice parameter. The lattice parameters were determined as 3.3321, 3.4438, 3.4136 and 3.4095 Å for $Ti_{30}Nb_{30}Hf_5Ta_{30}Zr_5$, $Ti_{20}Nb_{18}Hf_{20}Ta_{18}Zr_{24}$, TiNbHfTaZr and $TiNbHfTaZrMo_{0.25}$, respectively. It can be mentioned that the lattice parameter of $Ti_{30}Nb_{30}Hf_5Ta_{30}Zr_5$ is obviously lower, possibly due to the lowest atomic size misfit. Figure 6.17 presents the SEM micrographs of as-homogenized samples. It was observed the single solid solution phase with large equiaxed grains in the $Ti_{20}Nb_{18}Hf_{20}Ta_{18}Zr_{24}$, TiNbHfTaZr and $TiNbHfTaZrMo_{0.25}$ alloys. The as-homogenized $Ti_{30}Nb_{30}Hf_5Ta_{30}Zr_5$ presented dendritic microstructure. The annealing at 1373 K for 32 hours was not sufficient to homogenize the microstructure of the $Ti_{30}Nb_{30}Hf_5Ta_{30}Zr_5$ sample due to its relatively higher melting point.

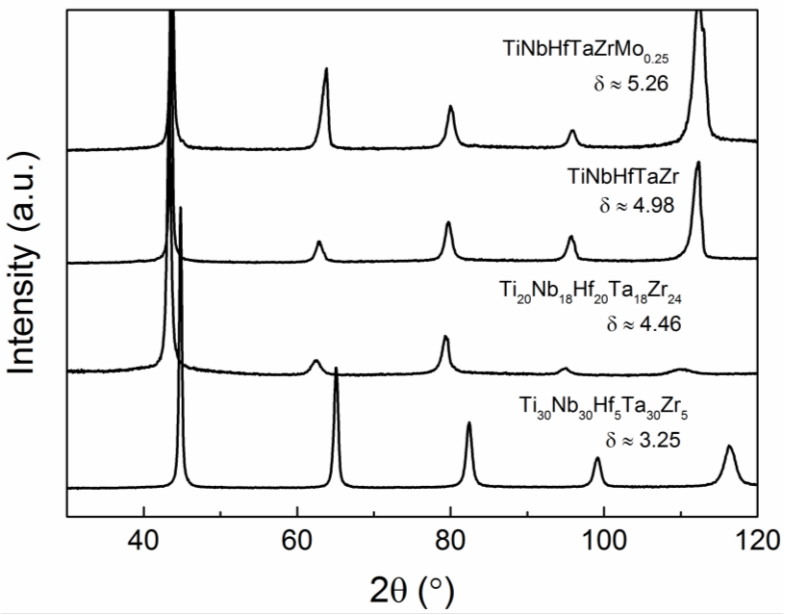

Figure 6.16 X-ray diffraction patterns of as-homogenized $Ti_{30}Nb_{30}Hf_5Ta_{30}Zr_5$, $Ti_{20}Nb_{18}Hf_{20}Ta_{18}Zr_{24}$, TiNbHfTaZr and $TiNbHfTaZrMo_{0.25}$ alloys.

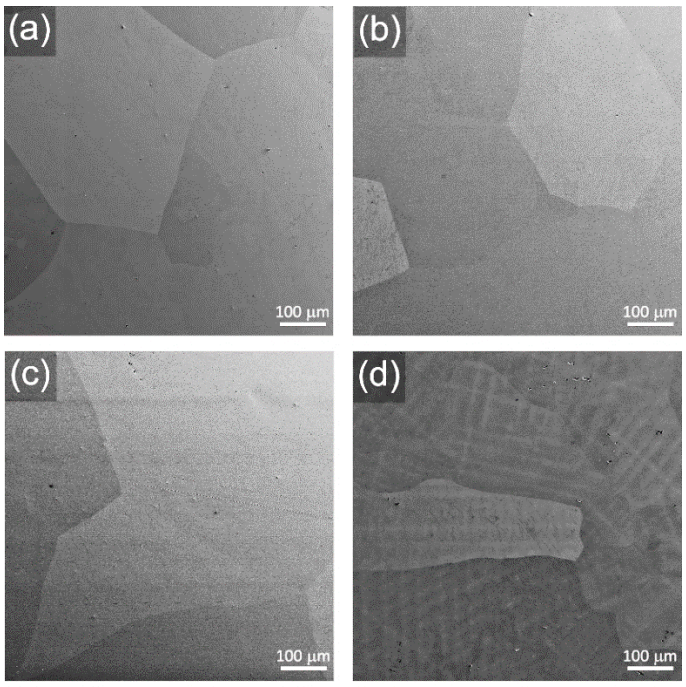

Figure 6.17 As-homogenized microstructures of (a) $TiNbHfTaZrMo_{0.25}$, (b) TiNbHfTaZr, (c) $Ti_{20}Nb_{18}Hf_{20}Ta_{18}Zr_{24}$ and (d) $Ti_{30}Nb_{30}Hf_5Ta_{30}Zr_5$ alloys.

Recently, it is reported that the hardness of the TiNbHfTaZr HEA increased with the time of annealing at 2073 K due to the formation of local chemical clustering [152]. Hence, in this thesis, suitable annealing time and water quenching after heat treatment were used to limit the diffusivities for the clustering formation. The TiNbHfTaZr sample showed the hardness of 338 MPa, similar to the value of as-homogenized TiNbHfTaZr rod (in section 6.1). These similar values of the TiNbHfTaZr HEA may indicates that the other effects besides solid solution hardening on hardness were controlled. Thus, the effect of solid solution hardening can be compared among the samples.

Figure 6.18 shows the hardness of as-homogenized samples as a function of atomic size misfit. The hardness increased as a function of atomic size misfit. The $TiNbHfTaZrMo_{0.25}$ with δ ~ 5.26% showed the highest value of the hardness (394 HV) among all studied samples. It suggests that the introduction of Mo can contribute to large atomic size misfit and strong atomic interactions between larger numbers of constituent elements. Although the as-homogenized $Ti_{30}Nb_{30}Hf_5Ta_{30}Zr_5$ shows dendritic microstructure, it obtains the lowest hardness value due to its smallest atomic size misfit. In chapter 5, the investigation of the lattice distortion with the PDF method demonstrated that the large atomic size misfit was attributed to the large local lattice strain. It can be said that the sample with the large atomic size misfit obtains the large solid solution hardening due to the large lattice strain. Figure 6.19 shows the microhardness as a function of atomic size misfit for non-equiatomic *bcc* alloys and equiatomic *bcc* alloys (investigated in previous sections). It is clear that the hardness increases with the magnitude of the atomic size misfit for the *bcc*-structured samples.

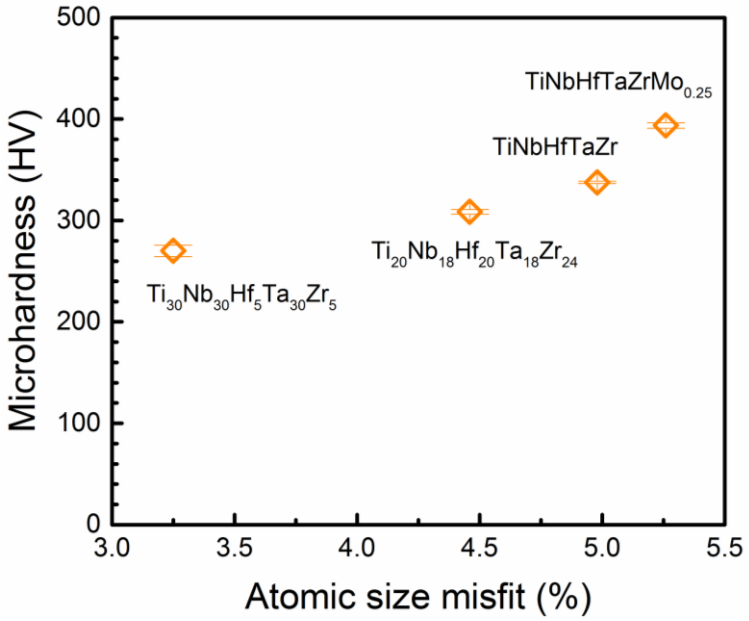

Figure 6.18 Correlation between microhardness and atomic size misfit for $Ti_{30}Nb_{30}Hf_5Ta_{30}Zr_5$, $Ti_{20}Nb_{18}Hf_{20}Ta_{18}Zr_{24}$, TiNbHfTaZr and $TiNbHfTaZrMo_{0.25}$ alloys.

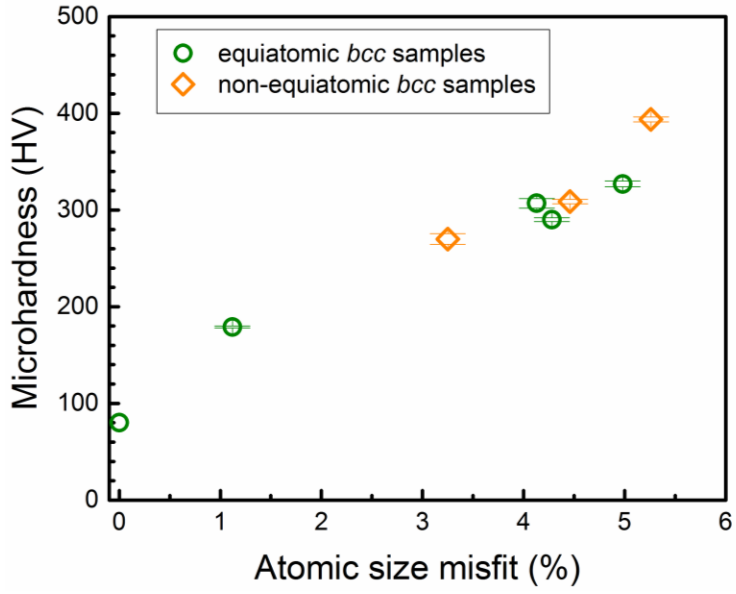

Figure 6.19 Correlation between microhardness and atomic size misfit for the *bcc*-structured samples.

It is well known that substitutional solid solution hardening is a result of the elastic interaction between dislocations and atoms in the lattice [153, 154]. A model for a prediction of solid solution hardening in binary alloys was proposed. However, in HEAs or multiple component alloys, the chemical complexity in HEAs causes a different behavior of solid solution hardening. The model for HEAs is generally adapted from existing models in conventional alloys. The approach is expressed in the form of the following equation [128]:

$$\Delta\sigma_{ss} = \left(\sum_i B_i^{3/2} X_i\right)^{2/3} \tag{6.1}$$

where $\Delta\sigma_{ss}$ is the level of solid solution hardening, X_i is the i solute content and B_i is a constant dependent on the shear modulus μ of the alloy, the misfit parameter ε_i and a fitting constant Z

$$B_i = 3\mu\varepsilon_i^{4/3} Z \tag{6.2}$$

where $\varepsilon_i = ({\varepsilon_i^b}^2 + \alpha^2 {\varepsilon_i^G}^2)^{1/2}$, ε_i represents the effects of elastic misfit (ε_i^G) and atomic size misfit (ε_i^b). The modulus misfit and the atomic size effect are attributed to the elastic interaction for solid solution hardening. It is reported that the modulus misfit is less important than the atomic size effect [128, 153, 155]. The equation 6.1 can be simplified in the following formula [155]:

$$\Delta\sigma_{ss} = k{\varepsilon_i^b}^{4/3} {X_i}^{2/3} \tag{6.3}$$

where k is the reduced form of the other parameters.

From the equation 6.3 and a neglect of the elastic misfit effect, it can indicate that the level of solid solution hardening is proportional to the parameter ${\varepsilon_i^b}^{4/3}$. The parameter of atomic size misfit ε_i^b is calculated with the interatomic spacing associated with the cell parameters [128]. The calculation of this parameter ε_i^b is complicated due to the chemical complexity and lattice distortion in the HEAs. The size misfit can also be evaluated by the differences of the atomic radius among the constituents according to the equation 2.4. In this study, the atomic size effect was considered, determined based on the atomic size misfit δ including the solute concentration as discussed previously. To simplify the effect of atomic size misfit on the solid solution hardness, the correlation between the solid solution hardening and the parameter $\delta^{4/3}$ was made, as shown in

Figure 6.20. The parameter *ΔHV* is the hardness difference between the hardness of the alloys and the hardness of unary samples (Ni for *fcc* samples and Nb for *bcc* samples).

Figure 6.20 (a) presents the correlation for the *bcc*-structured samples, which combines the hardness values of as-homogenized equiatomic *bcc* samples in previous sections and non-equiatomic *bcc* samples in this section. The increase in the hardness of the *bcc*-structure solid solution samples was caused by larger atomic size misfit of the composition. This correlation is supported by good linear fit with slight scattering. It can suggest that the solid solution hardening in the *bcc*-structured HEAs is correlated to the atomic size misfit. For the *fcc*-structured sample, the hardness of as-homogenized equiatomic *fcc* samples is plotted in the correlation with the parameter $\delta^{4/3}$, as presented in Figure 6.20 (b). The all marks are located at the low values of the parameter $\delta^{4/3}$, showing a good agreement with a linear fit. It is mentioned that the slopes of the linear fit for the *bcc* and *fcc* samples are similar. It can suggest that the level of solid solution hardening can be enhanced by enlarging the magnitude of atomic size misfit in the *fcc* HEAs. Due to the narrow range of the parameter $\delta^{4/3}$ associated with the slight atomic size differences, the correlation for the solid solution hardening in the *fcc* samples is limited. However, the experimental results suggest that the atomic size misfit has an influence on the solid solution hardening, at least, in the *bcc*-structured HEAs.

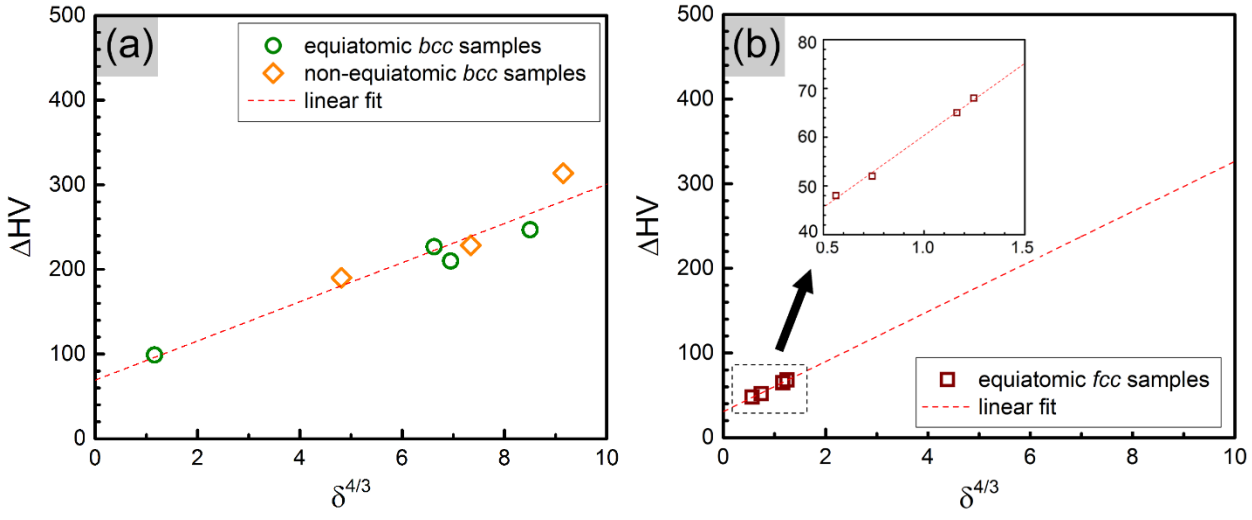

Figure 6.20 Correlation between microhardness and $\delta^{4/3}$ for (a) the *bcc*-structured samples and (b) the *fcc*-structured samples.

7. Work hardening in single phase high entropy alloys

Work hardening is commonly observed in plastic deformation of materials, which especially improves the strength. Cold rotary swaging was employed in this study to deform the samples. The rotary swaging facilitates an accumulation of high plastic strain due to delayed fracture associated with large hydrostatic stresses [17]. The hardness and compressive yield strength have been measured for evaluating the work hardening in the *fcc*-structured FeNiCoCrMn and the *bcc*-structured TiNbHfTaZr HEAs. This chapter also discusses the effects of degree of deformation and dislocation density on the mechanical properties of the HEAs.

7.1 Work hardenability of *fcc*- and *bcc*-structured high entropy alloys

The as-homogenized *fcc*-structured FeNiCoCrMn HEA rods with approximately 5.5 mm diameter after removing contaminated surface were swaged by approximately 45, 70 and 85 % reduction of cross-section area into 4.0, 3.0 and 2.0 mm diameter rods, respectively. Similarly, the as-homogenized *bcc*-structured TiNbHfTaZr HEA rods were swaged by 80 % and 90 % reduction of cross-section area into 2.5 and 1.7 mm diameter rods, respectively. The both HEAs indicated high deformability without cracking after the highest degree of cold deformation.

Figure 7.1 shows the effects of degree of deformation on hardness and compressive yield strength of the FeNiCoCrMn and TiNbHfTaZr HEAs. For the compression test, all the samples were compressed until 20 % of strain and no fracture evidence was observed during the test. It was reported that the FeNiCoCrMn HEA is ductile because of dislocation pile-ups, dislocation motion and deformation nanotwin [1, 156]. In addition, O.N. Senkov et al. [14] suggests that the good deformability of TiNbHfTaZr HEA is probably due to simultaneous dislocation and deformation twinning. Hardness and compressive yield strength for the two HEAs increase with an increase in the degree of deformation, as observed in Figure 7.1. The higher degree of cold working elongates grains and generates the number of dislocation, which increases the amount of barriers for

dislocation motions [136]. It can be also observed that work hardenability and strengthening abilities of the *fcc* FeNiCoCrMn HEA were larger than those of the *bcc* TiNbHfTaZr HEA. The TiNbHfTaZr HEA shows an insignificant change in the hardness and compressive yield strength during an increase in the degree of deformation.

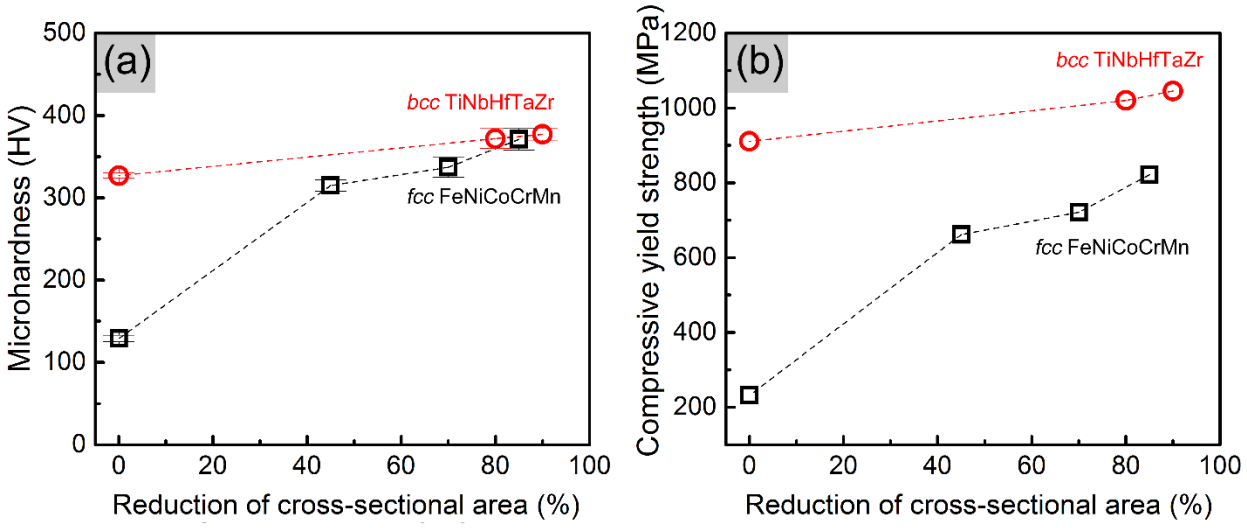

Figure 7.1 Effect of degree of cold working on (a) hardness and (b) compressive yield strength of *fcc*-structured FeNiCoCrMn HEA and *bcc*-structured TiNbHfTaZr HEA.

For the *fcc*-structured FeNiCoCrMn HEA, the hardness and compressive yield strength increased significantly at the 45 % of cold working beginning of cold swaging, but afterward the degree of hardening was lower. After the highest degree of cold working (85 %), the hardness and compressive yield strength significantly reached 367 HV and 821 MPa, respectively. They were approximately three times higher than the values of undeformed sample. The FeNiCoCrMn HEA has low stacking fault energy (18 - 30 mJ/m^2) [134, 157]. It was reported that stacking faults are frequently observed after small plastic deformation; for example at 2.1 % strain at room temperature [16]. Low stacking fault energy results in more difficult dislocation cross-slip and thus delay dynamic recovery [1, 158]. The deformation-induced nanotwinning was also reported in the FeNiCoCrMn at room temperature [16, 20, 134, 159, 160]. S-W Kim et al. [145] also reported the

deformation twins were immediately occurred during tensile straining on as-thermomechanically treated FeNiCoCrMn HEA. The twin boundaries retard the dislocation motion and moving across the boundaries, and thus result in dislocation pile-ups. These mechanisms are evident to cause the large work hardenability in the FeNiCoCrMn HEA.

The hardness and yield strength of the TiNbHfTaZr HEA slightly increased with an increase in the degree of deformation. The values of the hardness and strength after deformation with the highest degree of area reduction (90%) were 377 HV and 1046 MPa, respectively. These values were not largely different from those of undeformed samples (327 HV of hardness, 985 MPa of yield strength). The TiNbHfTaZr HEA is assumed to have high stacking fault energies due to high stacking fault energies of each constituent element (Ti, Nb, Hf, Ta and Zr). In the alloys with a high SFE, dynamic recovery is favored due to the dislocation cross slip under the deformation process [125, 136]. J.-P. Couzinié et al. [161] observed numerous dislocation debris in substructures of the TiNbHfTaZr sample after compression test. It is a consequence of the screw dislocation motions and ability to cross slip. J.-P. Couzinié et al. [161] also suggests that the dislocation activity during plastic deformation of the TiNbHfTaZr HEA is similar to *bcc* pure metals (i.e. Ta- or Nb-based alloys). Therefore, it can be assumed that the small work hardenability of the TiNbHfTaZr HEA is possibly resulted by high degree of solid solution hardening, ease to cross slip and less twin deformation.

7.2 Dislocation density of *fcc*- and *bcc*-structured high entropy alloys after cold swaging

Dislocation density of fcc- structured FeNiCoCrMn high entropy alloy after cold swaging

For determining dislocation density in the *fcc*-structured samples, the as-swaged rods after the 85% reduction of the cross-sectional area were examined by Williamson-Hall method on synchrotron high energy X-ray diffraction patterns of Figure 7.2. The XRD patterns show the single *fcc*-structured phase for all samples after the 85% area reduction. Williamson-Hall plot as given in Figure 7.3 was used to calculate the dislocation density of the as-swaged *fcc*-structured

samples [99, 100, 162]. The Williamson-Hall plot was made by the data from the synchrotron X-ray diffraction patterns as explained in the chapter 3. The micro lattice strain (ε_{str}) was derived from the slope of the linear fitting, as presented in Table 7.1. The values of the lattice strain were adopted to evaluate the dislocation density (ρ) for *fcc* materials with Burgers vector along <110> using the following equation proposed by Williamson and Smallman [163]:

$$\rho = 16.1 \frac{\varepsilon^2}{b^2} \tag{7.1}$$

where ε is lattice strain and b is the magnitude of Burgers vector. In the FeNiCoCrMn HEA, there is a report that deformation occurs by planar dislocation glide on the normal *fcc* slip system, {111}<110> [16]. The magnitude of the Burgers vector is calculated using the <110> slip direction.

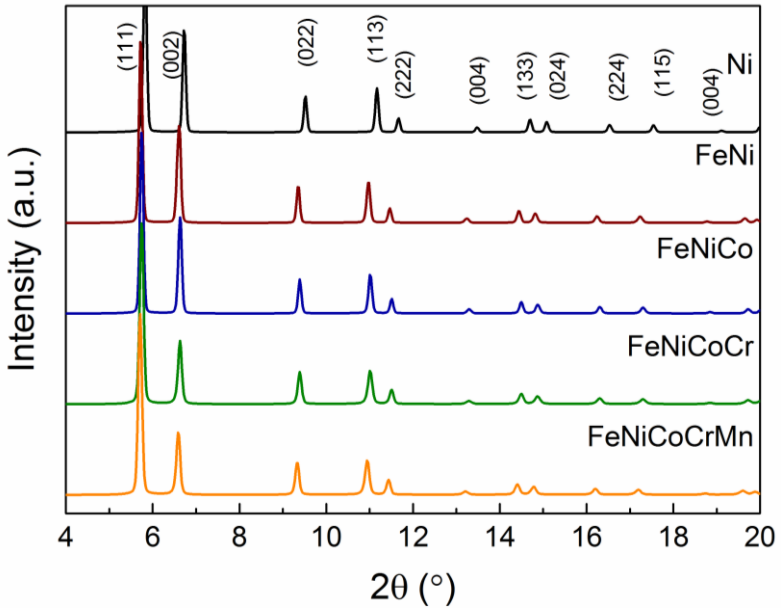

Figure 7.2 High energy synchrotron X-ray diffraction patterns of the *fcc*-structured samples after 85% reduction of the cross-sectional area.

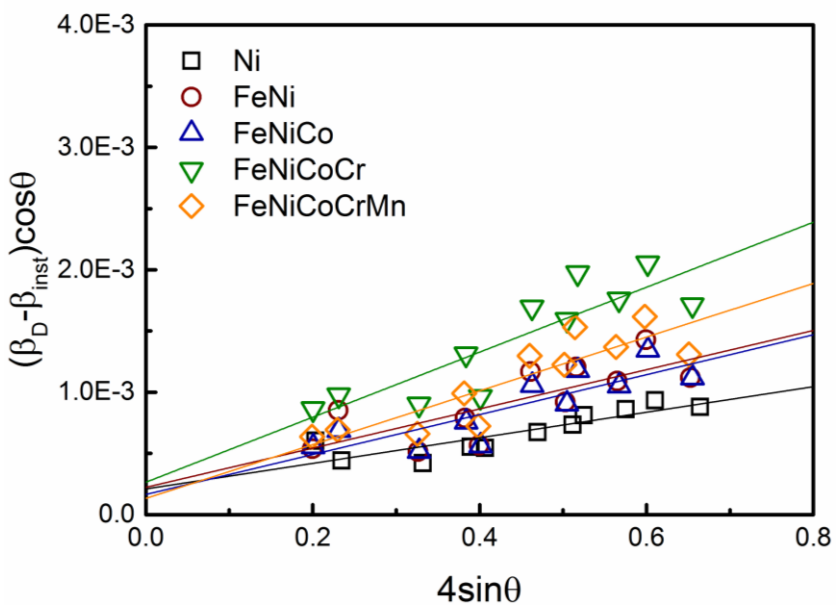

Figure 7.3 Williamson-Hall plots of the *fcc*-structured samples after 85% reduction of the cross-sectional area.

The dislocation densities of the samples after 85% reduction of the cross-sectional area were calculated as shown in Figure 7.4 and Table 7.1. The dislocation densities of the Ni, FeNi, FeNiCo, FeNiCoCr and FeNiCoCrMn samples are 2.8 x 10^{14}, 6.4 x 10^{14}, 6.7 x 10^{14}, 17.8 x 10^{14} and 12.0 x 10^{14} m^{-2}, respectively. The stored dislocation densities of the samples after cold working are in the range of 10^{14} - 10^{15} m^{-2}. In general, dislocation density of pure metals and conventional alloys is in a range of 10^{10} - 10^{12} m^{-2} at typical homogenized state, and can increase up to 10^{15} - 10^{16} m^{-2}, depending on the level of applied plastic deformation [163, 164]. The dislocation density of the as-swaged Ni in this study was examined as 2.8 x 10^{14} m^{-2}, similar to a reported magnitude of the Ni after severely deformed by accumulative roll bonding (ARB) (3 x 10^{14} m^{-2}) [165]. The dislocation densities of the FeNiCoCrMn HEA and its sub-alloys are within this range of the reported values, which supports the reliability of the current calculation. The dislocation density increases with the number of constituent elements, as shown in Figure 7.4. This could be due to the fact that the addition of a alloying elements (solid solution effect) to pure metals is effective to increase the dislocation density during deformation [163]. The presence of multiple atoms possibly produces strong barriers for dislocation motion. The strong inhibition of dislocation motion

reduces the dislocation recovery and grain boundary migration, and thus facilitates dislocation accumulation [164, 166]. Besides the number of constituent elements, the lattice distortion created by the random distribution of multiple principle elements in HEAs is often assumed to be an obstacle for dislocation motion and to affect the dislocation storage in HEAs. However, the experimental investigations in chapter 5 revealed that the level of the lattice distortion in the FeNiCoCrMn HEA was similar to those of the sub-alloys including Ni sample. Therefore, the role of the lattice distortion in the FeNiCoCrMn HEA is not expected to have a dominant effect on dislocation storage.

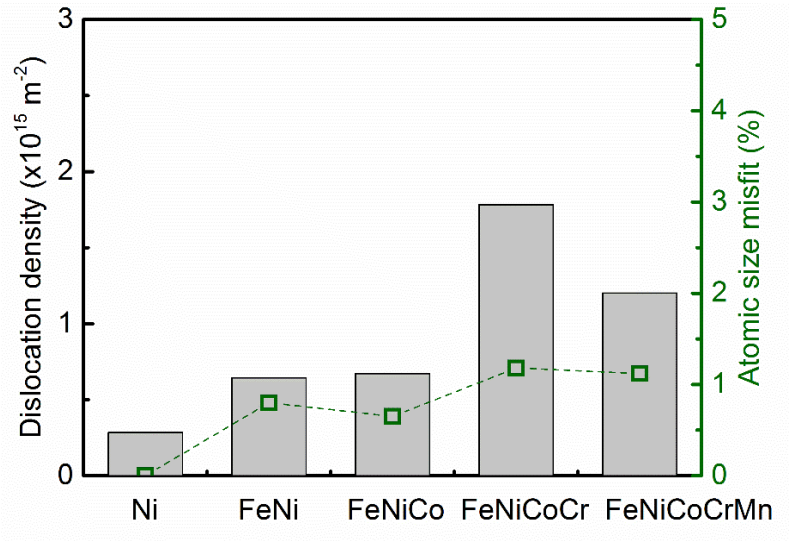

Figure 7.4 Dislocation density stored in the *fcc*-structured samples after 85% reduction of the cross-sectional area and the atomic size misfit of the samples.

Table 7.1 Lattice parameters (a), magnitudes of Burgers vector (b) along <110>, lattice strain (ε) and dislocation density (ρ) of the *fcc*-structured samples after 85% reduction of the cross-sectional area and stacking fault energy of the alloys (γ)

Alloys	a (Å)	b (Å)	ε (%)	ρ (x 10^{15} m^{-2})	γ (mJ/m^2)
Ni	3.5210	2.4897	0.104	0.28	120 - 130 [132]
FeNi	3.5834	2.5339	0.160	0.64	79 [133]
FeNiCo	3.5695	2.5240	0.163	0.67	31 [1]
FeNiCoCr	3.5709	2.5250	0.266	1.78	25 [1]
FeNiCoCrMn	3.5931	2.5407	0.220	1.20	18 - 27 [134, 167]

There have been experimental and theoretical studies which relates the stacking fault energy (SFE) to the dislocation density, cell size and flow stress [168, 169, 170]. According to these studies, a reduction of the SFE increases the total dislocation density and the flow stress, and promotes the splitting of a dislocation, which leads to the suppression of recombining the dissociated dislocations and annihilating the dislocations by cross-slip [126, 168]. The SFE of materials can be controlled by alloying elements [171]. Many studies reported the effects of alloying elements to Ni-based alloys on SFE. For example, the additions of Fe and Cr to Ni-based alloys generally decrease the SFE, while the addition of Cr up to 25 wt% reduces the SFE to 40 and 45 mJ/m^2 [172]. Meanwhile, the addition of Fe between 2.5 and 12.5 wt% results in an average SFE value of 86 mJ/m^2 [70, 173]. Based on the previous experimental and theoretical investigations, the SFE of the alloys in the present study are obtained [1, 132, 134]; 120 - 130 mJ/m^2 of pure Ni [132], 79 mJ/m^2 of FeNi [133], 31 mJ/m^2 of FeNiCo [1], 25 mJ/m^2 of FeNiCoCr [1] and 18 - 27 mJ/m^2 of the FeNiCoCrMn HEA [134, 167].

It can be seen that the FeNiCoCrMn HEA has the relatively low SFE among these studied samples. Based on the previous study, it is believed that the remarkably higher dislocation density of the FeNiCoCrMn HEA (~ 1.20 x 10^{15} m^{-2}) is influenced by the SFE effect. However, it is lower than the dislocation density in the quaternary FeNiCoCr alloy as 1.78 x 10^{15} m^{-2}. The melting points of Ni, FeNi, FeNiCo and FeNiCoCr are in narrow range between 1693 - 1728 K, while that

of the FeNiCoCrMn HEA is 1562 K. The relative lower melting point relates to increase its homologous temperature of the deformation that allows thermal energy more available. It possibly promoted more chance of a dislocation being able to overcome the lattice resistance and decreased dislocation storage.

Figure 7.5 presents the correlation between dislocation density, hardness and compressive yield strength as a function of constituent elements for the *fcc*-structured samples after 85% reduction of the cross-sectional area. The changes in the hardness and the compressive yield strength were followed by the level of dislocation density among the samples. The higher level of dislocation density produces stronger barriers for the dislocation motions. The FeNiCoCr alloy, which obtained the highest dislocation density, presented the highest hardness (403 HV) and compressive yield strength (933 MPa). The FeNiCoCrMn HEA with the most chemical complexity HEA was expected to exhibit the best mechanical properties but it showed lower hardness (367 HV) and yield strength (821 MPa) possibly due to its lower dislocation storage.

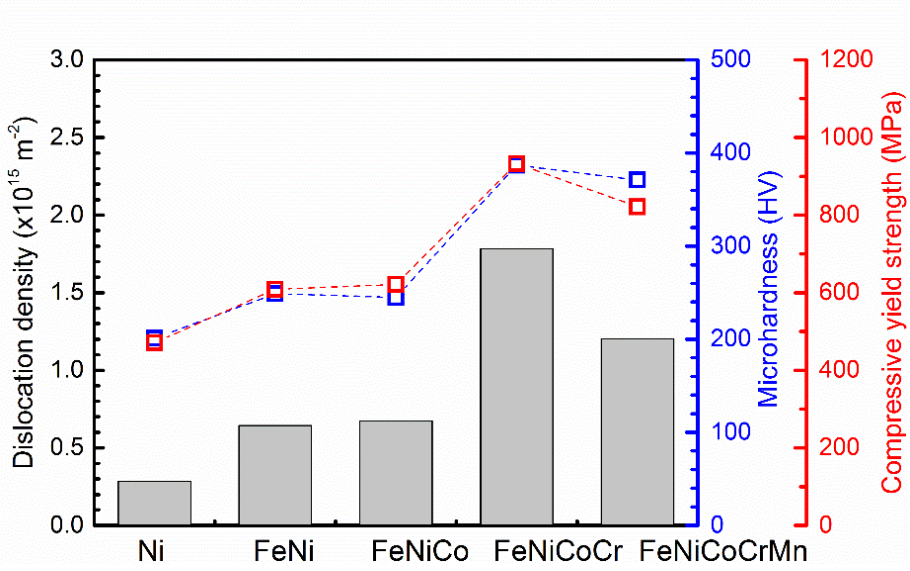

Figure 7.5 Dislocation density, hardness and compressive yield strength for the *fcc*-structured samples after 85% reduction of the cross-sectional area

Table 7.2 Hardness and compressive yield strength ($\sigma_{0.2}$) after 85% reduction of the cross-sectional area and shear modulus (G) calculated by the rule of mixture with the data from the reference [108].

Alloys	Hardness (HV)	$\sigma_{0.2}$ (MPa)	G (GPa)
Ni	201	471	76
FeNi	249	609	78
FeNiCo	245	621	77
FeNiCoCr	403	933	87
FeNiCoCrMn	367	821	84

In general, an increase in flow stress due to interaction with forest dislocation is expressed by the following Taylor relationship [174].

$$\tau = \tau_0 + \alpha G b \sqrt{\rho} \tag{7.2}$$

where τ is the shear strength, τ_0 is the intrinsic shear strength, α is a constant describing the average interactions between dislocations dependent on the alloy, b is the magnitude of Burgers vector and G is the shear modulus of materials. The shear strength can be converted to yield stress with Taylor factor *(M)* as shown in the following equation.

$$\tau = \frac{\sigma}{M} \tag{7.3}$$

The Taylor factor (M) is approximately 3.06 for typical *fcc*-structured polycrystalline materials with the <110> slip direction [126]. The equation 7.2 can be derived from a series of different interaction mechanisms (i.e. cutting of forest dislocations) and related to the mean dislocation density [175]. This relationship explains a hardening behavior under the plastic deformation for one material. However, the attempt to predict the plastic deformation behaviors of the single phase *fcc*-structured solid solution samples were made by the equation 7.2, as presented in Figures 7.6. The data points are in a good agreement with a linear fit. It suggests that the behavior of work hardening in the *fcc*-structured FeNiCoCrMn HEA is similar to those of its sub-alloys. The linear fit cuts a y-intercept at $\sigma/M \sim 48$ MPa; it is equivalent to $\sigma_0 \sim 146$ MPa. This

value indicates the property before plastic deformation, in the range of the yield strength between the as-annealed *fcc* HEA and its sub-alloys as discussed in chapter 6. The slope of the fit line is equivalent to the value of the term of αGb. In this study, the data points on the plot were interpreted from the different composition; hence, the extraction of the value of α was done by the average shear modulus G (80.40 GPa) and Burgers vector b (2.523 Å). The value of α in this work was calculated as approximately 0.3. The α values is dependent on many factors; i.e. deformation mode, deformation rate, temperature, dislocation distribution, crystal orientation, alloying [176]. For metals, the α value is in the range of 0.3 - 0.5 [177]. In particular, the treatment for general *fcc* metals uses $\alpha \sim 0.3$ for modeling work hardening behavior [178]. The dislocation interaction of the FeNiCoCrMn HEA and its sub-alloys was in a reasonable agreement with those of conventional *fcc* metals.

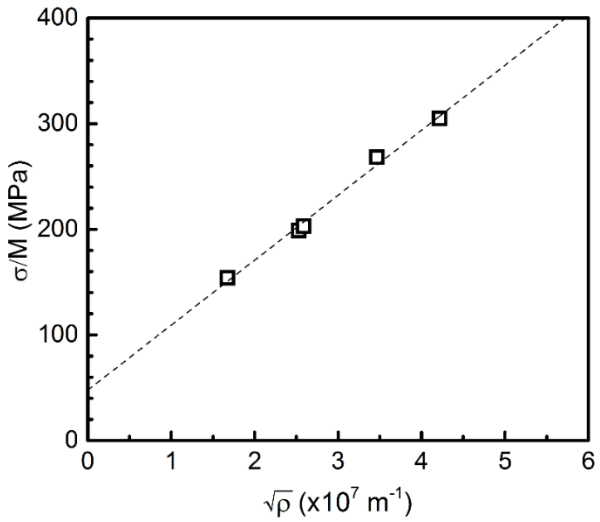

Figure 7.6 Taylor relationship of work hardening between σ/M and $\sqrt{\rho}$ for the *fcc*-structured alloys after 85% reduction of the cross-sectional area.

Dislocation density of the bcc-structured TiNbHfTaZr high entropy alloy after cold swaging

The TiNbHfTaZr, TiNbHfTa, TiNbHf and TiNb samples after 90% reduction of the cross-sectional area and as-received 2 mm diameter Nb rod were used for examination of dislocation density in correlation with their hardness and compressive yield strength. All the samples were cold-swaged continuously without intermediate annealing. The TiNbHfTaZr HEA presented superior cold plasticity with 90% reduction of the cross-sectional area. The integral breath and 2θ of the *bcc*-structured solid solution peaks taken from XRD patterns of Figure 7.7 were used to be calculated for the Williamson-Hall plots as given in Figure 7.8. The slopes represented the lattice strain as given in Table 7.3. The dislocation density for the *bcc*-structured materials was calculated by the following equation [163].

$$\rho = 14.4 \frac{\varepsilon^2}{b^2} \tag{7.4}$$

where b is Burgers vector along <111>. A previous investigation in the TiNbHfTaZr HEA suggested that plastic deformation at room temperature is governed by the motion of screw dislocation with b = a/2 <111> Burgers vector [161].

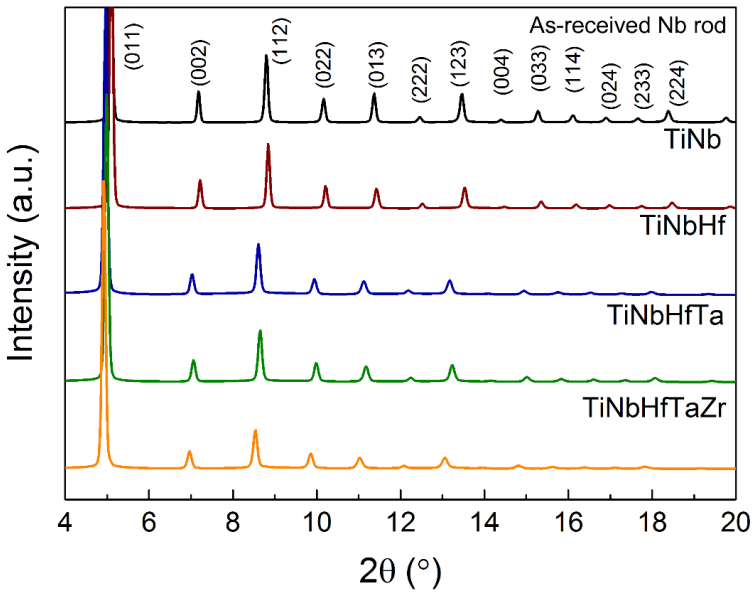

Figure 7.7 High energy synchrotron X-ray diffraction patterns of the *bcc*-structured samples after 90% reduction of the cross-sectional area including as-received Nb rod.

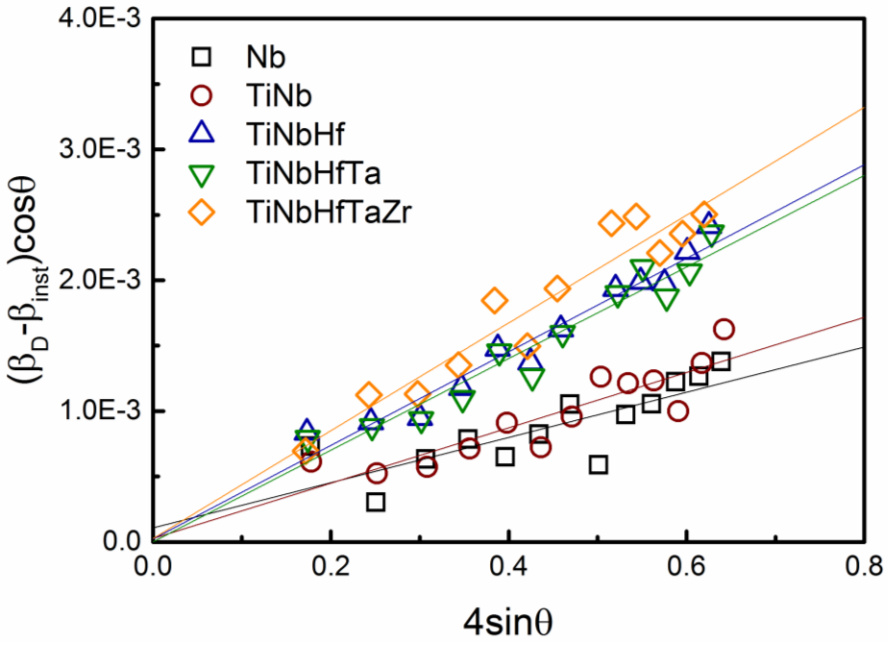

Figure 7.8 Williamson-Hall plots of the *bcc*-structured samples after 90% reduction of the cross-sectional area.

Table 7.3 Lattice parameters (a), magnitudes of Burgers vector (b) along <111>, lattice strain (ε) and dislocation density (ρ) of the *bcc*-structured samples after 90% reduction of the cross-sectional area.

Alloys	a (Å)	b (Å)	ε (%)	ρ (x 10^{15} m^{-2})
Nb*	3.298	2.856	0.170	0.510
TiNb	3.281	2.842	0.211	0.794
TiNbHf	3.370	2.918	0.358	2.167
TiNbHfTa	3.355	2.906	0.350	2.089
TiNbHfTaZr	3.398	2.942	0.412	2.823

*as-received 2 mm diameter rod

The dislocation densities of the as-swaged *bcc*-structured samples were listed in Table 7.3 and schematically showed in the bar chart of Figure 7.9. The calculated magnitudes of dislocation density were between 0.510 - 2.823 x 10^{15} m^{-2}, comparable to the range for conventional heavily

deformed materials [163, 164]. The dislocation density for the *bcc*-structured samples was higher than the *fcc*-structured sample. From equation 7.1 and 7.4, the dislocation density is proportional to the lattice strain. The larger lattice strain of the *bcc*-structured samples was possibly resulted by large atomic size misfit. On the other hand, the energy necessary to create dense distributions of dislocations is related to the elastic energy [179]. The elastic energy of *bcc*-structure is normally higher than that of *fcc*-structure due to more difficult to slip. Also the higher melting points of the *bcc*-structured samples have higher stored energy, which require more energy for plastic deformation. Strictly speaking, the dislocation density between *fcc* and *bcc* samples could not perfectly be compared due to different degree of deformation. The *bcc*- structured samples were deformed with higher degree of reduction than the *fcc*-structured samples; hence it could contribute to the higher magnitudes of dislocation density.

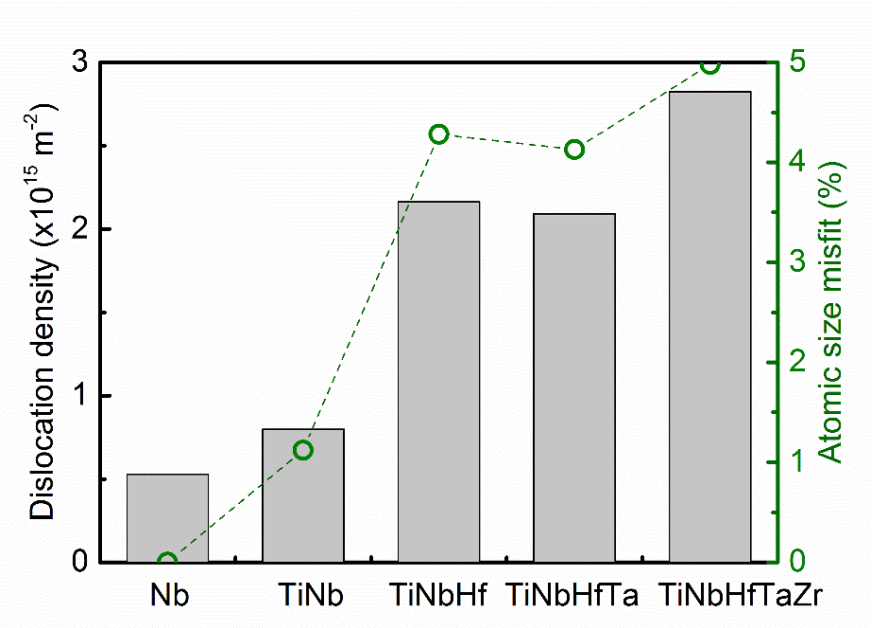

Figure 7.9 Dislocation density stored in the as-swaged *bcc*-structured samples after 90% reduction of the cross-sectional area and the atomic size misfit of the samples.

The stacking fault energy (SFE) for the most *bcc* alloys is unknown. The SFEs of Nb [180], Ti [181], Ta [181] and Zr [136] are reported as approximately 200, 320, 480 and 240 mJ/m^2, respectively. The SFEs of the studied *bcc*-structured are assumed to be high. Hence, the

TiNbHfTaZr HEA and its sub-alloys can be categorized as high SFE materials. With high stacking fault energy, the screw dislocations may cross-slip to accommodate deformation [182]. In literatures, the deformation twin is less found in *bcc* HEAs [1]. Less deformation twinning suggests difficult deformation and increases dislocation density storage. The plastic deformation of general *bcc* materials at low temperature is controlled by thermally activated motion of screw dislocations [183], leading to dislocation cross-slip for both generation [184] and annihilation [185]. Among the *bcc*-structured samples, their melting points are high between 2346 – 2750 K and they lead to remarkably low homologous temperatures (0.10 - 0.13) of deformed samples at room temperature. As the result, the thermal energies for every samples could be assumed to be same. The levels of dislocation density can be compared between the samples in terms of intrinsic lattice resistance and lattice structure.

The TiNbHfTaZr HEA obtained the highest dislocation density, followed by TiNbHf, TiNbHfTa, TiNb and as-received 2 mm Nb rod. It is claimed that the deformation of the *bcc* metals is affected by the interaction between the dislocations and solute atoms [183]. Figure 7.9 presents the strong correlation between the magnitude of dislocation density and the atomic size misfit. The large atomic size misfit caused the significant lattice distortion, as given evidence in chapter 5. The large atomic size misfit is possible to produces extensive stress field as strong obstacles to further dislocation motion [166, 186]. It leads to more chance for accumulation of high dislocation density. It was obvious that the dislocation densities for TiNbHf, TiNbHfTa and TiNbHfTaZr were higher than those of TiNb and Nb due to their relatively high atomic size misfits. As it is expected, bigger atoms, Hf and Zr, produce more local strains and cause a strong barrier for dislocation movement. The TiNbHfTaZr HEA, having the most chemical complexity and large atomic size misfit, demonstrated the high level of dislocation density. This suggested that the atomic size misfit and the large chemical complexity have a cooperative effect on dislocation density for the *bcc*-structured samples.

Figure 7.10 shows the dislocation density, hardness and compressive yield strength for the *bcc*-structured sample after 90% reduction of the cross-sectional area and the values for the mechanical properties are summarized in Table 7.4. The increases in hardness and compressive yield strength were observed between TiNb and TiNbHfTa, which their dislocation densities were greatly different. Although, the dislocation density of TiNbHfTa was slightly lower than that of

TiNbHf, the hardness and the compressive yield strength were higher. Moreover, the equation 7.2 suggests that the interaction between dislocations and shear modulus correlate to the shear strength of as-deformed samples. The shear modulus of Ta is 69 GPa, relatively higher than those of other elements between 30 – 40 GPa [43]. The interactions between Ta and other atoms may cause a larger deviation in the local forces than the other elements. The higher hardness and yield strength might be resulted by the higher shear modulus of TiNbHfTa. The TiNbHfTaZr HEA presented significantly high dislocation density, but the hardness and the yield strength were comparable to those of the TiNbHfTa. It could be contributed by lower shear modulus.

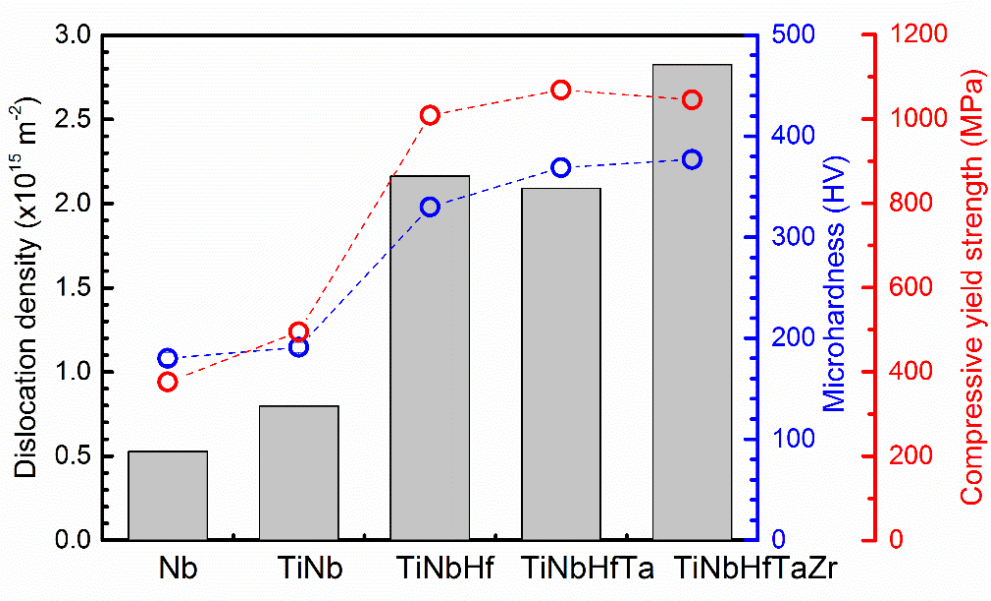

Figure 7.10 Dislocation density, hardness and compressive yield strength for the *bcc*-structured samples 90% reduction of the cross-sectional area.

Table 7.4 Hardness and compressive yield strength ($\sigma_{0.2}$) after 90% reduction of the cross-sectional area and shear modulus (G) calculated by the rule of mixture with the data from the reference [108].

Alloys	Hardness (HV)	$\sigma_{0.2}$ (MPa)	G (GPa)
Nb*	180	376	38
TiNb	191	495	41
TiNbHf	330	1009	37
TiNbHfTa	369	1069	45
TiNbHfTaZr	377	1046	43

*as-received 2 mm diameter rod

Figure 7.11 presents the relationship between σ/M and $\sqrt{\rho}$ for the as-swaged *bcc*-structured alloys according to the Taylor hardening model of the equation 7.2. The Taylor factor (M), 2.754, was used in this calculation for mixed slip modes in a <111> direction [187]. In *bcc* metals, slip is complex; however, the numerous experiments indicate that slip occurs in the closet packed <111> direction. In Figure 7.11, it shows a linear fit with some scatter. It is mentioned that the y-intercept is at σ/M (or τ_0) ~-65 MPa. The negative y-intercept suggests that the behaviors of work hardening in the TiNbHfTaZr HEA might be different from those of it sub-alloys. The term of τ_0 can be defined as the shear resistance to dislocation motion in the absence of dislocation interactions [188]. According to the investigation in the chapter 5, the levels of lattice strain for the TiNbHfTaZr HEA and its sub-alloys were significantly varied and the yield strength of as-annealed state, where external stress was removed, were in the wide range between 207 – 985 MPa. It indicates that the behavior of work hardening for the TiNbHfTaZr and its sub-alloys were possibly different due to their different lattice resistances. In addition, the α term, extracted from the slope of the linear fit in Figure 7.11, is approximately 0.8. This value is beyond the range for most metals between 0.3 – 0.5 [177]. G. Dirras et al. [189] reports $\alpha \sim 0.16$ for a plastic deformation of TiNbHfTaZr HEA, whereas the polycrystals of niobium is found with $\alpha \sim 0.47$ [176]. This suggests that the dislocation interaction in term of α for the TiNbHfTaZr might not be

similar to that of conventional *bcc* metals and, hence, the work hardening behavior is possibly not in an agreement with that of its sub-alloys and conventional alloys.

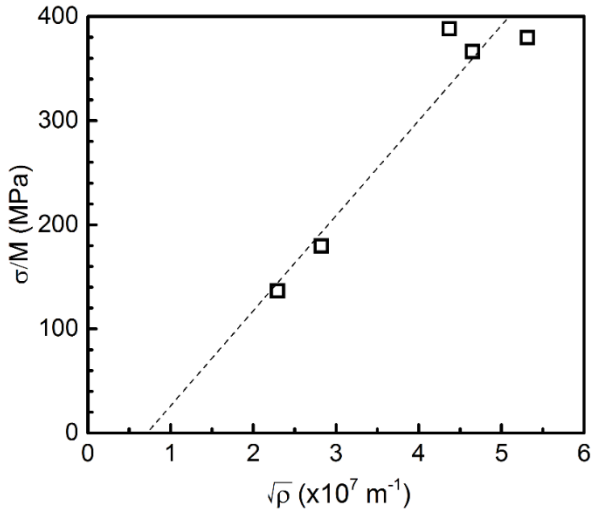

Figure 7.11 Taylor relationship of work hardening between σ/M and $\sqrt{\rho}$ for the *bcc*-structured alloys after 90% reduction of the cross-sectional area.

8. Summary and outlook

In this thesis, the interactions of multiple constituent elements in the single solid solution phase FeNiCoCrMn and TiNbHfTaZr high entropy alloys (HEAs) were mainly investigated in terms of the effects on microstructure, lattice strain and mechanical properties. The main points can be summarized below and the possible directions are suggested at the end of this chapter.

8.1 Summary

The equiatomic *fcc*-structured FeNiCoCrMn and *bcc*-structured TiNbHfTaZr HEAs were prepared by arc-melting, cold-crucible casting and thermomechanical treatment in order to study phase stability, intrinsic lattice strain, solid solution hardening and work hardening. The sub-alloys consisting of less number of constituent elements (*fcc*: equiatomic FeNiCoCr, FeNiCo, FeNi alloys and pure Ni / *bcc*: equiatomic TiNbHfTa, TiNbHf, TiNb alloys and pure Nb) were selected to be investigated in a comparison with the HEAs. The summary of each study in the HEAs was written in the following paragraphs.

Phase stability: The FeNiCoCrMn HEA, its sub-alloys (FeNiCoCr, FeNiCo, FeNi) and pure Ni sample obtained a single *fcc*-structured solid solution phase after homogenization. The DSC traces of the *fcc*-structured samples demonstrated phase stability and no phase transformation between 300 - 1500 K. This temperature range covers the temperature for the heat treatment in this work. Similarly, the as-homogenized TiNbHfTaZr HEA, its sub-alloys (TiNbHfTa, TiNbHf, TiNb) and pure Nb sample demonstrated a single *bcc*-structured solid solution phase and phase stability within that range of temperature. In aspect of thermodynamic, all studied samples obtain close to zero values of the mixing enthalpy and different values of the configurational entropy. This indicates that the mixing enthalpy is an important parameter to determine the formation of solid solution phase.

Lattice strain: The intrinsic lattice strain associated with the multiple atom species in the HEAs was examined in both micro and local scales by high energy synchrotron XRD. The micro

lattice strain in the HEAs and their sub-alloys was quantified by Williamson-Hall methods on the Bragg intensities. Although it was observed that larger micro lattice strain in the *fcc* FeNiCoCrMn and the *bcc* TiNbHfTaZr HEAs, but the levels of micro lattice strain were not significantly different among the samples having different number of constituent elements. The level of micro lattice strain were not clearly large to determine the atomic displacement. It is supported by the literature review that the crystallographic information on Bragg intensities demonstrates only the average bond distance and the lattice parameter. The pair distribution function (PDF) method was used to assess local lattice strain associated with the random arrangement of the multiple atom species in the HEAs. The small PDF peak widths of the FeNiCoCrMn HEA and its sub-alloys represented slight levels of local lattice strain affected by the small atomic size misfits. The atomic sizes of constituent elements in the FeNiCoCrMn HEA is not significantly different; hence, the local lattice strain was not anomalously large. In contrast, the PDF peaks of the TiNbHfTaZr HEA were broadened when compared with the peak widths of Nb and its sub-alloys. The large atomic size misfit in the TiNbHfTaZr HEA is assumed to cause the large local lattice strain. The evidence from this study suggests that the atomic size misfit is more important factor than the number of constituent elements in the determination of lattice distortion.

Solid solution hardening: For the single *fcc*-structured samples, the increase in the number of constituent elements from the unary Ni sample to the quinary FeNiCoCrMn HEA resulted in slight changes of hardness (64 – 132 HV) and tensile yield strength (60 – 192 MPa). On the contrary to the *fcc*-structured alloy system, the hardness and the yield strength of the *bcc*-structured alloy significantly increased with the number of constituent from the Nb sample to the TiNbHfTaZr HEA, between 80 – 327 HV of hardness and between 207 – 985 MPa of tensile yield strength. The lattice distortion in the *bcc*-structured alloy system was more pronounced than in the *fcc*-structured alloy system. The results suggest that the level of solid solution hardening is related to the level of lattice strain (lattice distortion) rather than the chemical complexity. The increase in atomic size misfit increases the lattice strain; thus, the large atomic size misfit is relative to enhancement of the solid solution hardening due to the strong elastic interaction between dislocations and atoms. The TiNbHfTaZr HEA presented larger level of solid solution hardening, than the FeNiCoCrMn HEA due to its large atomic size misfit.

Work hardening: The FeNiCoCrMn and TiNbHfTaZr HEAs including their sub-alloys were plastic deformed by the large degree of area reduction without intermediate annealing. The dislocation densities of the studied samples after the deformation were in the range between 10^{14} - 10^{15} m^{-2}. This range is consistent with reported levels for plastic deformed metals, which supports the reliability of this calculation. The increase in the number of constituent elements (solid solution effect) increased the accumulation of dislocation density during the cold working. Despite insignificant lattice distortion in the FeNiCoCrMn HEA and its sub-alloys, the dislocation storages after 85% reduction of the cross-sectional area were significantly different among the samples, followed by the level of atomic size misfit. For the *bcc*-structured alloys, the larger lattice distortion in the TiNbHfTaZr HEAs, the TiNbHfTa and the TiNbHf alloys were evident and significantly correlated with the higher dislocation densities after 90% reduction of the cross-sectional area, compared with the Nb and TiNb samples. The level of dislocation densities was correlated with the number of constituent elements, the level of lattice distortion associated with atomic size misfit and the intrinsic properties (i.e. the stacking fault energy and the melting point). Furthermore, it is expected that the higher dislocation densities of the FeNiCoCrMn and the TiNbHfTaZr HEAs are attributed to the enhanced solid solution effect. It is in a good agreement with the experimental results that the samples with higher level of dislocation density obtained higher hardness and compressive yield strength due to stronger interaction between dislocations. By applying the Taylor equation to describe the work hardening behavior, the result indicated that the FeNiCoCrMn showed similar dislocation interaction to Ni sample and its sub-alloys. However, the dislocation interaction of the TiNbHfTaZr HEA is likely to be different from the Nb sample and its sub-alloys. The work hardenability of the *fcc*-structured FeNiCoCrMn HEA is significant. The mechanical properties of as-deformed FeNiCoCrMn were significantly higher than the undeformed sample. The hardness and the yield strength of the *bcc*-structured TiNbHfTaZr HEA insignificantly increased by the reduction of cross-sectional area; the values were not significantly higher than those of the undeformed sample. The larger work hardenability of the FeNiCoCrMn HEA is believed to be as a result of relatively lower solid solution hardening and more ease of deformation twin.

8.2 Outlook

Based on the findings of this study, some aspects could be further investigated, as listed in the following points:

- As determined with the PDF method on the XRD patterns, the lattice strain in the *bcc* TiNbHfTaZr HEA was evident. Another method such as TEM should be made an attempt to demonstrate atomic arrangement for another evidence of lattice distortion.

- The experimental results demonstrated that the atomic size misfit had a great influence on the level of lattice strain and subsequently solid solution hardening. The investigation was made in the FeNiCoCrMn and TiNbHfTaZr HEAs and their sub-alloys. A study on other single solid solution phase HEA systems should be needed to emphasize this statement.

- In the sample preparation, the microstructural evolutions during annealing were different between the HEAs and their sub-alloys and pure metals. The microstructural behavior of the HEAs could be studied in a comparison with the sub-alloys.

- Due to single solid solution phase in the HEAs, the mechanical properties could modified within the limit of solid solution hardening. The other hardening mechanisms could be involved in the HEAs to enhance the mechanical properties. For example, the second phase precipitation, made by an addition of alloying element into single phase HEAs, can increase the strength and change the microstructural behavior.

References

[1] M.C. Gao, J.W. Yeh, P.K. Liaw, Y. Zhang, *High-entropy alloys: fundamentals and applications*, Springer Nature, Switzerland, (2016).

[2] B.S. Murty, J.W. Yeh, S. Ranganathan, *High-entropy alloys*, Butterworth-Heinemann, Boston, (2014).

[3] D.B. Miracle, O.N. Senkov; A critical review of high entropy alloys and related concepts, *Acta Mater.* 122 (2017) 448-511.

[4] Z.P. Lu, H. Wang, M.W. Chen, I. Baker, J.W. Yeh, C.T. Liu, T.G. Nieh; An assessment on the future development of high-entropy alloys: Summary from a recent workshop, *INTERMETALLICS* 66 (2015) 67-76.

[5] S. Guo, C. Ng, Z. Wang, C.T. Liu; Solid solutioning in equiatomic alloys: Limit set by topological instability, *J. Alloys Compd.* 583 (2014) 410-413.

[6] B. Cantor; Multicomponent and High Entropy Alloys, *Entropy* 16(9) (2014) 4749-4768.

[7] F.X. Zhang, S. Zhao, K. Jin, H. Xue, G. Velisa, H. Bei, R. Huang, J.Y.P. Ko, D.C. Pagan, J.C. Neuefeind, W.J. Weber, Y. Zhang; Local structure and short-range order in a NiCoCr solid solution alloy, *Phys. Rev. Lett.* 118(20) (2017) 205501-1-6.

[8] S. Billinge, M.F. Thorpe, *Local structure from diffraction*, Springer US (1998).

[9] A.S. Masadeh; Total scattering atomic pair distribution function: new methodology for nanostructure determination, *J. Exp. Nanosci.* 11(12) (2016) 951-974.

[10] P. Bordet; Local structure studies using the pair distribution function, *EPJ Web of Conferences* 104 (2015) 01003-1-14.

[11] J.-W. Yeh; Physical metallurgy of high-entropy alloys, *JOM* 67(10) (2015) 2254-2261.

[12] E.J. Pickering, N.G. Jones; High-entropy alloys: a critical assessment of their founding principles and future prospects, *Int. Mater. Rev.* 61(3) (2016) 183-202.

[13] H.Y. Diao, R. Feng, K.A. Dahmen, P.K. Liaw; Fundamental deformation behavior in high-entropy alloys: An overview, *Curr. Opin. Solid State Mater. Sci.* 21(5) (2017) 252-266.

[14] G. Laplanche, A. Kostka, C. Reinhart, J. Hunfeld, G. Eggeler, E.P. George; Reasons for the superior mechanical properties of medium-entropy CrCoNi compared to high-entropy CrMnFeCoNi, *Acta Mater.* 128 (2017) 292-303.

[15] W. Woo, E.W. Huang, J.-W. Yeh, H. Choo, C. Lee, S.-Y. Tu; In-situ neutron diffraction studies on high-temperature deformation behavior in a CoCrFeMnNi high entropy alloy, *INTERMETALLICS* 62 (2015) 1-6.

[16] F. Otto, A. Dlouhý, C. Somsen, H. Bei, G. Eggeler, E.P. George; The influences of temperature and microstructure on the tensile properties of a CoCrFeMnNi high-entropy alloy, *Acta Mater.* 61(15) (2013) 5743-5755.

[17] G. Laplanche, O. Horst, F. Otto, G. Eggeler, E.P. George; Microstructural evolution of a CoCrFeMnNi high-entropy alloy after swaging and annealing, *J. Alloys Compd.* 647 (2015) 548-557.

[18] R.R. Eleti, V. Raju, M. Veerasham, S.R. Reddy, P.P. Bhattacharjee; Influence of strain on the formation of cold-rolling and grain growth textures of an equiatomic HfZrTiTaNb refractory high entropy alloy, *Mater. Charact.* 136 (2018) 286-292.

[19] W. Wu, S. Ni, Y. Liu, M. Song; Effects of cold rolling and subsequent annealing on the microstructure of a HfNbTaTiZr high-entropy alloy, *J. Mater. Res.* 31(24) (2016) 3815-3823.

[20] A. Gali, E.P. George; Tensile properties of high- and medium-entropy alloys, *INTERMETALLICS* 39 (2013) 74-78.

[21] R. Kozak, A. Sologubenko, W. Steurer; Single-phase high-entropy alloys – an overview, *Z. Kristallogr. Cryst. Mater.* 230(1) (2015) 55-68.

[22] J.W. Yeh, S.K. Chen, S.J. Lin, J.Y. Gan, T.S. Chin, T.T. Shun, C.H. Tsau, S.Y. Chang; Nanostructured high-entropy alloys with multiple principal elements: Novel alloy design concepts and outcomes, *Adv. Eng. Mater.* 6(5) (2004) 299-303.

[23] B. Cantor, I.T.H. Chang, P. Knight, A.J.B. Vincent; Microstructural development in equiatomic multicomponent alloys, *Mater. Sci. Eng. A.* 375–377 (2004) 213-218.

[24] D.B. Miracle; Critical Assessment 14: High entropy alloys and their development as structural materials, *Mater. Sci. Technol.* 31(10) (2015) 1142-1147.

[25] Y. Zhang, T.T. Zuo, Z. Tang, M.C. Gao, K.A. Dahmen, P.K. Liaw, Z.P. Lu; Microstructures and properties of high-entropy alloys, *Prog. Mater Sci.* 61 (2014) 1-93.

[26] D.A. Porter, K.E. Easterling, *Phase Transformations in Metals and Alloys*, Taylor & Francis (1992).

[27] A. Takeuchi, A. Inoue; Quantitative evaluation of critical cooling rate for metallic glasses, *Mater. Sci. Eng. A.* 304-306 (2001) 446-451.

[28] Y. Zhang, Y.J. Zhou, J.P. Lin, G.L. Chen, P.K. Liaw; Solid-solution phase formation rules for multi-component alloys, *Adv. Eng. Mater.* 10(6) (2008) 534-538.

[29] A.R. Miedema, P.F. de Châtel, F.R. de Boer; Cohesion in alloys - fundamentals of a semi-empirical model, *Physica B* 100(1) (1980) 1-28.

[30] X. Yang, Y. Zhang; Prediction of high-entropy stabilized solid-solution in multi-component alloys, *Mater. Chem. Phys.* 132(2) (2012) 233-238.

[31] Z. Wang, S. Guo, C.T. Liu; Phase selection in high-entropy alloys: from nonequilibrium to equilibrium, *JOM* 66(10) (2014) 1966-1972.

[32] Z. Wang, Y. Huang, Y. Yang, J. Wang, C.T. Liu; Atomic-size effect and solid solubility of multicomponent alloys, *Scr. Mater.* 94 (2015) 28-31.

[33] W. Hume-Rothery; The sizes of atoms in metallic crystals, *Physica* 15(1) (1949) 29-33.

[34] Y. Zhang, X. Yang, P.K. Liaw; Alloy design and properties optimization of high-entropy alloys, *JOM* 64(7) (2012) 830-838.

[35] Y.F. Ye, Q. Wang, J. Lu, C.T. Liu, Y. Yang; High-entropy alloy: challenges and prospects, *Mater. Today* 19(6) (2016) 349-362.

[36] M.C. Gao, C. Zhang, P. Gao, F. Zhang, L.Z. Ouyang, M. Widom, J.A. Hawk; Thermodynamics of concentrated solid solution alloys, *Curr. Opin. Solid State Mater. Sci.* 21(5) (2017) 238-251.

[37] J.W. Yeh, Y.L. Chen, S.J. Lin, S.K. Chen; High-Entropy Alloys – A New Era of Exploitation, *Mater. Sci. Forum* 560 (2007) 1-9.

[38] F. Otto, Y. Yang, H. Bei, E.P. George; Relative effects of enthalpy and entropy on the phase stability of equiatomic high-entropy alloys, *Acta Mater.* 61(7) (2013) 2628-2638.

[39] B. Cantor, I.T.H. Chang, P. Knight, A.J.B. Vincent; Microstructural development in equiatomic multicomponent alloys, *Mater. Sci. Eng. A.* 375 (2004) 213-218.

[40] M.S. Lucas, G.B. Wilks, L. Mauger, J.A. Muñoz, O.N. Senkov, E. Michel, J. Horwath, S.L. Semiatin, M.B. Stone, D.L. Abernathy, E. Karapetrova; Absence of long-range chemical ordering in equimolar FeCoCrNi, *Appl. Phys. Lett.* 100(25) (2012) 251907-1-4.

[41] S.G. Ma, S.F. Zhang, M.C. Gao, P.K. Liaw, Y. Zhang; A successful synthesis of the CoCrFeNiAl0.3 single-crystal, high-entropy alloy by bridgman solidification, *JOM* 65(12) (2013) 1751-1758.

[42] J.Y. He, W.H. Liu, H. Wang, Y. Wu, X.J. Liu, T.G. Nieh, Z.P. Lu; Effects of Al addition on structural evolution and tensile properties of the FeCoNiCrMn high-entropy alloy system, *Acta Mater.* 62 (2014) 105-113.

[43] O.N. Senkov, J.M. Scott, S.V. Senkova, D.B. Miracle, C.F. Woodward; Microstructure and room temperature properties of a high-entropy TaNbHfZrTi alloy, *J. Alloys Compd.* 509(20) (2011) 6043-6048.

[44] M. Feuerbacher, M. Heidelmann, C. Thomas; Plastic deformation properties of Zr–Nb–Ti–Ta–Hf high-entropy alloys, *Philos. Mag.* 95(11) (2014) 1221-1232.

[45] Y.D. Wu, Y.H. Cai, X.H. Chen, T. Wang, J.J. Si, L. Wang, Y.D. Wang, X.D. Hui; Phase composition and solid solution strengthening effect in TiZrNbMoV high-entropy alloys, *Mater. Des.* 83 (2015) 651-660.

[46] O.N. Senkov, G.B. Wilks, D.B. Miracle, C.P. Chuang, P.K. Liaw; Refractory high-entropy alloys, *INTERMETALLICS* 18(9) (2010) 1758-1765.

[47] J.W. Christian, *The theory of transformations in metals and alloys*, Pergamon, Oxford, (2002).

[48] O.N. Senkov, G.B. Wilks, J.M. Scott, D.B. Miracle; Mechanical properties of Nb25Mo25Ta25W25 and V20Nb20Mo20Ta20W20 refractory high entropy alloys, *INTERMETALLICS* 19(5) (2011) 698-706.

[49] J.-W. Yeh; Recent progress in high-entropy alloys, *European Journal of Control* 31(6) (2006) 633-648.

[50] J.-W. Yeh, S.-J. Lin, T.-S. Chin, J.-Y. Gan, P.-H. Lee, T.-T. Shun, C.-H. Tsau, S.-Y. Chou; Formation of simple crystal structures in Cu-Co-Ni-Cr-Al-Fe-Ti-V alloys with multiprincipal metallic elements, *Metall. Mater. Trans. A* 35A (2004) 2533-2536.

[51] Y.J. Zhou, Y. Zhang, Y.L. Wang, G.L. Chen; Solid solution alloys of AlCoCrFeNiTix with excellent room-temperature mechanical properties, *Appl. Phys. Lett.* 90(18) (2007) 181904.

[52] H. Song, F. Tian, Q.-M. Hu, L. Vitos, Y. Wang, J. Shen, N. Chen; Local lattice distortion in high-entropy alloys, *Phys. Rev. Mater.* 1(2) (2017) 023404.

[53] J.-W. Yeh, S.-Y. Chang, Y.-D. Hong, S.-K. Chen, S.-J. Lin; Anomalous decrease in X-ray diffraction intensities of Cu–Ni–Al–Co–Cr–Fe–Si alloy systems with multi-principal elements, *Mater. Chem. Phys.* 103(1) (2007) 41-46.

[54] Z. Wang, Q. Fang, J. Li, B. Liu, Y. Liu; Effect of lattice distortion on solid solution strengthening of BCC high-entropy alloys, *J. Mater. Sci. Technol.* (2017).

[55] Y.-F. Kao, S.-K. Chen, T.-J. Chen, P.-C. Chu, J.-W. Yeh, S.-J. Lin; Electrical, magnetic, and Hall properties of AlxCoCrFeNi high-entropy alloys, *J. Alloys Compd.* 509(5) (2011) 1607-1614.

[56] N.G. Jones, R. Izzo, P.M. Mignanelli, K.A. Christofidou, H.J. Stone; Phase evolution in an Al0.5CrFeCoNiCu High Entropy Alloy, *INTERMETALLICS* 71 (2016) 43-50.

[57] C. Ng, S. Guo, J. Luan, Q. Wang, J. Lu, S. Shi, C.T. Liu; Phase stability and tensile properties of Co-free Al0.5CrCuFeNi2 high-entropy alloys, *J. Alloys Compd.* 584 (2014) 530-537.

[58] C. Ng, S. Guo, J. Luan, S. Shi, C.T. Liu; Entropy-driven phase stability and slow diffusion kinetics in an Al0.5CoCrCuFeNi high entropy alloy, *INTERMETALLICS* 31 (2012) 165-172.

[59] K.Y. Tsai, M.H. Tsai, J.W. Yeh; Sluggish diffusion in Co–Cr–Fe–Mn–Ni high-entropy alloys, *Acta Mater.* 61(13) (2013) 4887–4897.

[60] O.N. Senkov, J.M. Scott, S.V. Senkova, F. Meisenkothen, D.B. Miracle, C.F. Woodward; Microstructure and elevated temperature properties of a refractory TaNbHfZrTi alloy, *J. Mater. Sci.* 47(9) (2012) 4062-4074.

[61] M.-H. Tsai, C.-W. Wang, C.-W. Tsai, W.-J. Shen, J.-W. Yeh, J.-Y. Gan, W.-W. Wu; Thermal stability and performance of NbSiTaTiZr high-entropy alloy barrier for copper metallization, *J. Electrochem. Soc.* 158(11) (2011) H1161-H1165.

[62] M.-H. Tsai, J.-W. Yeh, J.-Y. Gan; Diffusion barrier properties of AlMoNbSiTaTiVZr high-entropy alloy layer between copper and silicon, *Thin Solid Films* 516(16) (2008) 5527-5530.

[63] C.-J. Tong, Y.-L. Chen, J.-W. Yeh, S.-J. Lin, S.-K. Chen, T.-T. Shun, C.-H. Tsau, S.-Y. Chang; Microstructure characterization of AlxCoCrCuFeNi high-entropy alloy system with multiprincipal elements, *Metall. Mater. Trans. A* 36(4) (2005) 881-893.

[64] J. Kottke, M. Laurent-Brocq, A. Fareed, D. Gaertner, L. Perrière, Ł. Rogal, S.V. Divinski, G. Wilde; Tracer diffusion in the Ni–CoCrFeMn system: Transition from a dilute solid solution to a high entropy alloy, *Scr. Mater.* 159 (2019) 94-98.

[65] S. Ranganathan; Alloyed pleasures: multimetallic cocktails, *Current science* 85(5) (2003) 1404-1406.

[66] O.N. Senkov, D.B. Miracle; A new thermodynamic parameter to predict formation of solid solution or intermetallic phases in high entropy alloys, *J. Alloys Compd.* 658 (2016) 603-607.

[67] J.Y. He, C. Zhu, D.Q. Zhou, W.H. Liu, T.G. Nieh, Z.P. Lu; Steady state flow of the FeCoNiCrMn high entropy alloy at elevated temperatures, *INTERMETALLICS* 55 (2014) 9-14.

[68] S. Praveen, J. Basu, S. Kashyap, R.S. Kottada; Exceptional resistance to grain growth in nanocrystalline CoCrFeNi high entropy alloy at high homologous temperatures, *J. Alloys Compd.* 662 (2016) 361-367.

[69] M. Vaidya, S. Trubel, B.S. Murty, G. Wilde, S. Divinski; Ni tracer diffusion in CoCrFeNi and CoCrFeMnNi high entropy alloys, *J. Alloys Compd.* 688(994-1001) (2016).

[70] Z. Wu, H. Bei, F. Otto, G.M. Pharr, E.P. George; Recovery, recrystallization, grain growth and phase stability of a family of FCC-structured multi-component equiatomic solid solution alloys, *INTERMETALLICS* 46 (2014) 131-140.

[71] M.J. Yao, K.G. Pradeep, C.C. Tasan, D. Raabe; A novel, single phase, non-equiatomic FeMnNiCoCr high-entropy alloy with exceptional phase stability and tensile ductility, *Scr. Mater.* 72–73 (2014) 5-8.

[72] H.-P. Chou, Y.-S. Chang, S.-K. Chen, J.-W. Yeh; Microstructure, thermophysical and electrical properties in AlxCoCrFeNi ($0 \leq x \leq 2$) high-entropy alloys, *Mater. Sci. Eng. B.* 163(3) (2009) 184-189.

[73] N.D. Stepanov, D.G. Shaysultanov, G.A. Salishchev, M.A. Tikhonovsky; Structure and mechanical properties of a light-weight AlNbTiV high entropy alloy, *Mater. Lett.* 142 (2015) 153-155.

[74] X. Yang, Y. Zhang, P.K. Liaw; Microstructure and compressive properties of NbTiVTaAlx high entropy alloys, *Procedia Engineering* 36 (2012) 292-298.

[75] J. Chen, X. Zhou, W. Wang, B. Liu, Y. Lv, W. Yang, D. Xu, Y. Liu; A review on fundamental of high entropy alloys with promising high–temperature properties, *J. Alloys Compd.* 760 (2018) 15-30.

[76] C.-C. Juan, K.-K. Tseng, W.-L. Hsu, M.-H. Tsai, C.-W. Tsai, C.-M. Lin, S.-K. Chen, S.-J. Lin, J.-W. Yeh; Solution strengthening of ductile refractory HfMoxNbTaTiZr high-entropy alloys, *Mater. Lett.* 175 (2016) 284-287.

[77] S. Sheikh, S. Shafeie, Q. Hu, J. Ahlström, C. Persson, J. Veselý, J. Zýka, U. Klement, S. Guo; Alloy design for intrinsically ductile refractory high-entropy alloys, *J. Appl. Phys.* 120(16) (2016) 164902.

[78] Y.D. Wu, Y.H. Cai, T. Wang, J.J. Si, J. Zhu, Y.D. Wang, X.D. Hui; A refractory Hf25Nb25Ti25Zr25 high-entropy alloy with excellent structural stability and tensile properties, *Mater. Lett.* 130 (2014) 277-280.

[79] Q. Guo, O.J. Kleppa; The standard enthalpies of formation of the compounds of early transition metals with late transition metals and with noble metals as determined by Kleppa and co-workers at the University of Chicago — A review, *J. Alloys Compd.* 321(2) (2001) 169-182.

[80] Y. Zhang; Mechanical properties and structures of high entropy alloys and bulk metallic glasses composites, *Mater. Sci. Forum* 654-656 (2010) 1058-1061.

[81] C.-W. Tsai, M.-H. Tsai, J.-W. Yeh, C.-C. Yang; Effect of temperature on mechanical properties of Al0.5CoCrCuFeNi wrought alloy, *J. Alloys Compd.* 490(1) (2010) 160-165.

[82] K.R. Evans, W.F. Flanagan; Solid-solution strengthening of f.c.c. alloys, *Phil. Mag.* 18(155) (1968) 977-983.

[83] M. Walbrühl, D. Linder, J. Ågren, A. Borgenstam; Modelling of solid solution strengthening in multicomponent alloys, *Mater. Sci. Eng. A.* 700(Supplement C) (2017) 301-311.

[84] C.-M. Lin, C.-C. Juan, C.-H. Chang, C.-W. Tsai, J.-W. Yeh; Effect of Al addition on mechanical properties and microstructure of refractory AlxHfNbTaTiZr alloys, *J. Alloys Compd.* 624 (2015) 100-107.

[85] O.N. Senkov, S.V. Senkova, C. Woodward; Effect of aluminum on the microstructure and properties of two refractory high-entropy alloys, *Acta Mater.* 68 (2014) 214-228.

[86] J.C. Rao, V. Ocelík, D. Vainchtein, Z. Tang, P.K. Liaw, J.T.M. De Hosson; The fcc-bcc crystallographic orientation relationship in AlxCoCrFeNi high-entropy alloys, *Mater. Lett.* 176 (2016) 29-32.

[87] Y. Ma, Y.H. Feng, T.T. Debela, G.J. Peng, T.H. Zhang; Nanoindentation study on the creep characteristics of high-entropy alloy films: fcc versus bcc structures, *Int. J. Refract. Met. Hard Mater.* 54 (2016) 395-400.

[88] S. Guo, C. Ng, J. Lu, C.T. Liu; Effect of valence electron concentration on stability of fcc or bcc phase in high entropy alloys, *J. Appl. Phys.* 109(10) (2011) 103505.

[89] S. Guo, C. Ng, J. Lu, C.T. Liu; Effect of valence electron concentration on stability of fcc or bcc phase in high entropy alloys, *J. Appl. Phys.* 109(10) (2011).

[90] O.N. Senkov, S.L. Semiatin; Microstructure and properties of a refractory high-entropy alloy after cold working, *J. Alloys Compd.* 649 (2015) 1110-1123.

[91] A.T. Samaei, M.M. Mirsayar, M.R.M. Aliha; The microstructure and mechanical behavior of modern high temperature alloys, *Engineering Solid Mechanics* 3 (2015) 1-20.

[92] Y. Wu, W.H. Liu, X.L. Wang, D. Ma, A.D. Stoica, T.G. Nieh, Z.B. He, Z.P. Lu; In-situ neutron diffraction study of deformation behavior of a multi-component high-entropy alloy, *Appl. Phys. Lett.* 104(5) (2014) 051910.

[93] V. Soni, O.N. Senkov, B. Gwalani, D.B. Miracle, R. Banerjee; Microstructural Design for Improving Ductility of An Initially Brittle Refractory High Entropy Alloy, *Sci. Rep.* 8(1) (2018) 8816.

[94] Y. Lederer, C. Toher, K.S. Vecchio, S. Curtarolo; The search for high entropy alloys: A high-throughput ab-initio approach, *Acta Mater.* 159 (2018) 364-383.

[95] C. Dmitry; Crystallography with synchrotron light, *J. Phys. D: Appl. Phys.* 48(50) (2015) 504001.

[96] A.P. Hammersley, S.O. Svensson, M. Hanfland, A.N. Fitch, D. Hausermann; Two-dimensional detector software: From real detector to idealised image or two-theta scan, *High Pressure Research* 14(4-6) (1996) 235-248.

[97] P.M. Woodward, K.Z. Baba-Kishi; Crystal structures of the relaxor oxide Pb2(ScTa)O6 in the paraelectric and ferroelectric states, *J. Appl. Crystallogr.* 35(2) (2002) 233-242.

[98] J. Gubicza, *X-ray line profile analysis in materials science*, IGI Global (2014).

[99] A. Khorsand Zak, W.H. Abd. Majid, M.E. Abrishami, R. Yousefi; X-ray analysis of ZnO nanoparticles by Williamson–Hall and size–strain plot methods, *Solid State Sci.* 13(1) (2011) 251-256.

[100] G.K. Williamson, W.H. Hall; X-ray line broadening from filed aluminium and wolfram, *Acta Metall.* 1(1) (1953) 22-31.

[101] P. Juhas, T. Davis, C.L. Farrow, S.J.L. Billinge; PDFgetX3: a rapid and highly automatable program for processing powder diffraction data into total scattering pair distribution functions, *J. Appl. Crystallogr.* 46(2) (2013) 560-566.

[102] T. Egami, S.J.L. Billinge, *Underneath the bragg peaks: Structural analysis of complex materials*, Elsevier Science (2012).

[103] V. Petkov; *Pair distribution functions analysis*, In Characterization of Materials, John Wiley & Sons (2012).

[104] L.R. Owen, E.J. Pickering, H.Y. Playford, H.J. Stone, M.G. Tucker, N.G. Jones; An assessment of the lattice strain in the CrMnFeCoNi high-entropy alloy, *Acta Mater.* 122 (2017) 11-18.

[105] A. Šalak, M. Selecká, *Manganese in Powder Metallurgy Steels*, Cambridge International Science Publishing Limited (2012).

[106] E. Hryha, E. Dudrova; *The sintering behaviour of Fe-Mn-C powder system, correlation between thermodynamics and sintering process, manganese distribution and microstructure composition, effect of alloying mode*, In Application of thermodynamics to biological and materials science, InTech (2011).

[107] N.N. Greenwood, A. Earnshaw, *Chemistry of the elements*, Pergamon (1984).

[108] M. Winter; *http://www.webelements.com*, 2018 (2018).

[109] G.V. Raynor, V.G. Rivlin, *Phase equilibria in iron ternary alloys: a critical assessment of the experimental literature*, Institute of Metals (1988).

[110] ASM International; *ASM handbook volume 3: Alloy phase diagrams*, ASM International, the United States of America, 1992.

[111] B. Schuh, F. Mendez-Martin, B. Völker, E.P. George, H. Clemens, R. Pippan, A. Hohenwarter; Mechanical properties, microstructure and thermal stability of a nanocrystalline CoCrFeMnNi high-entropy alloy after severe plastic deformation, *Acta Mater.* 96 (2015) 258-268.

[112] N.D. Stepanov, D.G. Shaysultanov, M.S. Ozerov, S.V. Zherebtsov, G.A. Salishchev; Second phase formation in the CoCrFeNiMn high entropy alloy after recrystallization annealing, *Mater. Lett.* 185 (2016) 1-4.

[113] J.Y. He, H. Wang, Y. Wu, X.J. Liu, H.H. Mao, T.G. Nieh, Z.P. Lu; Precipitation behavior and its effects on tensile properties of FeCoNiCr high-entropy alloys, *INTERMETALLICS* 79 (2016) 41-52.

[114] O.N. Senkov, J.D. Miller, D.B. Miracle, C. Woodward; Accelerated exploration of multi-principal element alloys for structural applications, *Calphad* 50 (2015) 32-48.

[115] A.K. Singh, A. Subramaniam; On the formation of disordered solid solutions in multi-component alloys, *J. Alloys Compd.* 587 (2014) 113-119.

[116] S. Guo, C.T. Liu; Phase stability in high entropy alloys: Formation of solid-solution phase or amorphous phase, *Progress in Natural Science: Materials International* 21(6) (2011) 433-446.

[117] B.D. Cullity, *Elements of x-ray diffraction*, Addison-Wesley Publishing Company (1978).

[118] G.E. Ice, C.J. Sparks, X. Jiang, L. Robertson; Diffuse scattering measurements of static atomic displacements in crystalline binary solid solutions, *Journal of Phase Equilibria* 19(6) (1998) 529.

[119] I.K. Jeong, R.H. Heffner, M.J. Graf, S.J.L. Billinge; Lattice dynamics and correlated atomic motion from the atomic pair distribution function, *Phys. Rev. B* 67(10) (2003) 104301-1-9.

[120] L. Cartz; Thermal vibrations of atoms in cubic crystals II: the amplitude of atomic vibrations, *Proc. Phys. Soc. London, Sect. B* 68(11) (1955) 957.

[121] H.E. Cook; The influence of static atomic displacements on the diffuse intensity scattered by solid solutions, *J. Phys. Chem. Solids* 30(5) (1969) 1097-1112.

[122] N.L. Okamoto, K. Yuge, K. Tanaka, H. Inui, E.P. George; Atomic displacement in the CrMnFeCoNi high-entropy alloy – A scaling factor to predict solid solution strengthening, *AIP Advances* 6(12) (2016) 125008.

[123] R. Kaplow, S.L. Strong, B.L. Averbach; Radial density functions for liquid mercury and lead, *Physical Review* 138(5A) (1965) A1336-A1345.

[124] R. Kaplow, B.L. Averbach, S.L. Strong; Pair correlations in solid lead near the melting temperature, *J. Phys. Chem. Solids* 25(11) (1964) 1195-1204.

[125] G.E. Dieter, *Mechanical metallurgy*, McGraw-Hill (1976).

[126] W.F. Hosford, *Mechanical behavior of materials*, Cambridge University Press, Cambridge, (2005).

[127] ASM International; *10ASM handbook volume 2: Properties and selection: Nonferrous alloys and special-purpose materials*, 10 ed., ASM International, the United States of America, 1990.

[128] I. Toda-Caraballo, P.E.J. Rivera-Díaz-del-Castillo; Modelling solid solution hardening in high entropy alloys, *Acta Mater.* 85 (2015) 14-23.

[129] R.W. Cahn, P. Haasen (Ed.); *Physical metallurgy*, North-Holland Physics Publishing, Amsterdam, (1996).

[130] S. Mahajan; Critique of mechanisms of formation of deformation, annealing and growth twins: Face-centered cubic metals and alloys, *Scr. Mater.* 68(2) (2013) 95-99.

[131] W. Wang, S. Lartigue-Korinek, F. Brisset, A.L. Helbert, J. Bourgon, T. Baudin; Formation of annealing twins during primary recrystallization of two low stacking fault energy Ni-based alloys, *J. Mater. Sci.* 50(5) (2015) 2167-2177.

[132] C.B. Carter, S.M. Holmes; The stacking-fault energy of nickel, *Phil. Mag.* 35(5) (1977) 1161-1172.

[133] M.F. de Campos, S.A. Loureiro, D. Rodrigues, M.d.C. Silva, N.B. de Lima; Estimative of the stacking fault energy for a FeNi(50/50) alloy and a 316L stainless steel, *Mater. Sci. Forum* 591 - 593 (2008) 3-7.

[134] A.J. Zaddach, C. Niu, C.C. Koch, D.L. Irving; Mechanical properties and stacking fault energies of NiFeCrCoMn high-entropy alloy, *JOM* 65(12) (2013) 1780-1789.

[135] V. Randle, P.R. Rios, Y. Hu; Grain growth and twinning in nickel, *Scr. Mater.* 58(2) (2008) 130-133.

[136] A. Rollett, F.J. Humphreys, G.S. Rohrer, M. Hatherly, *Recrystallization and related annealing phenomena*, Elsevier, Netherlands, (2004).

[137] B.-R. Chen, A.-C. Yeh, J.-W. Yeh; Effect of one-step recrystallization on the grain boundary evolution of CoCrFeMnNi high entropy alloy and its subsystems, *Sci. Rep.* 6 (2016) 1-9.

[138] C.S. Pande, M.A. Imam, B.B. Rath; Study of annealing twins in fcc metals and alloys, *Metall. Trans. A* 21(11) (1990) 2891-2896.

[139] Y. Jin, B. Lin, A.D. Rollett, G.S. Rohrer, M. Bernacki, N. Bozzolo; Thermo-mechanical factors influencing annealing twin development in nickel during recrystallization, *J. Mater. Sci.* 50(15) (2015) 5191-5203.

[140] R. Carroll, C. Lee, C.-W. Tsai, J.-W. Yeh, J. Antonaglia, B.A.W. Brinkman, M. LeBlanc, X. Xie, S. Chen, P.K. Liaw, K.A. Dahmen; Experiments and model for serration statistics in low-entropy, medium-entropy, and high-entropy alloys, *Sci. Rep.* 5 (2015) 16997.

[141] Y. Zhang, J.-w. Qiao, P.K. Liaw; A Brief Review of High Entropy Alloys and Serration Behavior and Flow Units, *J. Iron. Steel Res. Int.* 23(1) (2016) 2-6.

[142] W.Y. Wang, S.L. Shang, Y. Wang, F. Han, K.A. Darling, Y. Wu, X. Xie, O.N. Senkov, J. Li, X.D. Hui, K.A. Dahmen, P.K. Liaw, L.J. Kecskes, Z.-K. Liu; Atomic and electronic basis for the serrations of refractory high-entropy alloys, *NPJ COMPUT MATER* 3(1) (2017) 23.

[143] B. Gludovatz, E. George, R. Ritchie; Processing, microstructure and mechanical properties of the CrMnFeCoNi high-entropy alloy, *JOM* 67(10) (2015) 2262-2270.

[144] R. Kozak, A. Sologubenko, W. Steurer; Single-phase high-entropy alloys–an overview, *Z. Kristallogr. Cryst. Mater.* 230(1) (2015) 55-68.

[145] S.-W. Kim, J.H. Kim; In-situ observations of deformation twins and crack propagation in a CoCrFeNiMn high-entropy alloy, *Mater. Sci. Eng. A.* 718 (2018) 321-325.

[146] A.H. Committee, *Metals handbook: Fractography*, American Society for Metals (1978).

[147] W.Y. Guo, J. Sun; Annealing twins in a multifunctional beta Ti-Nb-Ta-Zr-O alloy, *Bull. Mater. Sci.* 34(7) (2011) 1435-1438.

[148] J.Z. Lu, J.S. Zhong, K.Y. Luo, L. Zhang, H. Qi, M. Luo, X.J. Xu, J.Z. Zhou; Strain rate correspondence of fracture surface features and tensile properties in AISI304 stainless steel under different LSP impact time, *Surf. Coat. Technol.* 221 (2013) 88-93.

[149] F.R.N. Nabarro; The mechanical properties of metallic solid solutions, *Proceedings of the Physical Society* 58(6) (1946) 669.

[150] P. Haasen; *Mechanical Properties of Solid Solutions*, In Fundamental Aspects of Structural Alloy Design, Springer US, Boston, MA, (1977). 3-25.

[151] H.W. Yao, J.W. Qiao, J.A. Hawk, H.F. Zhou, M.W. Chen, M.C. Gao; Mechanical properties of refractory high-entropy alloys: Experiments and modeling, *J. Alloys Compd.* 696 (2017) 1139-1150.

[152] S. Maiti, W. Steurer; Phase stability, local chemical disorder and its effect on the mechanical properties of refractory high-entropy alloys, *eprint arXiv:1601.06015* (2016).

[153] T. Murakami, R. Sahara, D. Harako, M. Akiba, T. Narushima, C. Ouchi; The effect of solute elements on hardness and grain size in platinum based binary alloys, *Materials transactions* 49(3) (2008) 538-547.

[154] C. Varvenne, G.P.M. Leyson, M. Ghazisaeidi, W.A. Curtin; Solute strengthening in random alloys, *Acta Mater.* 124 (2017) 660-683.

[155] H. Sieurin, J. Zander, R. Sandström; Modelling solid solution hardening in stainless steels, *Mater. Sci. Eng. A.* 415(1) (2006) 66-71.

[156] Z. Wu, H. Bei, G.M. Pharr, E.P. George; Temperature dependence of the mechanical properties of equiatomic solid solution alloys with face-centered cubic crystal structures, *Acta Mater.* 81 (2014) 428-441.

[157] S.F. Liu, Y. Wu, H.T. Wang, J.Y. He, J.B. Liu, C.X. Chen, X.J. Liu, H. Wang, Z.P. Lu; Stacking fault energy of face-centered-cubic high entropy alloys, *INTERMETALLICS* 93 (2018) 269-273.

[158] F. Hamdi, S. Asgari; Influence of stacking fault energy and short-range ordering on dynamic recovery and work hardening behavior of copper alloys, *Scr. Mater.* 62(9) (2010) 693-696.

[159] W. Skrotzki, A. Pukenas, B. Joni, E. Odor, T. Ungar, A. Hohenwarter, R. Pippan, E.P. George; Microstructure and texture evolution during severe plastic deformation of CrMnFeCoNi high-entropy alloy, *IOP Conf. Ser.: Mater. Sci. Eng.* 194(1) (2017) 012028.

[160] Y. Deng, C.C. Tasan, K.G. Pradeep, H. Springer, A. Kostka, D. Raabe; Design of a twinning-induced plasticity high entropy alloy, *Acta Mater.* 94 (2015) 124-133.

[161] J.P. Couzinié, L. Lilensten, Y. Champion, G. Dirras, L. Perrière, I. Guillot; On the room temperature deformation mechanisms of a TiZrHfNbTa refractory high-entropy alloy, *Mater. Sci. Eng. A.* 645 (2015) 255-263.

[162] T. Shintani, Y. Murata; Evaluation of the dislocation density and dislocation character in cold rolled Type 304 steel determined by profile analysis of X-ray diffraction, *Acta Mater.* 59(11) (2011) 4314-4322.

[163] G.K. Williamson, R.E. Smallman; III. Dislocation densities in some annealed and cold-worked metals from measurements on the X-ray debye-scherrer spectrum, *Phil. Mag.* 1(1) (1956) 34-46.

[164] R.E. Smallman, R.J. Bishop, *Modern physical metallurgy and materials engineering*, Butterworth-Heinemann, Oxford, (1999).

[165] Y. Miyajima, T. Ueda, H. Adachi, T. Fujii, S. Onaka, M. Kato; Dislocation Density of FCC Metals Processed by ARB, *IOP Conf. Ser.: Mater. Sci. Eng.* 63(1) (2014) 012138.

[166] K. Edalati, D. Akama, A. Nishio, S. Lee, Y. Yonenaga, J. Cubero-Sesin, Z. Horita; Influence of dislocation–solute atom interactions and stacking fault energy on grain size of single-phase alloys after severe plastic deformation using high-pressure torsion, 69 (2014) 68–77.

[167] N.L. Okamoto, S. Fujimoto, Y. Kambara, M. Kawamura, Z.M.T. Chen, H. Matsunoshita, K. Tanaka, H. Inui, E.P. George; Size effect, critical resolved shear stress, stacking fault energy, and solid solution strengthening in the CrMnFeCoNi high-entropy alloy, *Sci. Rep.* 6 (2016) 35863.

[168] H. Parvin, M. Kazeminezhad; Development a dislocation density based model considering the effect of stacking fault energy: Severe plastic deformation, *Comput. Mater. Sci.* 95 (2014) 250-255.

[169] L. Vitos, J.O. Nilsson, B. Johansson; Alloying effects on the stacking fault energy in austenitic stainless steels from first-principles theory, *Acta Mater.* 54(14) (2006) 3821-3826.

[170] B. Cai, S. Ren, S. Zhou, P. Li, W. Lv, J. Tao, X. Zhu; Effects of stacking fault energy on the deformation mechanisms and mechanical properties of Cu and Cu alloys processed by rolling at different temperatures, *Indian J. Eng. Mater. Sci.* 22 (2015) 399-406.

[171] W.G. Nöhring, W.A. Curtin; Dislocation cross-slip in fcc solid solution alloys, *Acta Mater.* 128 (2017) 135-148.

[172] D.M. Symons; Hydrogen embrittlement of Ni-Cr-Fe alloys, *Metall. Mater. Trans. A* 28(3) (1997) 655-663.

[173] D.J. Siegel; Generalized stacking fault energies, ductilities, and twinnabilities of Ni and selected Ni alloys, *Appl. Phys. Lett.* 87(12) (2005) 121901.

[174] F.R.S. G. I. Taylor; The mechanism of plastic deformation of crystals. Part I.—Theoretical, *Proceedings of the Royal Society of London. Series A* 145(855) (1934) 362.

[175] M. Čebron, F. Kosel; Stored energy predictions from dislocation-based hardening models and hardness measurements for tensile-deformed commercial purity copper, *Strojniški vestnik-Journal of Mechanical Engineering* 60(7-8) (2014) 462-474.

[176] F.F. Lavrentev; The type of dislocation interaction as the factor determining work hardening, *Mater. Sci. Eng.* 46(2) (1980) 191-208.

[177] K.K. Chawla, M. Meyers, *Mechanical behavior of materials*, Prentice Hall Upper Saddle River (1999).

[178] E. Nes; Modelling of work hardening and stress saturation in FCC metals, *Prog. Mater Sci.* 41(3) (1997) 129-193.

[179] Y. Murata, I. Nakaya, M. Morinaga; Assessment of strain energy by measuring dislocation density in copper and aluminium prepared by ECAP and ARB, *Materials transactions* 49(1) (2008) 20-23.

[180] L.M. Voronova, T.I. Chashchukhina, T.M. Gapontseva, Y.G. Krasnoperova, M.V. Degtyarev, V.P. Pilyugin; Effect of the deformation temperature on the structural refinement of

BCC metals with a high stacking fault energy during high pressure torsion, *Russian Metallurgy (Metally)* 2016(10) (2016) 960-965.

[181] E.I. Galindo Nava; Thermostatistical theory of plastic deformation in metals, Mater. Sci. Eng., Delft University of Technology, 2013.

[182] I.L. Dillamore, E. Butler, D. Green; Crystal Rotations under Conditions of Imposed Strain and the Influence of Twinning and Cross-Slip, *Metal Science Journal* 2(1) (1968) 161-167.

[183] S. Nemat-Nasser, W. Guo; Flow stress of commercially pure niobium over a broad range of temperatures and strain rates, *Mater. Sci. Eng. A.* 284(1-2) (2000) 202-210.

[184] A.A. Galkin, V.V. Tokii, B.P. Filatov; Dislocation multiplication. II. The effect of the initial defect structure and deformation conditions on the dislocation multiplication, *Phys. Status Solidi A* 45(1) (1978) 327-332.

[185] W. Püschl; Models for dislocation cross-slip in close-packed crystal structures: a critical review, *Prog. Mater Sci.* 47(4) (2002) 415-461.

[186] B. Ziebarth, M. Mrovec, C. Elsässer, P. Gumbsch; Influence of dislocation strain fields on the diffusion of interstitial iron impurities in silicon, *Phys. Rev. B* 92(11) (2015) 115309.

[187] J.M. Rosenberg, H.R. Piehler; Calculation of the taylor factor and lattice rotations for bcc metals deforming by pencil glide, *Metallurgical Transactions* 2(1) (1971) 257-259.

[188] K.M. Davoudi, J.J. Vlassak; Dislocation evolution during plastic deformation: Equations vs. discrete dislocation simulations, *arXiv preprint arXiv:1408.6609* (2014).

[189] G. Dirras, H. Couque, L. Lilensten, A. Heczel, D. Tingaud, J.P. Couzinié, L. Perrière, J. Gubicza, I. Guillot; Mechanical behavior and microstructure of Ti20Hf20Zr20Ta20Nb20 high-entropy alloy loaded under quasi-static and dynamic compression conditions, *Mater. Charact.* 111 (2016) 106-113.

Acknowledgements

First of all, I would like to express my sincere gratitude and appreciation to Prof. Jürgen Eckert for an opportunity to do PhD at IFW-Dresden, in association with Faculty of Mechanical Science and Engineering at the Technical University of Dresden. I equally thank Prof. Kornelius Nielsch, my supervisor, and Dr. Thomas Gemming for all constant supports, including financial supports, for my PhD research. Also thanks to the Graduate Academy of TU Dresden for a grant during completion phase of my PhD.

This paragraph is dedicated to my research supervisor Dr. Junhee Han who always assists me in both academic and personal life throughout my PhD. He is the best supervisor who never lets me face problems alone. I would like to thank a million to him for his simplicity, patience, motivation, immense knowledge and all discussions, which importantly improve my skills and perception throughout my PhD life.

I particularly thank Dr. Piter Gargarella for agreeing to be the second reviewer of this thesis.

I would like to special thank Dr. U. Kühn, Dr. I. Kaban, Assoc. Prof. Dr. M. Calin and Dr. M. for all their supports and valuable suggestions. My sincere thanks also go to Prof. Dr. J. Freudenberger, Dr. A. Gebert and Dr. M. Uhlemann for supporting my experimental works at IFW-Dresden, especially Dr. H. Wendrock for the discussion and advises on EBSD measurement and post processing. I also express thanks to B. Bartusch, S. Donath, M. Frey, S. Grundkowski, A. Voß, H. Bußkamp, J. Scheiter, K. Schröder, C. Mix, A. Kahnt, N. Geißler, B. Opitz, A. Schultze, D. Seifert and C. Blum for technical supports and advices on my experimental works. I also thank Dr. J. Jayaraj and Dr. G. Song for research collaboration and suggestion on the research work, and Dr. J. Bednarčik for support and advices during the synchrotron experiments in DESY, Hamburg.

Thanks to R. N. Shahid and S. Omar for doing PhD and sharing funny PhD experiences together from the beginning. I also give thanks all the former and current colleagues at the IFW-Dresden for their supports and keeping a friendly working environment: T. He, J. Zeisig , T. Gustmann, B. S. Kim, P. Ramasamy, X. Cai, L. Xi, K. Kosiba, P. Wang, R. G. Mendes, S. Pilz, J.

Wang, J. Pang, H. Weber, M. Monica, A. Fernandes Andreoli, M. Romero da Silva, S. Yousefli, A. Funk, A. Permana, S. Selter and Dr. S. Scudino. I would like to thank B. Präßler-Wüstling for all administrative works.

I am grateful to Prof. U. Takateru, Dr. N. Phinichka, Dr. S. Niyomsoan, Dr. S. Kaenthong, Dr. S. Suphansomboon and Dr. S. Wongsriraksa for motivating me to pursue PhD and to experience this unforgettable time.

Thanks to all Thai friends in Dresden for Thai food party and joyful leisure. Also thanks to my best friends Niyaporn and Hacchan for their encouragements and giving me a cup of coffee all the time.

Last, but not least, I would like to dedicate my thesis to my beloved father and sister, who have been gone during my PhD study. With the great supports of my father, mother, sister, brother, sister in law, nephew, all of my relatives and friends, I can continue doing this thesis until the end. I absolutely know that my father and my sister will give me wide smiles for a gift on my day. Thanks to my great family and friends.

Erklärung

Hiermit versichere ich, dass ich die vorliegende Arbeit ohne unzulässige Hilfe Dritter und ohne Benutzung anderer als der angegebenen Hilfsmittel angefertigt habe; die aus fremden Quellen direkt oder indirekt übernommenen Gedanken sind als solche kenntlich gemacht. Bei der Auswahl und Auswertung des Materials sowie bei der Herstellung des Manuskripts habe ich Unterstützungsleistungen von folgenden Personen erhalten: Prof. Dr. Kornelius Nielsch und Dr. Junhee Han. Weitere Personen waren an der geistigen Herstellung der vorliegenden Arbeit nicht beteiligt. Insbesondere habe ich nicht die Hilfe eines kommerziellen Promotionsberaters in Anspruch genommen. Dritte haben von mir keine geldwerten Leistungen für Arbeiten erhalten, die in Zusammenhang mit dem Inhalt der vorgelegten Dissertation stehen. Die Arbeit wurde bisher weder im Inland noch im Ausland in gleicher oder ähnlicher Form einer anderen Prüfungsbehörde vorgelegt und ist auch noch nicht veröffentlicht worden. Die Promotionsordnung der Fakultät Maschinenwesen der TU Dresden aus dem Jahre 2001 erkenne ich an.

Pramote Thirathipviwat

Dresden, 11.01.2019